A Computational Investigation of Gear Windage

Matthew J. Hill and Robert F. Kunz
Pennsylvania State University, Philadelphia, Pennsylvania

NASA STI Program . . . in Profile

Since its founding, NASA has been dedicated to the advancement of aeronautics and space science. The NASA Scientific and Technical Information (STI) program plays a key part in helping NASA maintain this important role.

The NASA STI Program operates under the auspices of the Agency Chief Information Officer. It collects, organizes, provides for archiving, and disseminates NASA's STI. The NASA STI program provides access to the NASA Aeronautics and Space Database and its public interface, the NASA Technical Reports Server, thus providing one of the largest collections of aeronautical and space science STI in the world. Results are published in both non-NASA channels and by NASA in the NASA STI Report Series, which includes the following report types:

- TECHNICAL PUBLICATION. Reports of completed research or a major significant phase of research that present the results of NASA programs and include extensive data or theoretical analysis. Includes compilations of significant scientific and technical data and information deemed to be of continuing reference value. NASA counterpart of peer-reviewed formal professional papers but has less stringent limitations on manuscript length and extent of graphic presentations.

- TECHNICAL MEMORANDUM. Scientific and technical findings that are preliminary or of specialized interest, e.g., quick release reports, working papers, and bibliographies that contain minimal annotation. Does not contain extensive analysis.

- CONTRACTOR REPORT. Scientific and technical findings by NASA-sponsored contractors and grantees.

- CONFERENCE PUBLICATION. Collected papers from scientific and technical conferences, symposia, seminars, or other meetings sponsored or cosponsored by NASA.

- SPECIAL PUBLICATION. Scientific, technical, or historical information from NASA programs, projects, and missions, often concerned with subjects having substantial public interest.

- TECHNICAL TRANSLATION. English-language translations of foreign scientific and technical material pertinent to NASA's mission.

Specialized services also include creating custom thesauri, building customized databases, organizing and publishing research results.

For more information about the NASA STI program, see the following:

- Access the NASA STI program home page at *http://www.sti.nasa.gov*

- E-mail your question to *help@sti.nasa.gov*

- Fax your question to the NASA STI Information Desk at 443–757–5803

- Phone the NASA STI Information Desk at 443–757–5802

- Write to:
  STI Information Desk
  NASA Center for AeroSpace Information
  7115 Standard Drive
  Hanover, MD 21076–1320

NASA/CR—2012-217807

A Computational Investigation of Gear Windage

Matthew J. Hill and Robert F. Kunz
Pennsylvania State University, Philadelphia, Pennsylvania

National Aeronautics and
Space Administration

Glenn Research Center
Cleveland, Ohio 44135

December 2012

Acknowledgments

A Computational Investigation of Gear Windage

Matthew J. Hill and Robert F. Kunz
Pennsylvania State University
Philadelphia, Pennsylvania 19104

Abstract

A CFD method has been developed for application to gear windage aerodynamics. The goals of this research are to develop and validate numerical and modeling approaches for these systems, to develop physical understanding of the aerodynamics of gear windage loss, including the physics of loss mitigation strategies, and to propose and evaluate new approaches for minimizing loss. Absolute and relative frame CFD simulation, overset gridding, multiphase flow analysis, and sub-layer resolved turbulence modeling were brought to bear in achieving these goals. Several spur gear geometries were studied for which experimental data are available. Various shrouding configurations and free-spinning (no shroud) cases were studied. Comparisons are made with experimental data from the open literature, and data recently obtained in the NASA Glenn Research Center Gear Windage Test Facility. The results show good agreement with experiment. Interrogation of the validative and exploratory CFD results have led, for the first time, to a detailed understanding of the physical mechanisms of gear windage loss, and have led to newly proposed mitigation strategies whose effectiveness is computationally explored.

Table of Contents

List of Figures

List of Tables

Chapter 1

Introduction

Gears provide an extremely efficient method for the transmission of rotary motion and power. It is possible to achieve efficiencies of 99% with a well designed gearbox, but a number of power loss mechanisms have to be overcome to achieve such efficiencies. These mechanisms include meshing (sliding and rolling) losses, bearing losses, lubrication churning losses, and windage losses. The relative importance of these mechanisms varies depending on the application. In high speed gearing applications, windage effects become extremely important and can dominate the other loss mechanisms. Unfortunately, windage losses are extremely difficult to measure accurately and are the least understood of the other mechanisms.

Windage losses are a result of the aerodynamic drag forces (pressure and viscous) that act on rotating gears. They are a function of the size, shape, and rotation speed of the gears. Inside a gear transmission, windage manifests itself as increased rotational resistance and added heating. These effects present several problems for rotorcraft transmission systems. Rotorcraft transmissions are susceptible to windage effects because of the high rotation speeds introduced by their gas turbine engines. Rotorcraft can require reduction ratios anywhere between 25:1 and 100:1 [5, 8] between engine and rotors. For example, the UH-60A helicopter transmission provides a reduction ratio of 81.042:1 from the engine input (20,900 rpm) to the main rotor output (258 rpm) [9].

The increased rotational resistance consumes engine power which reduces range and payload. Windage losses in a transmission can consume up to 3% of the transmitted power from the engines. For a rotorcraft like the V-22 Osprey, whose

engines produce 6,150 hp (4,590 kW), that can mean windage losses up to 180 hp (137 kW). The added heating has design implications for the lubrication cooling system which must be sized appropriately to absorb and dissipate all of the heat generated within the gearbox. Proper functioning of the transmission lubrication cooling system is critical on a rotorcraft because its unique weight and packaging constraints require the gearing to be extremely lightweight. This means that the gears have a relatively low heat carrying capacity and need to be actively cooled during operation. If the cooling requirements (along with the size and complexity of the cooling system) can be reduced, this could present significant benefits in range, maintenance costs, and payload capacity. Furthermore, rotorcraft survivability under transmission oil-out conditions is exacerbated by windage. In the oil-out condition, the lubrication cooling system has ceased to function either due to damage or component failure. Since windage manifests as added dissipative flow heating, the loss of the cooling system can lead to a catastrophic failure of the drive system. Figure 1.1 is from Bartz [1] and shows the effect of running high-speed gears without lubrication. The gear teeth have deformed and have lost the ability to transfer power.

Despite the significant relevance, design efforts throughout the gearing industry aimed at reducing windage losses have generally fallen into the trial and error category. Nevertheless, it has been shown by some that modest geometric modifications to control the air flow path, such as shrouding, can very significantly reduce both windage losses and lubricating oil consumption (80% and 40% reductions were observed, respectively, in Reference [10]). However, these hardware specific approaches are empirical, time consuming, and expensive.

1.1   A Brief Introduction to Gearing

Gears are machine elements that transmit rotary motion and power by the successive engagements of teeth on their periphery. They provide an extremely efficient method for such transmission, especially if power levels and accuracy requirements are high. Gears come in a wide variety of types to serve different functions. Figure 1.2 provides sketches of some of the more common gear types. Spur gears are used to transmit motion between parallel shafts. The teeth are radial, uniformly
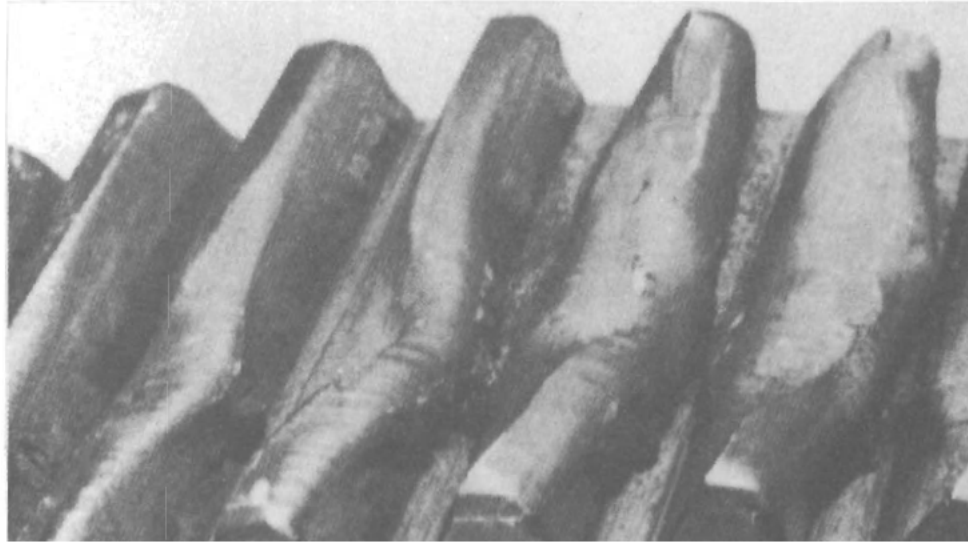
Figure 1.1. Effect of lubrication failure on a gear. [1]

spaced around the outer periphery and are parallel to the axis of rotation. Helical gears can transmit motion between parallel or crossed shafts by meshing teeth that lie along a helix at an angle to the axis of the shaft. Mating of the teeth occurs such that two or more teeth of each gear are always in contact. This permits smoother action than that of spur gears. However, helical gears also generate axial thrust which causes slight power loss and requires thrust bearings.

Bevel gears are used to transmit rotary motion between two non-parallel shafts and come in a variety of tooth designs. Straight bevel gears have straight teeth that, if extended inward, would intersect at the axis of gear. Spiral bevel gears have teeth that are curved and oblique. They provide a greater load carrying capacity and transmit the load more smoothly than straight bevel gears. Zerol bevel gears differ from spiral bevel gears in that their teeth are not oblique. Face gears have teeth cut on the end face of a gear.

This dissertation focuses on spur and helical gears. Figure 1.3 is a schematic
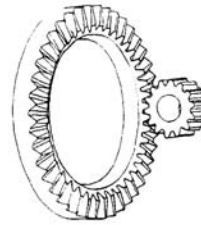
Figure 1.2. Various gear types. [2]

of the typical gear nomenclature and is from Reference [3]. The pitch circle is the circumference of a gear measured at the point of contact with the mating gear and the pitch diameter and pitch radius are the diameter and radius, respectively, of the this circle. In the English system, the size of the teeth is described by the diametral pitch (DP), which is the number of teeth per inch of pitch diameter. As tooth size increases, the diametral pitch decreases. However, in the metric system, the module is used in place of diametral pitch and it is simply the reciprocal of

the diametral pitch. It is given in units of millimeters. Pressure angle denotes the angle between a tooth profile and a radial line at its pitch point. The pressure angle of an involute gear tooth is determined by the size ratio between the base circle and the pitch circle. The standard pressure angles used in the gearing industry are 14.5, 20, and 25°, with 20° being the most common [11].

An involute gear tooth is a gear tooth whose profile is established by an involute curve outward from the base circle. A involute curve is described by curve that is drawn by the unwinding of a taut string from the base circle. The involute profile can mathematically describe the thickness of the teeth as a function of radius:

$$t(R) = R \left[\frac{t_S}{R_S} + 2(\text{inv}(\phi_S) - \text{inv}(\phi_R)) \right] \tag{1.1}$$

where t_S denotes the thickness at the pitch radius, R_S, and is determined by the equation:

$$t_S = \pi/(2 \times \text{DP}) \tag{1.2}$$

$\text{inv}(\phi)$ is the involute function and is given by Equation 1.3:

$$\text{inv}(\phi) = tan(\phi) - \phi \tag{1.3}$$

where ϕ is in radians. ϕ_S and ϕ_R are pressure angles calculated by the equation

$$\phi = cos^{-1}\frac{R_B}{R} \tag{1.4}$$

where R_B denotes the radius of the base circle.
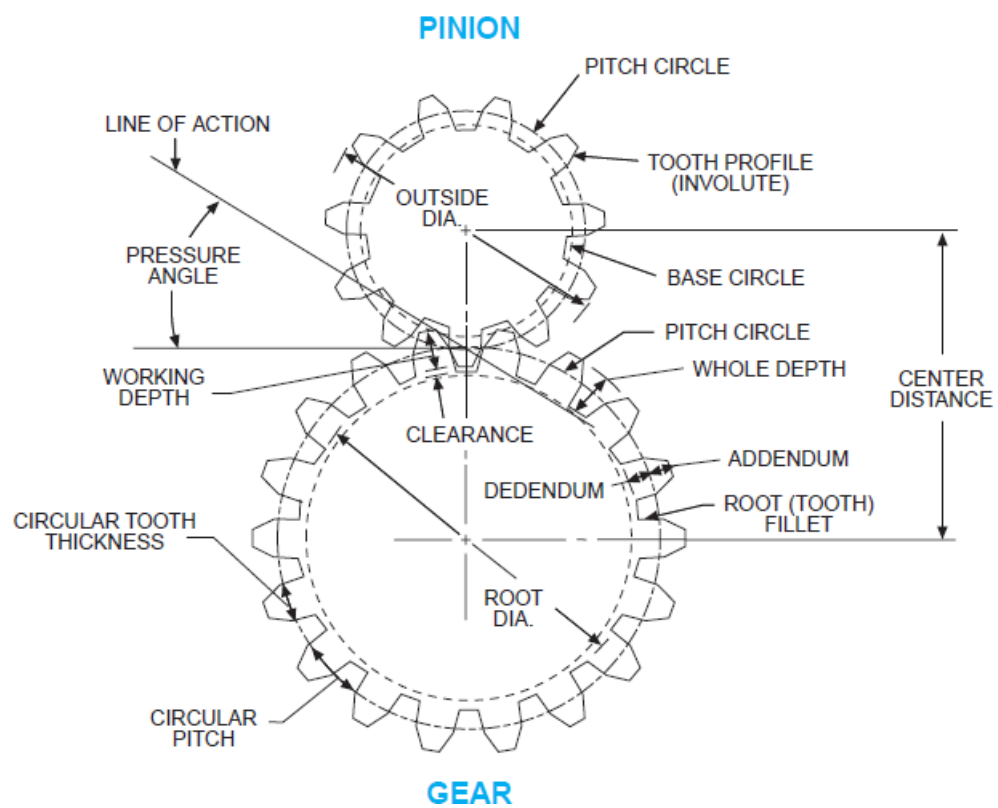
Figure 1.3. Schematic of typical gear tooth nomenclature. [3]

1.2 Previous Research

The available, open literature on gear windage is somewhat sparse. Numerous studies have been conducted on rotating disks or drums [12, 13, 14, 15, 16, 17], but there have only been a handful of published studies on rotating gears. These studies typically report on experimental evidence of the presence of windage and the associated heating and power consumption [5].

The literature on rotating disk flows is rather extensive. Von Karman [12] used an approximate method based on the momentum equation to investigate the turbulent boundary layer on a rotating disk. Schlichting [13] provides an analytic solution of the incompressible Navier-Stokes equations for an infinite spanning rotating disk. Much of the literature has been in the area of gas turbine analysis [15, 16, 17]. These studies focus on the effects of shrouding, turbine disk placement, and coolant flows in gas turbine engines. Daily and Nece [14] studied experimentally and theoretically the rotation of a fully enclosed disk. The effect of axial clearance was studied was studied while the radial tip clearance was kept small. Water and four different lubricating oils were the test fluids. Daily and Nece identified four possible flow modes within the disk enclosure: laminar flow with merged boundary layers between the shroud wall and disk, laminar flow with separate boundary layers, turbulent flow with merged boundary layers, and turbulent flow with separate boundary layers. Maroti et al. [15] studied a rotating disk in air with only axial shrouding (no outer radial shroud) and noticed an unsteady flow pattern when the shrouds were radially larger than the disk. It was also observed that the viscous torque on the disk was greater when the flow was unsteady. Bayley et al. [16] studied air-cooled shrouded disk systems. However, the shrouds did not fully enclose the disk as the shrouds shared the same radial dimensions. The disks were cooled by air that was pumped from the axis of of the shroud system. Bayley found that when there was no forced radial outflow of coolant, the shrouds reduced the viscous moment on the disk by conserving the angular momentum between the rotor and the stator shroud at high Reynolds numbers. When the radial outflow was forced, the shroud caused the viscous moment to increase due to increased shear stress at the outer radius as fluid passed through the shroud clearance. Daniels et al. [17] conducted experiments on adjacent rotating disks

enclosed in a shroud to determine the aerodynamic and torque characteristics. It was found that co-rotating disks exhibited less viscous torque than counter-rotating disks.

Gear theory texts, in fact, only qualitatively handle windage losses. For instance, Townsend [18] identifies a number of factors that influence windage losses. The variables that affect windage include the size, shape, and speed of the rotating elements, the oil-feed system, the overall casing design, the operating temperature and viscosity of the oil, and the pressurization of the casing. Most importantly, he noted that windage effects become important when pitch-line velocities begin to exceed 10,000 ft/min (50 m/s). Townsend also provides a windage approximation formula based on empirical studies of smooth rotating bodies in air, but leaves the determination of windage largely to the experience of the designer.

Anderson and Loewenthal [19, 20] developed an analytic system to calculate all of the losses in a gear train and provided a more sophisticated approximation formula of gear windage based on turbine rotor wheel analysis. However, their work on gear system power losses focused mainly on non-aerodynamic sources of power loss (rolling, sliding, bearing, etc.) and their gear studies involved relatively low-speed gearing. The pitch-line velocities did not exceed 8000 ft/min (40.6 m/s).

The first systematic study of gear windage was performed by Dawson [4] in 1984. He investigated how the geometric properties, speed, and the presence of shrouding affected single isolated gears in air. Experimental measurements were carried out on a set of rather large gears (the root diameters varied between 300 and 1160 mm) in his garage. The gears were constructed of hardboard and designed to allow different tooth geometries to be fitted. Tests were primarily performed on spur gears, but one helical gear was tested as well. The gears were operated in a spin-down test ring where the test gears were accelerated to a maximum rotation speed. The power supply was then disconnected and the gear was allowed to freely decelerate. Windage power loss was calculated by measuring the rate of deceleration. With his test stand, Dawson could achieve root-line velocities up to around 90 m/s (17,900 ft/min) with the 1160 mm diameter gear.

Dawson concluded that the key source of gear windage losses was the teeth. He observed with smoke that the teeth of a spur gear act similarly to those of a centrifugal fan. Air is drawn in axially (from both ends of the teeth) and ejected

out radially. Additionally, he noted that losses could be reduced by up to 41% by simply inhibiting the axial inflow. This was done by placing paper "washers" at the ends of the teeth. The helical gear exhibited quite different behavior, that of an axial fan, when it was similarly observed. Air is drawn in axially and radially from leading edge of the gear teeth and then expelled out axially, radially, and tangentially from the trailing edge. When the edges of the teeth were blocked at both ends or at just the leading edge, windage losses decreased. However, when only the trailing edge was blocked, windage losses actually increased. Figure 1.4 provides sketches by Dawson of the flow patterns he observed.
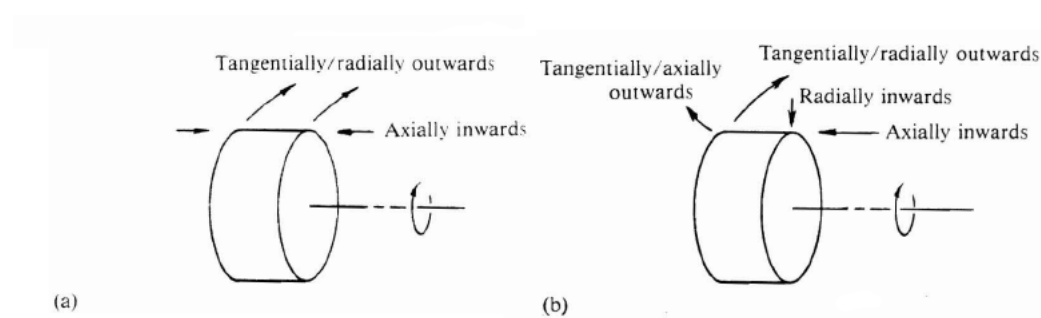
Figure 1.4. Dawson's sketches of the airflow around (a) the spur gear and (b) the helical gear. [4]

Dawson also examined the effect of the gear case, since most gear trains are typically enclosed. Various configurations of axial and radial shrouds of different sizes and shapes were tested. All of the measurements were conducted on a spur gear having the dimensions of 760 mm root diameter, a face width of 187 mm, and a tooth module of 8 mm. Dawson published the power loss for these experiments as a percentage of the power loss experienced by the same gear in free space. The greatest reduction (66%) was seen with the gear completely enclosed in a smooth cylindrical shroud. Dawson, however, did not make any observations of how enclosures actually reduced windage losses but provided an empirical formula for estimating spur gear windage losses that also accounted for shroud effects.

In a follow-up paper [21], Dawson performed further tests on helical gears. In his previous paper, only one helical gear (30° helix angle) was studied, which exhibited 30% less loss than an equivalent spur gear. The gear tests were performed on a gear with a root diameter of 514 mm, a face width of 187.8 mm, and a 16 mm

tooth module. The helix angle of a single gear was varied between 0° and 50°. It was observed that power loss decreased as the helix angle was increased. However, he only presented data for root-line velocities of about 20 m/s (4000 ft/min). Dawson also provided an updated windage formula that accounted for the effects of helix angle.

Following the work of Dawson, Winfree [10] conducted experiments on a single high-speed bevel gear using various baffle configurations. Winfree's focus was on finding an optimal baffle configuration to minimize windage losses of a straight bevel gear. The bevel gear had a diameter of 15 inches and was mounted on a vertical shaft with its face pointed down at the sump. The test rig could achieve pitch-line velocities up to 127 m/s (25,000 ft/min). The test stand was also enclosed so that lubrication system effects could be studied. Windage was calculated by measuring the power draw on the drive motor. With a bevel gear, Winfree observed that there was a significant suction effect at the gear face. Fluid was pumped radially from the inside to the outside through the teeth. Winfree determined that if the pumping ability of the bevel gear could be restrained (e.g. with a shroud) a gear system would become more efficient.

Handschuh and Kilmain [5, 8, 22] investigated the efficiency of a high speed helical gear train and the effects of speed, load, and lubricant jet pressure on operating performance and thermal behaviour. The test rig employed a closed-loop torque regenerative system consisting of two identical gearboxes. One was the test gearbox and the other was set as a slave. Both gearboxes consisted of a input gear, three idlers and a bull gear. Figure 1.5 is an illustration of the test facility. The facility could achieve speeds up 15,000 rpm with pitch-line velocities reaching 24000 ft/min (122 m/s) and loads up to 5000 hp (3730 kW). High rotational speeds had a dramatic effect on efficiency and performance. Windage losses were found to dominate meshing losses when light loads and high speeds were applied to a gear meshing system. Shrouding was also found to be beneficial at the higher operating speeds.

Houjoh et al. [23] instrumented meshing helical gears with pressure transducers to determine the optimal method to supply lubrication to the gear teeth. The transducers were placed in the space between teeth to trace the flow of air across the width of the gears during meshing. Their results showed the axial travel of a
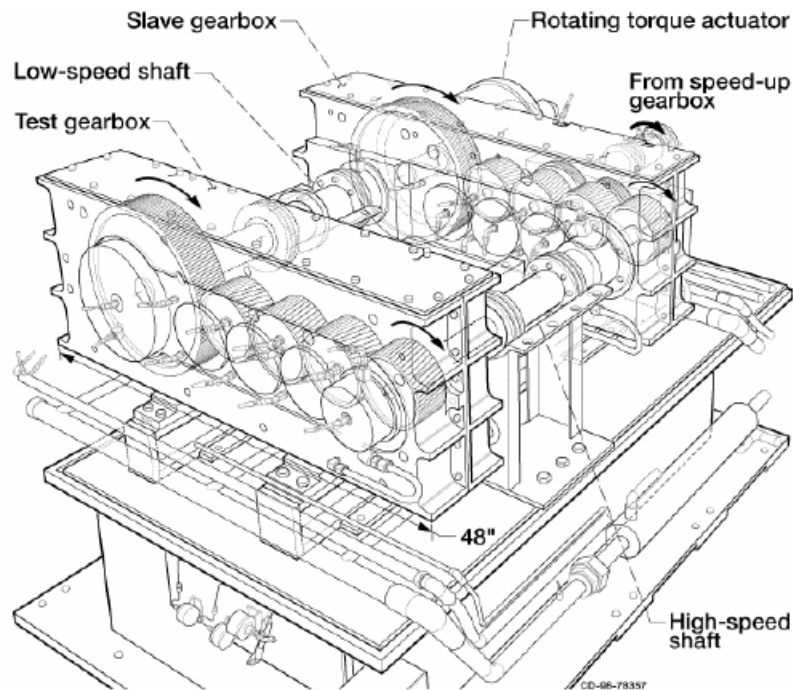
Figure 1.5. NASA High-Speed Helical Gear Train Facility. [5]

strong low pressure wave (what the authors referred to as a negative pressure) as meshing proceeds. It was also observed with helical gears that along with a strong axial flow through the teeth from the leading edge to the trailing edge, there is also an opposite flow from part of the trailing edge. This behavior was not seen by Dawson [4].

In 2004, Diab et al. [6] presented a experimental and numerical study of single, isolated gears rotating in air without an enclosure. Four different spur gears and a disk were tested in a spin-down test rig. The test stand was similar to that of Dawson [4], but it was designed to test industrial components at greater speeds in a more controlled environment. Figure 1.6 is an illustration of the test rig. The gears varied in diameter, width, and module and Table 1.1 lists the properties of the gears and the disk that were studied. The experimental results were also used to evaluate the windage estimation formulas of Anderson and Loewenthal [19], Dawson [4], and those developed by Diab et al. The formulas developed by Diab showed improved

results over the older formulas for the gears in the study. Dawson's formula over-predicted the power losses for all cases, and Anderson and Loewenthal's under-predicted windage for the smaller gears. Subsequent papers from these authors [24, 25] focused on modeling the pumping losses from the meshing of the gear teeth.
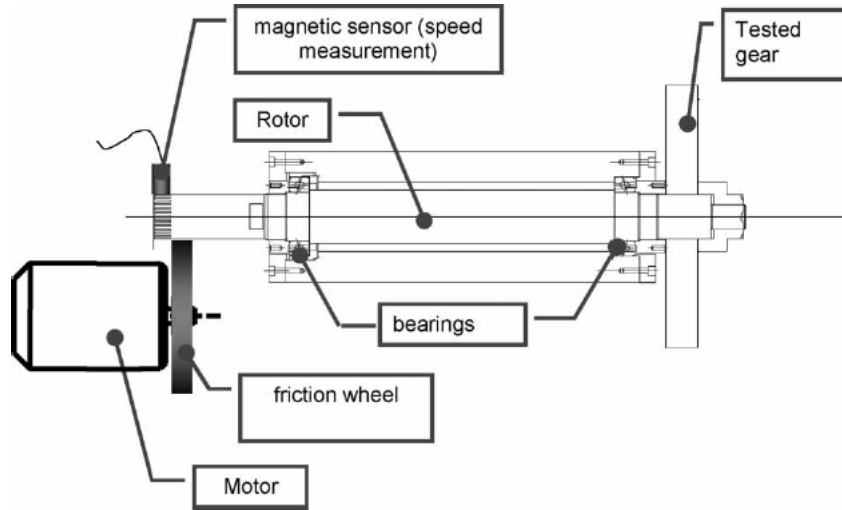
Figure 1.6. Diab Test Rig. [6]

Table 1.1. Diab Gear Properties.

	Pitch Diameter (mm)	Tooth Width (mm)	Module (mm)	Teeth
Gear 1	288	30	4	72
Gear 2	144	30	4	36
Gear 3	144	60	4	36
Gear 4	144	60	6	24
Disk	300	30		

Johnson et al. [26] studied the effects of shrouding on a spiral bevel gear mesh test rig. Through transparent shrouding, Johnson observed that the air and oil phases remained separate, indicating that analysis based on average fluid density may not be physical. Lubrication was also found to reduce the effectiveness of shrouding.

Seetharaman and Kahraman [27] proposed a physics-based model to predict windage losses on meshed spur gears. In their model, windage losses were the sum

of the aerodynamic drag losses associated with the individual gears and the losses due to compression or trapping of the atmospheric medium between meshing gear teeth. In this model, however, it was the compression losses in the meshing region that were seen as the dominant source of windage losses, not the aerodynamic drag forces. Their model was validated against windage data of two meshed spur gears from Petry-Johnson et al. [28]. They did not validate their model against data of isolated gears and the dominance of compression losses has not been seen by others [25].

Due to the complexities of the physics and geometries involved, it is only recently that modern computational fluid dynamic (CFD) methodologies have been employed in analysing gear windage. Farrall et al. [29] used the commercial unstructured CFD solver FLUENT to obtain a steady-state, single phase solution for a shrouded bevel gear. Farrall attempted to computationally replicate the work of Winfree, but calculated dramatically less windage reduction from shrouding than did Winfree. This is likely due to the fact that Farrall did not study the same gear or shroud design as Winfree.

Al-shibli et al. [30] performed a 2-D study of a spur gear using FLUENT. The model domain consisted of two teeth and a side correlation factor adopted from Townsend [18] was used to to account for 3-D effects (although these authors state that work is under way to extend their simulations to 3-D [31]). Ref. [31] also provides a fairly comprehensive review of the study of gear windage. Computations were validated against data from experiments performed by Lord [32], but the side correlation function actually predicted nearly 40% of the losses.

Hill et al. [33] implemented a 3-D unstructured moving mesh method and applied it to isolated spur gears in air and validated their predictions against data from Diab et al. [6] Marchesse et al. [34] followed the same approach as Al-shibli et al. [30], but used a structured grid with the flow solver ANSYS CFX. However, Marchesse et al. did not find the 2-D approach to be satisfying. The 2-D model was then extended into three dimensions, and it was found that a 3-D CFD approach produced significantly improved calculations of gear windage losses. Their CFD results produced flow patterns similar to those obtained by Hill et al.. Imai et al. [35] investigated 3-D bevel gears in mesh in an air-oil atmosphere, but modeled the gears as porous bodies.

1.3 Modeling Gear Windage Loss

The simplest way to model the flow around a rotating gear is to neglect the effect of the teeth and treat the gear as a simple disk. Schlichting [13] provides an exact solution of the Navier-Stokes equations for the flow around a rotating disk. Schlichting derives the frictional moment (M) of a disk in laminar flow and wetted on both sides as:

$$2M = 0.616\pi\rho R^4(\nu\omega^3)^{1/2} \tag{1.5}$$

For turbulent flows, the viscous torque on the disk is written as:

$$2M = 0.073\pi\omega^2 R^5(\nu/\omega\ R^2)^{1/5} \tag{1.6}$$

where ρ is density, R is radius, ν is kinematic viscosity, and ω is the angular velocity. These solutions only provide the minimum estimate of the windage drag since both edge effects and pressure effects are neglected.

The windage estimation formula provided by Townsend [18] is based on empirical studies of smooth rotating bodies in air. The formula provides an approximation of windage power loss in horsepower:

$$P = \frac{15}{0.746}\left(\frac{n}{1000}\right)^3\left(\frac{D}{1000}\right)^4\left(\frac{5L}{100} + \frac{D}{100}\right) \tag{1.7}$$

where n is rotation speed in revolutions per minute, D is the diameter (inches) of the rotating body, and L is the length (inches) of the body. Equation 1.7 completely neglects the influence of the teeth and only provides a minimum estimate for windage. This equation, though, has two parts that account for the losses from the gear face and the losses from the periphery. Equation 1.8 represents the losses from the periphery:

$$P = \frac{15}{0.746}\left(\frac{n}{1000}\right)^3\left(\frac{D}{1000}\right)^4\left(\frac{5L}{100}\right) \tag{1.8}$$

and it assumes that the outer surface is smooth. Townsend provides a modification to account for the presence of gear teeth on the surface. This is shown in Equation 1.9 where the effect of the teeth are treated with a rough surface adjustment

factor, R_f, that is a function of diametral pitch (coarser pitched gears will have a higher roughness factor):

$$P = \frac{15}{0.746} \left(\frac{n}{1000}\right)^3 \left(\frac{D}{1000}\right)^4 \left(\frac{5L}{100}\right) \left(\frac{R_f}{\sqrt{tan\Psi}}\right) \tag{1.9}$$

Ψ is the helix angle and adjusts the losses for differences in helix angle. Appropriate values of R_f can be found in Table 12.5 of Reference [18].

The analytical formula provided by Anderson and Loewenthal [19] is based on turbine rotor wheel analysis where windage power losses (Watts) are calculated with Equation 1.10:

$$P = C_1 \left(1 + 2.3\frac{t}{R}\right) \rho^{0.8} n^{2.8} R^{4.6} \mu^{0.2} \tag{1.10}$$

where C_1 is a constant (2.04×10^{-8} in S.I. units), t is the gear face width (meters), R is the pitch radius (meters), n is rotation rate in revolutions per minute, and ρ and μ are the density (kg/m^3) and viscosity (centipoise), respectively, of the atmosphere. To account for the oil atmosphere within the gearbox, the density and viscosity of the atmosphere was corrected to reflect a 34.25 parts air to 1 part oil combination as reported in Reference [36]. Their expression became:

$$P_W = C_2 \left(1 + 2.3\frac{t}{R}\right) n^{2.8} R^{4.6} \left(0.028\mu + C_3\right)^{0.2} \tag{1.11}$$

where C_2 and C_3 are 2.82×10^{-7} and 0.019, receptively. This equation, however, does not account for the properties (diametral pitch, helix angle, etc.) of the gear teeth.

Dawson [4] developed his own formula for gear windage power losses based on his own empirical studies. He defined windage as a function of the rotation speed N (RPM), the root diameter D of the gear (mm), the face width F (mm), and the tooth module M (mm):

$$P = N^{2.9}(0.16D^{3.9} + D^{2.9}F^{0.75}M^{1.15}) \times 10^{-20}\Phi\lambda \tag{1.12}$$

where Φ represents an unknown function of the effective density of the air-oil

atmosphere ($\Phi = 1$ indicates an oil free atmosphere). The λ term represents the effect of the gear case. A λ of unity is for a gear operating in free space, 0.6-0.7 is for a gear in a large enclosure, and 0.5-0.6 is for tighter enclosures. He accounted for the helix angle in his updated formula [21]:

$$P = 1.12 \times 10^{-8} C' \rho N^{2.85} D^{4.7} \nu^{0.15} \lambda \tag{1.13}$$

where ν is the kinematic viscosity (m^2/s) and C' represents a shape factor based on the face width to diameter ratio and the number of teeth the gear possesses. Figures 3 and 5 of Reference [21] provide the shape factors for spur gears and helical gears, respectively. The root diameter, D, is in meters. Both Equations 1.12 1.13 provided windage power loss in kilowatts.

The formula presented by Diab et al. [6] calculated power loss in Watts as a function of fluid density ρ (kg/m^3), rotation rate ω (rad/s), pitch radius R (m) and a total windage loss coefficient C_t:

$$P = \frac{1}{2} C_t \rho \omega^3 R^5 \tag{1.14}$$

where two different formulas were provided to calculate C_t. The first formula was based on a dimensional analysis:

$$C_t = \alpha \text{Re}^\beta \left(\frac{b}{R} \right)^\gamma Z^\delta \left\{ \left(\frac{h_1}{R} \right)^\psi + \left(\frac{h_2}{R} \right)^\psi \right\} \tag{1.15}$$

where R, b, and Z are the geometrical gear parameters pitch radius, width, and number of teeth, respectively. α, β, γ, δ, and ψ are constant coefficients that are derived experimentally. The parameters $h_{1,2}$ are used to account for the presence of flanges near the teeth. When there is no obstacle on the side of the gear $h_{1,2} = 0.5^{1/\psi} R$.

The second approach was based on a fluid flow analysis. The power loss coefficient ($C_t = C_f + C_l$) was divided between the losses from the gear face (C_f)and from the gear teeth (C_l). The gear face contribution is given by Equation 1.16:

$$C_f = \frac{2n_1 \pi}{5 - 2m_1} \frac{1}{\text{Re}^{*m_1}} \left(\frac{R^*}{R} \right)^5 + \frac{2n_2 \pi}{5 - 2m_2} \left[\frac{1}{\text{Re}^{m_2}} - \frac{1}{\text{Re}^{*m_2}} \left(\frac{R^*}{R} \right)^5 \right] \tag{1.16}$$

where n_1 and m_1 are coefficients for laminar flows and have the values of 1.293 and 0.5, respectively. The coefficients n_2 and m_2 are for turbulent flows and have values of 0.072 and 0.2, respectively. Re^* is the critical Reynolds number ($\cong 3 \times 10^5$) between laminar and turbulent flow. R is the pitch radius and $R^* = \sqrt{\mu \mathrm{Re}^*/\rho\omega}$ is the critical radius separating the laminar and turbulent regions. The tooth contribution coefficient is given by Equation 1.17:

$$C_l \cong \xi \frac{Z}{4} \left(\frac{b}{R} \right) \left[1 + \frac{2(1 + X_A)}{Z} \right]^4 (1 - cos\phi)(1 + cos\phi)^3 \qquad (1.17)$$

X_A represents the profile shift coefficient and ϕ is computed from the formula

$$\phi = \pi/Z - 2(\mathrm{inv}(\alpha_P) - \mathrm{inv}(\alpha_A)) \qquad (1.18)$$

where α_P and α_A are the pressure angles at the pitch point and tooth tip, respectively. The tooth analysis assumed that the fluid is expelled from an active tooth area and that the pressure is uniform on the tooth. This has not been seen by the author [33] or others [30, 31].

Figure 1.7 compares the windage approximation formulas for a simple 13 in. pitch diamter spur gear. The gear is 1.12 inches wide and the teeth have 25° pressure angle. At the higher rotational speeds the differences between estimates becomes quite pronounced. Figure 1.7 was produced by the Python program provided in Appendix A.

1.4 Physics

The flow physics inside a gearbox are quite complex. Gears are not designed to be aerodynamically efficient. The shape and profile of the gear teeth has an important function in transferring power between gears. Variations in angular velocity of the driven gear will lead to vibrations in the gear train and will generally cause fatigue cracks to form in the teeth resulting in early failure of the gear.

Unlike a smooth rotating disk, pressure torque on the teeth will play in important role in calculating the windage drag on gears. The teeth are also located at the periphery of the gear where speeds are greatest (speed $= \omega \times r$). It is very pos-
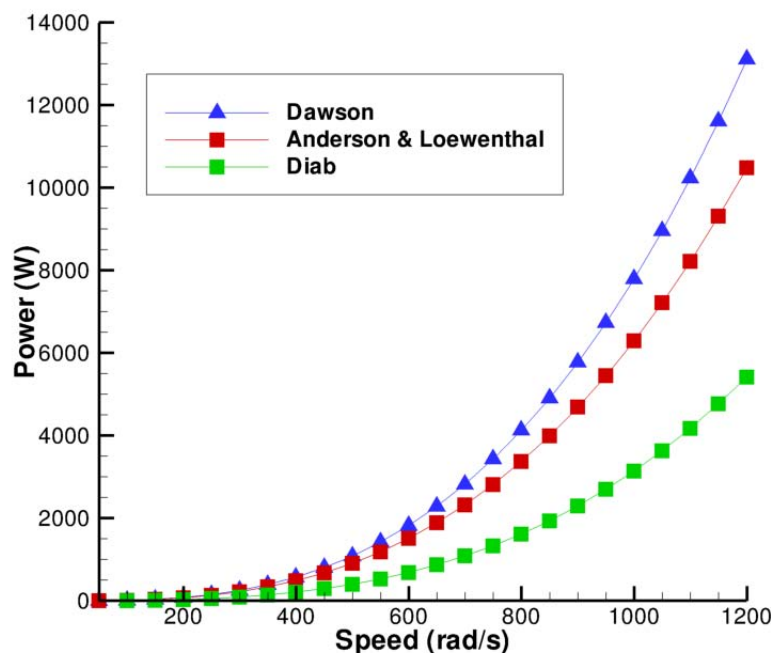
Figure 1.7. Gear windage loss estimates for a 13-inch pitch diameter spur sear

sible that depending on the rotation rate and the size of the gear, gear tip speeds can enter the the range of compressible flow. Compressible flow effects typically become noticeable above Mach numbers of 0.3. However, sonic speed is affected by both the temperature and the composition (air-only versus air-oil) of the fluid environment. Brennen [37] showed that the sonic velocity of a homogeneous mixture (e.g. air and only) can be much smaller than that of either of its constituents, meaning that compressibility effects could be be a concern at lower speeds than an air-only analysis would indicate. The teeth also introduce turbulence into the flow. Gear teeth are not designed to pass smoothly through the air. Their faces present a blunt surface in the direction of the direction of rotation.

The behavior of the air flow is also affected by the orientation of the teeth with respect to the axis of rotation. The face of spur gear teeth are oriented parallel to the axis of rotation while helical gear teeth are aligned along a helix at an angle to the axis of the shaft. As was shown in Figure 1.4, it was observed that spur and helical gears generate different flow patterns.

Moving away from the effects of simple isolated gears, there is also the fact that gears operate in mesh with or in close proximity to other gears. Diab et al. [24] noted the possibility of sonic conditions existing within the tooth mesh region. There is also the effect of the enclosure that needs to be considered. The gear train studied by Handschuh and Kilmain [5, 8, 22] was enclosed in a relatively tight (axially) enclosure, but additional radial shrouding was found to be necessary to reduce losses.

Finally, there is the issue that meshing gears require lubrication. In high-speed gear trains (pitch-line speeds above 10,000 ft/min) lubrication is used to both reduce frictional losses between meshing teeth and to cool the gears. A significant amount of heat is generated by frictional forces acting in the meshing region [5]. In high-speed gearing applications, lubrication is applied to the gears by an oil spray system. As oil mist is sprayed on the gears, it builds up the oil film layer on the teeth that is used to reduce meshing frictional losses. Immediately after meshing, the gears are sprayed again to dissipate the heat generated by meshing. Lubrication has to be continuously applied because centrifugal forces fling the oil off the gear shortly after its application. The fluid mechanics of these systems thus consists of highly turbulent air flow, disperse oil phase flow from the spray system and oil fling-off, and continuous oil phase lubricating films on the gears.

1.5 Challenges

The complex physics involved in gear windage provide several challenges for CFD analysis methods. The fluid mechanics involve complex separated air flow, disperse multiphase flow (oil droplets) and continuous multiphase films (lubricating oil on gears), moving boundaries in contact, and all modes of heat transfer. The complex internal geometries of the gearbox and the relative motion of the gears also necessitate that a CFD solver support either adaptive grids or overset grid systems.

With respect to the fluid mechanics, the CFD solver must be able to support suitable turbulence modeling to accommodate the highly separated flows within the gearbox and the cascade of energy through turbulence scales into viscous heating. Viscous dissipation is critical in this case since it is often neglected in many CFD

analyses. An oil-out condition exacerbates many of these challenges. In the oil-out condition, all modes of heat transfer (conduction, convection, radiation) are present and need to be accounted for in the CFD model. These flows are also highly unsteady, non-aerodynamic high-Reynolds number flows ($\rho R2\Omega/\mu \cong O(10^6)$). In the most extreme cases, gears can have tip velocities close to a Mach number of 0.75, which means compressible flow effects will be present.

The solver also needs to contain a non-equilibrium multiphase capability that can accommodate the disperse mist/droplet phase and the continuous film phases to model the multiphase flow dynamics. Johnson et al. [26] indicated that simply modeling the air-oil atmosphere as a homogeneous fluid may not be physical. The relative importance of 1-phase and 2-phase physics in windage losses is still not well known.

Finally, there is a paucity of validation data. There are only a handful of experimental cases [10, 4, 6] in the open literature that provide enough useful data for CFD validation. In the cases that are available, there is little data on the flow itself. Typically, only power loss or temperature data is reported. Velocity field data is nearly impossible to obtain because of the high velocities involved, and the fact that lubrication tends to obscure optical measurement equipment. Also fitting measuring equipment into a tightly enclosed gear space presents its own issues. There are only two of cases that provide any kind of pressure data [7, 23].

1.6   Objectives of Dissertation

This research has a number of objectives with respect to gear windage. The first is to develop numerical modeling approaches for the application of gear windage aerodynamics. The second goal is to use these methods to develop physical understanding of gear windage aerodynamics, loss mechanisms, and loss mitigation strategies. Additionally, it is expected that new approaches for minimizing windage loss can be developed and evaluated through an understanding of the physics and the numerical tools presented here. Finally, validation of the method is key to relying on "computational discovery" elements of these objectives and date from the open literature and the new NASA Glenn Gear Windage Test Facility will be used to validate the approaches presented in this dissertation.

1.7 Organization of Dissertation

The dissertation is organized as follows. Chapter 1 has introduced the problem of gear windage and previous work on the subject. Chapter 2 reports the governing equations and numerical procedures. Next, Chapter 3 describes the work done to validate the numerical procedures. In Chapter 4, a series of numerical studies are performed that provide insight into several of the physical mechanisms of windage losses including the role of gear shrouding. This is followed by an overview of the NASA Glenn Gear Windage Test Facility along with a selection of data obtained to date. CFD simulation of the NASA Glenn windage loss tests are presented and a discussion of these comparisons is provided. This is followed by the results of a numerical experiment, guided by the findings described in the dissertation, that demonstrate a benefit in windage performance beyond that observed with shrouds alone. Finally, Chapter 5 presents a summary of the results, conclusions, and suggestions for future work.

Chapter 2

Theoretical Formulation

Two different CFD codes are used in this research. The first is NPHASE-PSU which is a time accurate, unstructured, overset multiphase flow solver. In all NPHASE-PSU simulations the entire gear is modeled, which allows for the study of complex gearbox geometries and bodies in relative motion. The second CFD code is OVER-REL. OVER-REL is a steady-state, incompressible, block-structured, overset flow solver. Only one gear tooth/"blade row" is modeled using this solver providing for a very efficient and numerically accurate physics analysis of gear windage aerodynamics. The governing equations and the numerical methods used in these two codes will be discussed further in this chapter. In this dissertation, all verification and validation flow studies are either incompressible, or have maximum local absolute Mach numbers of less than 0.35. The available data [4, 38, 10, 6] shows that windage losses already become significant at low subsonic tip Mach numbers. Accordingly, for all simulations presented here, an incompressible assumption is invoked and the energy equation is not solved.

2.1   NPHASE-PSU

NPHASE-PSU [39] is a parallel, face-based, arbitrary-element, unstructured multiphase flow solver that has been instrumented with overset mesh capability. The baseline algorithm follows established segregated pressure based methodology. A collocated variable arrangement is used and a lagged coefficient linearization is applied [40]. Diagonal dominance preserving, finite volume spatial discretization

schemes are used for the scalar transport equations. Continuity is introduced through a pressure correction equation, based on the SIMPLE-C algorithm [41]. In constructing cell face fluxes, a momentum interpolation scheme [42] is used which introduces damping in the continuity equation. Grid motion/deformation terms are implemented in a Geometric-Conservation-Law (GCL) preserving fashion [43]. A dual-time formulation is usedwhere at each physical timestep, between 5 and 20 pseudo-timesteps of the SIMPLE-C algorithm are applied. Specifically, at each pseudo-timestep, the discrete momentum equations are solved approximately (using a simple point iterative scheme), followed by a more exact solution of the pressure correction equation (using the PETSC [44] parallel LU preconditioning and GMRES utilities). Turbulence scalar and energy equations are then solved in succession. Parallelization is implemented in a standard fashion by invoking domain decomposition based on METIS [45] in a pre-processing step, and MPI-based message passing in the CFD code. A high-Reynolds number k-ϵ turbulence model and a sublayer resolved hybrid k-ϵ/k-ω turbulence model due to Menter [46] are used in the studies that follow. No explicit transition model was employed as justified, for now, by the small contribution of near-axis viscous torques on windage loss.

2.1.1 Governing Equations

The equations for the conservation of mass (Equation 2.1), momentum (Equation 2.2) and energy (Equation 2.3) can be written in integral conservation law form for a unsteady compressible flow as:

$$\frac{\partial}{\partial t} \int_\forall \rho d\forall + \int_{\vec{S}} \rho \vec{V} \cdot d\vec{S} = 0 \tag{2.1}$$

$$\frac{\partial}{\partial t} \int_\forall \rho \vec{V} d\forall + \int_{\vec{S}} \rho \vec{V} \vec{V} \cdot d\vec{S} = -\int_{\vec{S}} p d\vec{S} + \int_{\vec{S}} \underline{\underline{\tau}} \cdot d\vec{S} \tag{2.2}$$

$$\frac{\partial}{\partial t} \int_\forall \rho E d\forall + \int_{\vec{S}} \rho H \vec{V} \cdot d\vec{S} = \int_{\vec{S}} \left(\underline{\underline{\tau}} \cdot \vec{V} \right) \cdot d\vec{S} + W_f + q_H \tag{2.3}$$

where $\vec{V}$ is the velocity vector, ρ is the fluid density, p is pressure, $\underline{\underline{\tau}}$ is the stress tensor, q_H is the heat added to the control volume, and W_f represents the work done on the control volume. Since all verification and validation flow studies are either incompressible, or have maximum local absolute Mach numbers of less than 0.35, an incompressible assumption is invoked for all simulations and the energy equation is not solved. Future studies will require the use of the compressible flow formulation of the governing equations.

A high-Reynolds number k-ϵ turbulence model and a sublayer resolved hybrid k-ϵ/k-ω turbulence model due to Menter [46] are used. The model transport equations for k and ϵ are:

$$\frac{\partial}{\partial t} \int_\forall \rho k d\forall + \int_{\vec{S}} \rho k \vec{V} \cdot d\vec{S} = \int_{\vec{S}} \left(\mu + \frac{\mu_t}{\mathrm{Pr}_k} \right) \nabla k \cdot d\vec{S} + \int_\forall (P - \rho\epsilon)\, d\forall \qquad (2.4)$$

$$\frac{\partial}{\partial t} \int_\forall \rho\epsilon d\forall + \int_{\vec{S}} \rho\epsilon \vec{V} \cdot d\vec{S} = \int_{\vec{S}} \left(\mu + \frac{\mu_t}{\mathrm{Pr}_\epsilon} \right) \nabla\epsilon \cdot d\vec{S} + \int_\forall (C_1 P - C_2 \rho\epsilon) \frac{\epsilon}{k} d\forall \quad (2.5)$$

2.1.2 Grid Motion

In the case of moving bodies (e.g. rotating gears), the solution domain will change with time due to the movement of the boundaries. Therefore, the grid also has to move to accommodate the movement of the boundaries. Using Cartesian velocity components in the absolute frame of reference (coordinate system remains fixed), the only change in the equations of motion is the appearance of the relative velocity in the convective terms. If we consider the 1-D continuity equation, for example:

$$\frac{\partial\rho}{\partial t} + \frac{\partial\rho u}{\partial x} = 0 \qquad (2.6)$$

By integrating Equation 2.6 over a control volume whose boundaries move with time from $x_1(t)$ to $x_1(t)$ it becomes:

$$\int_{x_1(t)}^{x_2(t)} \frac{\partial\rho}{\partial t} dx + \int_{x_1(t)}^{x_2(t)} \frac{\partial\rho u}{\partial x} dx = 0 \qquad (2.7)$$

After applying Leibniz's rule to the first term and integrating the second, the continuity equation becomes:

$$\frac{d}{dt} \int\limits_{x_1(t)}^{x_2(t)} \rho dx - \left[\rho_2 \frac{dx_2}{dt} - \rho_1 \frac{dx_1}{dt} \right] + \rho_2 u_2 - \rho_1 u_1 = 0 \qquad (2.8)$$

The dx/dt terms describe the velocities with which the grid moves. The terms in the square brackets share a form similar to the last two terms involving the fluid velocity which allows Equation 2.7 to be rewritten as:

$$\frac{d}{dt} \int\limits_{x_1(t)}^{x_2(t)} \rho dx + \int\limits_{x_1(t)}^{x_2(t)} \frac{\partial}{\partial x} \left[\rho(u - u_b) \right] dx = 0 \qquad (2.9)$$

To further simplify terms, dx/dt has been rewritten as u_b. This analysis can be extended into three dimensions by using the 3-D version of Leibnitz's rule. Thus, the conservation of mass, momentum and energy can be written for a compressible flow through a moving mesh in integral conservation law form as:

$$\frac{\partial}{\partial t} \int\limits_{\forall} \rho d\forall + \int\limits_{\vec{S}} \rho \left(\vec{V} - \vec{W} \right) \cdot d\vec{S} = 0 \qquad (2.10)$$

$$\frac{\partial}{\partial t} \int\limits_{\forall} \rho \vec{V} d\forall + \int\limits_{\vec{S}} \rho \vec{V} \left(\vec{V} - \vec{W} \right) \cdot d\vec{S} = -\int\limits_{\vec{S}} p d\vec{S} + \int\limits_{\vec{S}} \underline{\underline{\tau}} \cdot d\vec{S} \qquad (2.11)$$

$$\frac{\partial}{\partial t} \int\limits_{\forall} \rho E d\forall + \int\limits_{\vec{S}} \rho H \left(\vec{V} - \vec{W} \right) \cdot d\vec{S} = \int\limits_{\vec{S}} \left(\underline{\underline{\tau}} \cdot \vec{V} \right) \cdot d\vec{S} + W_f + q_H \qquad (2.12)$$

where $\vec{W}$ is the velocity of the surface element, $d\vec{S}$, in the absolute frame of reference.

2.1.3   Multiphase Flow Methods

The issue of gear windage cannot be completely studied by only considering an air-only environment. Gears operate in an environment of both air and oil. Gears require lubrication to reduce friction during meshing and to provide cooling. A

multiphase flow approach will thus needed to model the air and oil environment and this is why NPHASE-PSU was selected.

Accurate predictions of multiphase flows can only be made if the overall CFD model uses mechanistically-based closure laws for the various local phenomena. These models describe the interfacial mass, momentum and energy transfer between the fields. There is a hierarchy of approaches to model such flows [37]. The simplest method is to treat the air and oil atmosphere as a homogeneous mixture where all of the phases are in dynamic and thermodynamic equilibrium. The next approach is the Eulerian two-fluid method where each phase is treated as a continuum with separate velocity and temperature fields. Finally, there is the Lagrangian approach (or trajectory models) where the motion of the disperse phases is assessed by following either the motion of the actual particles or the motion of larger, representative particles. Both the homogeneous mixture method and the Eulerian two-fluid method are available in NPHASE-PSU.

2.1.3.1   Two-Fluid Eulerian Formulation

The single-pressure ensemble averaged continuity and momentum equations are cast in conservation law form as:

$$\frac{\partial}{\partial t}(\alpha^k \rho^k) + \frac{\partial}{\partial x_j}(\alpha^k \rho^k u_j^k) = \sum_{k \neq 1}(\Gamma^{lk} - \Gamma^{kl}) \qquad (2.13)$$

$$\begin{aligned}
\frac{\partial}{\partial t}(\alpha^k \rho^k u_i^k) + \frac{\partial}{\partial x_j}(\alpha^k \rho^k u_i^k u_j^k) &= -\alpha^k \frac{\partial p}{\partial x_i} + \frac{\partial}{\partial x_j}\left[\alpha^k \mu_t^k \left(\frac{\partial u_i^k}{\partial x_j} + \frac{\partial u_j^k}{\partial x_i}\right)\right] \qquad (2.14) \\
&+ \alpha^k \rho^k g_i + M_i^{kl} + \sum_{k \neq 1}(D^{kl}[u_i^l - u_i^k] + \Gamma^{lk}u_i^l - \Gamma^{kl}u_i^k)
\end{aligned}$$

Γ^{kl} is the mass transfer rate from field k to field l. D^{kl} is the drag force coefficient and M_i^{kl} represents the non-drag interfacial force of field k arising from the interface with field l. In general each field, k, will have a different density, volume fraction, velocity, and viscosity. α^k is the volume fraction for field k. Ensemble averaging is achieved by repeating the measurement at a fixed-time and position for a large number of systems with identical macroscopic properties (velocity, tem-

perature) and boundary conditions, and finding the mean values of the results. For compressible flows and flows with heat transfer, it is necessary to solve an energy equation. An enthalpy transport equation for each field is written as

$$\frac{\partial}{\partial t}(\alpha^k \rho^k h^k) + \frac{\partial}{\partial x_j}(\alpha^k \rho^k u_j^k h^k) = \frac{\partial}{\partial x_j}\left[\alpha^k\left(\mu^k + \frac{\mu_t^k}{\sigma_h^k}\right)\frac{\partial h^k}{\partial x_j}\right] + S_h^k \qquad (2.15)$$

In the context of multifield flows, separate turbulence transport scalars are solved for each field. For example, the high Reynolds number k-ϵ model is written:

$$\begin{aligned}
\frac{\partial}{\partial t}(\alpha^k \rho^k k^k) + \frac{\partial}{\partial x_j}(\alpha^k \rho^k u_j^k k^k) &= \frac{\partial}{\partial x_j}\left[\alpha^k\left(\mu^k + \frac{\mu_t^k}{\sigma_k^k}\right)\frac{\partial k^k}{\partial x_j}\right] \\
&+ P^k - \alpha^k \rho^k \epsilon^k + S_k^k \qquad (2.16)\\
\frac{\partial}{\partial t}(\alpha^k \rho^k \epsilon^k) + \frac{\partial}{\partial x_j}(\alpha^k \rho^k u_j^k \epsilon^k) &= \frac{\partial}{\partial x_j}\left[\alpha^k\left(\mu^k + \frac{\mu_t^k}{\sigma_\epsilon^k}\right)\frac{\partial \epsilon^k}{\partial x_j}\right] \\
&+ C_1\frac{\epsilon^k}{k^k}P^k - C_2\frac{\epsilon^k}{k^k}\alpha^k \rho^k \epsilon^k + S_\epsilon^k \qquad (2.17)
\end{aligned}$$

where S_k and S_ϵ are available source/sink terms to extract turbulence energy associated with breakup and and modify production due to interface dynamics and mass transfer mechanisms [48].

2.1.3.2   Homogeneous Multiphase Formulation

For homogeneous multiphase flow, it is assumed that the fields are in dynamic and thermodynamic equilibrium allowing equations 2.13 and 2.14 to reduce to:

$$\frac{\partial}{\partial t}(\alpha^k \rho^k) + \frac{\partial}{\partial x_j}(\alpha^k \rho^k u_j^k) = \sum_{k\neq 1}(\Gamma^{lk} - \Gamma^{kl}) \qquad (2.18)$$

$$\frac{\partial}{\partial t}(\rho^m u_i^m) + \frac{\partial}{\partial x_j}(\rho^m u_i^m u_j^m) = -\frac{\partial p}{\partial x_i} + \frac{\partial}{\partial x_j}\left[\mu_t^k\left(\frac{\partial u_i^m}{\partial x_j} + \frac{\partial u_j^m}{\partial x_i}\right)\right] + \rho^m g_i \qquad (2.19)$$

where the set of momentum equations is reduced to a single equation for the mixture. The superscript m represents the mixture quantities. In equations 2.18-2.19, a high Reynolds number for the viscous term is assumed with dilation and turbulence energy terms neglected.

2.2 OVER-REL

OVER-REL is a parallel, cell-centered, incompressible, finite-volume code based on structured overset multi-block grids and the time-marching, pseudo-compressibility formulation of Chorin [49]. The inviscid fluxes are formulated from the Roe approximate Riemann solver [50] and extended to third-order accuracy through the MUSCL scheme [51]. Second-order accurate central differences are used for the viscous fluxes. Numerical derivatives are used to calculate the flux Jacobians. A symmetric Gauss-Seidel method is applied to solve the resulting linear system of equations. In the present application, the code's turbomachinery analysis instrumentation is used; all simulations are carried out for a single gear tooth, with periodic boundary conditions, in a non-inertial frame-of-reference rotating with the gear. OVER-REL does not support compressible flow, multiphase flow, or unstructured meshes (necessary for complex gearbox geometries). However, it is better suited than NPHASE-PSU for physics exploration analyses due to its efficiency for cases where a single "blade-row"/gear tooth can be used (i.e., axisymmetric shroud).

2.2.1 Governing Equations

As will be shown, much can be learned from systems that are either shroud-free or have completely axisymmetric shrouds (i.e., fully enclosed radial shrouds). So we can consider single-tooth domains that are periodic and steady in the frame of reference of the rotating gear. The conservation of mass and momentum can be written in integral conservation law form for a system rotating with constant angular velocity $\vec{\omega}$ as:

$$\int_{\vec{S}} \rho \vec{V} \cdot d\vec{S} = 0 \tag{2.20}$$

$$\int_{\vec{S}} \rho \vec{V} \vec{V} \cdot d\vec{S} = - \int_{\vec{S}} p d\vec{S} + \int_{\vec{S}} \underline{\underline{\tau}} \cdot d\vec{S}$$

$$- \int_\forall \rho \vec{\omega} \times (\vec{\omega} \times \vec{r}) \, d\forall - \int_\forall 2\rho \left(\vec{\omega} \times \vec{V} \right) d\forall \qquad (2.21)$$

where $\vec{V}$ is the velocity vector in the relative frame of reference. The last two terms on the right-hand side of Equation 2.21 represent the apparent centrifugal and Coriolis forces, respectively.

It was shown in Hill et al. [33] that a sublayer-resolved two-equation turbulence model performed better than a high-Reynolds number form with wall-functions in predicting viscous losses on a spinning disk. Therefore, with this formulation of the governing equations $\underline{\tau} = (\mu + \mu_t)(\nabla \underline{V} + (\nabla \underline{V})^T)$ is adopted and a sublayer resolved q-ω turbulence model due to Coakley [52] is employed. The q-ω model in OVER-REL was selected because it has been validated for a number of turbomachinery applications. Unlike NPHASE-PSU, OVER-REL does not have a k-ϵ turbulence model. The dependent variables in this model are related to the turbulence kinetic energy, k, and the turbulence dissipation rate, ϵ, through $q = \sqrt{k}$ and $\omega = \epsilon/k$. In this model, the eddy viscosity is obtained from:

$$\mu_t = \rho C_\mu D q^2 / \omega \qquad (2.22)$$

where $C_\mu = 0.09$ and D is the near wall damping function:

$$D = 1 - e^{-\alpha \rho q d_n / \mu} \qquad (2.23)$$

where $\alpha = 0.02$ and d_n is a measure of the normal distance to the nearest wall. The modeled transport equations for q and ω are:

$$\int_{\vec{S}} \rho q \vec{V} \cdot d\vec{S} = \int_{\vec{S}} \left(\mu + \frac{\mu_t}{\mathrm{Pr}_q} \right) \nabla q \cdot d\vec{S} + \int_\forall \frac{\rho q}{2} \left(C_\mu D \frac{S}{\omega} - \omega \right) d\forall \qquad (2.24)$$

$$\int_{\vec{S}} \rho \omega \vec{V} \cdot d\vec{S} = \int_{\vec{S}} \left(\mu + \frac{\mu_t}{\mathrm{Pr}_\omega} \right) \nabla \omega \cdot d\vec{S} + \int_\forall \rho \left(C_1 C_\mu S - C_2 \omega^2 \right) d\forall \qquad (2.25)$$

where $C_1 = 0.405D + 0.045$, $C_2 = 0.92$, $\mathrm{Pr}_q = 1.0$, and $\mathrm{Pr}_\omega = 1.3$ and S represents the strain rate invariant.

In a axisymmetric gear system, the overall size of the grid domain can signifi-

cantly reduced by only gridding one tooth passage instead of many. This is done by using periodic boundary conditions. Figure 2.1 illustrate the use of periodic boundaries in a axisymmetric gear case. The area colored in green represents the one tooth passage that is included in the computational domain. The blue region represents the rest of the gear that is left out. The red lines indicate the periodic boundaries of the domain. With periodic boundary conditions, the flux of all flow variables at one periodic boundary is set to equal the flux at the opposite periodic boundary.
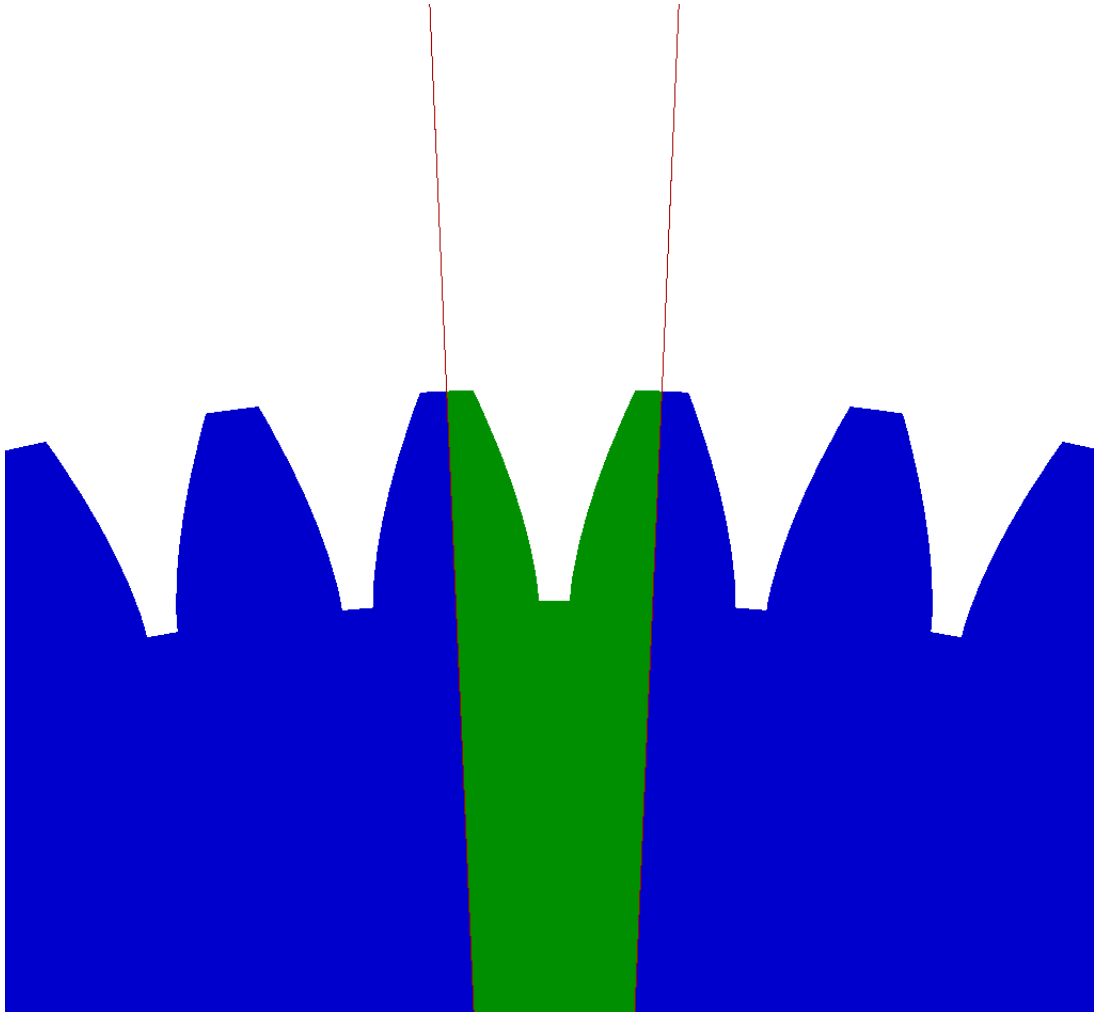
Figure 2.1. An example domain reduction of an axisymmetric system with periodic boundaries.

2.3 Overset Grid Methods

The overset grid approach [54] uses a composite grid consisting of a set of overlapping component grids to discretize the domain. No point-to-point or face-to-face matching is required between component grids. The solution on the component grids are linked by identifying appropriate intergrid boundary points (IGBPs) where the solution is given by a specified boundary value obtain by interpolation from another overlapping donor component grid. The overset domain connectivity information (DCI), which consists of the identification of the intergrid boundary points and corresponding interpolation sources, is obtained by an overset grid assembly step.

The Donor interpolation Receptor Transaction library [55] (DiRTlib) is a solver-neutral library that encapsulates the functionality required by the solver to use the overset domain connectivity information. It is independent of the solver grid storage and topology, dependent variables, etc. and can be used with any solver. The solver calls a few functions to initialize the library, load the DCI interpolation, transfer the data to appropriate processors in a parallel execution environment, and apply the interpolated data as boundary values at IGBPs. Solver functions must be provided and are called by DiRTlib to get and put data in the correct solver-dependent variable storage locations. When the solver executes in a distributed memory parallel computational environment the solver must also inform DiRTlib of the parallel decomposition enabling DiRTlib to get/put data from the appropriate parallel process.

The current overset grid assembly process is performed using the SUGGAR code [56]. SUGGAR stands for Structured, Unstructured, Generalized overset Grid AssembleR. It is a general overset grid assembly code with the capability to create the domain connectivity information at node and/or element centers for most current grid topologies including any combination of structured Cartesian and curvilinear, unstructured tetrahedral and mixed element, general polyhedral, and octree based Cartesian grids. For static grid assemblies with no motion between component grids the grid assembly is a pre-processing step. The case of solution and time dependent motion, requires the solver to communicate the new body and grid positions to the grid assembly process, wait for it to complete, and then

load the new DCI. In the case of prescribed motion, such as used in the present study, the DCI is computed a priori and saved in a file for each time step in the simulation and the solver simply loads the file appropriate for each time step. Figure 2.2 provides an example of an overset grid. The grids colored in red are boundary layer resolved grids for the teeth. The blue gridlines represent the far field domain.
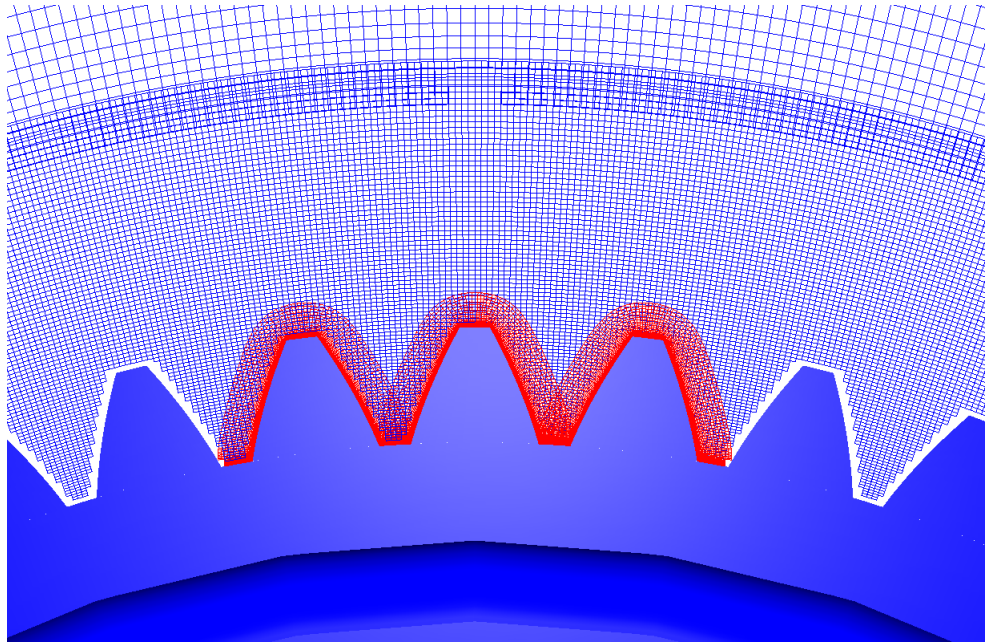
Figure 2.2. An example overset grid system.

The donor interpolations produced by SUGGAR are a set of linear weights that multiply the values at the donor members. For a cell centered flow solver the interpolation stencil will use as members the cell in the donor grid that was found to contain an IGBP and the neighboring cells that share a face with the donor cell. The interpolation weights are computed using an unweighted least square procedure.

Chapter 3

Validation and Parametric Studies

The experimental data of Diab et al. [6] has been used to validate both NPHASE-PSU and OVER-REL for the case of isolated unshrouded rotating spur gears. Diab et al. tested four different spur gears and a disk isolated in free air on a spin-down test rig. The properties of the gears were listed in Table 1.1. The effects of an enclosure or lubrication were not part of the study. Diab et al. used a spin-down test rig to measure windage losses. Here, a sequence of prescribed constant rotation rate simulations are used to replicate the experiment.

3.1 NPHASE-PSU Results

Grids were generated for all four spur gears and the disk. For the gear studies where the high Reynolds number k-ϵ turbulence model was used, near-wall grid spacing was defined to accommodate wall-functions (e.g., $y^+ \simeq 70$ for gear 1, $\omega = 1000$ rad/s). The single plane of symmetry in the problem (at the gear centerline) was exploited to reduce total cell count by a factor of two. Grid cell counts for the different cases varied between 2.0 x 10^6 (Gear 4) and 8.0 x 10^6 (Gear 1). Grid generation was further simplified by employing a hybrid mesh topology, as illustrated in Figure 3.1. Specifically, for the regions above the surface of the gear teeth to the outer radial boundary, structured hexahedral cells were used. For the region above the gear face surface, unstructured prism cells were employed. Figure 3.1 shows the surface mesh of the gear in blue and the symmetry plane in purple. The meshes were generated using the commercial grid generation software

package GridgenV15.15 [57]. The computational domain of the isolated gear grids was extended to approximately five times the gear radius from the gear surface in all directions. It was found that this distance was adequate for defining a farfield boundary condition with a specified pressure since the flow is nearly stagnant there.
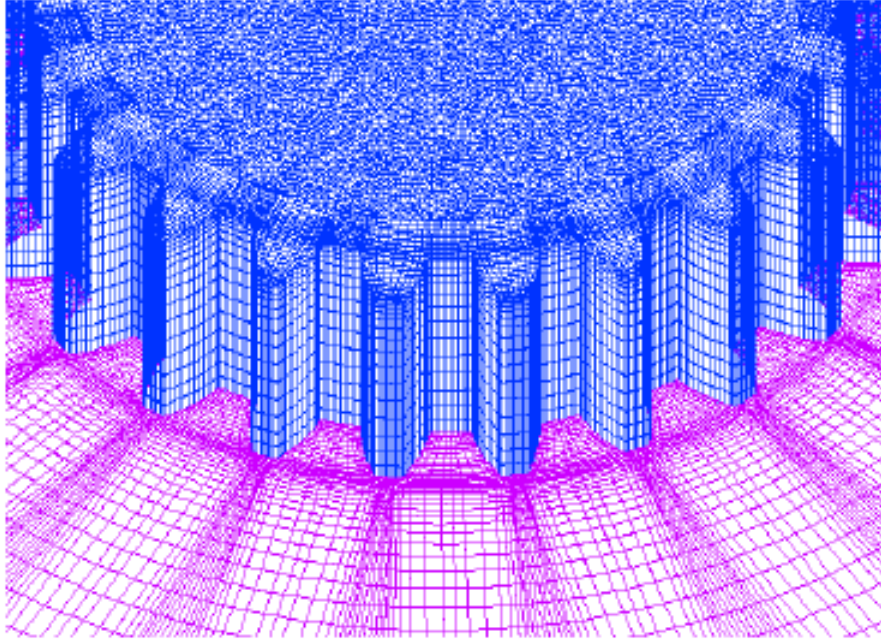
Figure 3.1. Grid topology of Diab Gear 4.

An azimuthal step size of 1/40th of one tooth passage duration (the time it takes one tooth to rotate to the position of the tooth adjacent to it) was used in all CFD calculations. The timestep size Δt can be calculated by using Equation 3.1:

$$\Delta t = \frac{1}{40}\left(\frac{2\pi}{N\omega}\right) \tag{3.1}$$

where N is the number of gear teeth and ω is angular velocity in radians per second. This corresponds to 2880 timesteps per gear revolution for Gear 1, 1440 timesteps for Gears 2 & 3, and 960 timesteps for Gear 4. All cases used 10 pseudo-time iterations per physical timestep. All of the Diab gear NPHASE-PSU simulations presented here were executed on the Columbia supercomputer at NASA Ames Research Center. The code scales very well on this system as illustrated in Figure 3.2.

Figure 3.2 shows that by increasing the number of processors used to compute the solution for a 1.1 x 10^6 cell rotating disk case, NPHASE-PSU exhibits better than ideal (linear) speedup in processing time when running on Columbia.
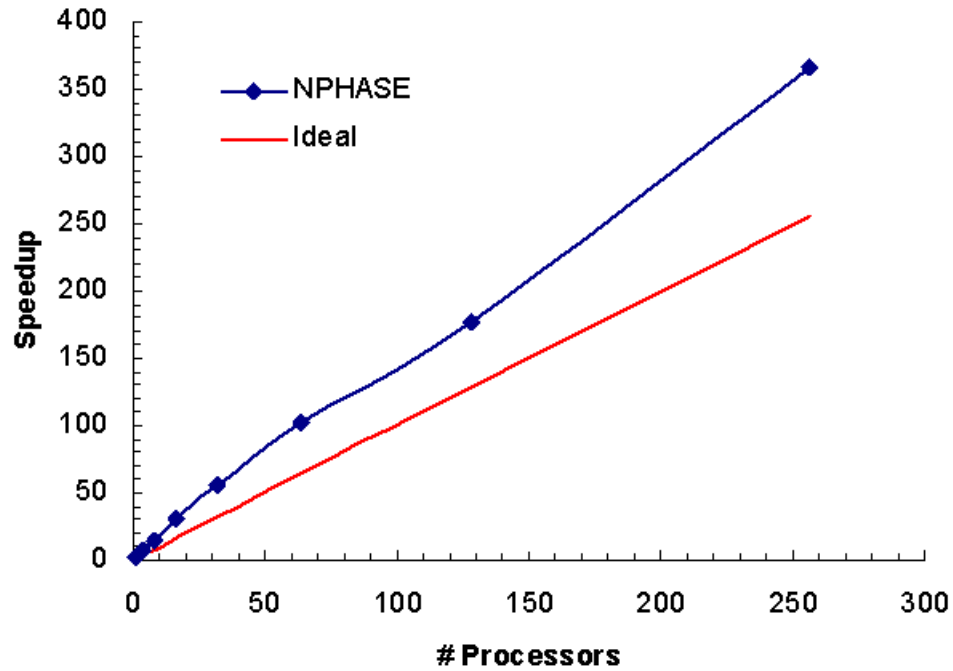
Figure 3.2. Parallel efficiency of NPHASE-PSU on the NASA Ames Columbia computer system for a spinning disk case (1.1x10^6 cells).

CFD runs were made for all four gears and the disk at a number of rotation speeds. All cases were run for at least two complete revolutions to remove simulation startup transient behavior. Convergence histories show that transients leave the solution after about one revolution as illustrated in Figure 3.3, where it is also observed that the pseudo-time residual drops approximately two orders of magnitude in each physical timestep when 10 pseudo-timesteps are used per physical timestep.

Figure 3.4 compares the experimental results of Diab et al. [6] with the computational NPHASE-PSU analysis of all four gears. The CFD analysis for all of the gears exhibited very good agreement with experiment. The disk case, however, did not share this same level of agreement, as illustrated in Figure 3.5, where NPHASE-PSU results are seen to underpredict the measured power loss. In order
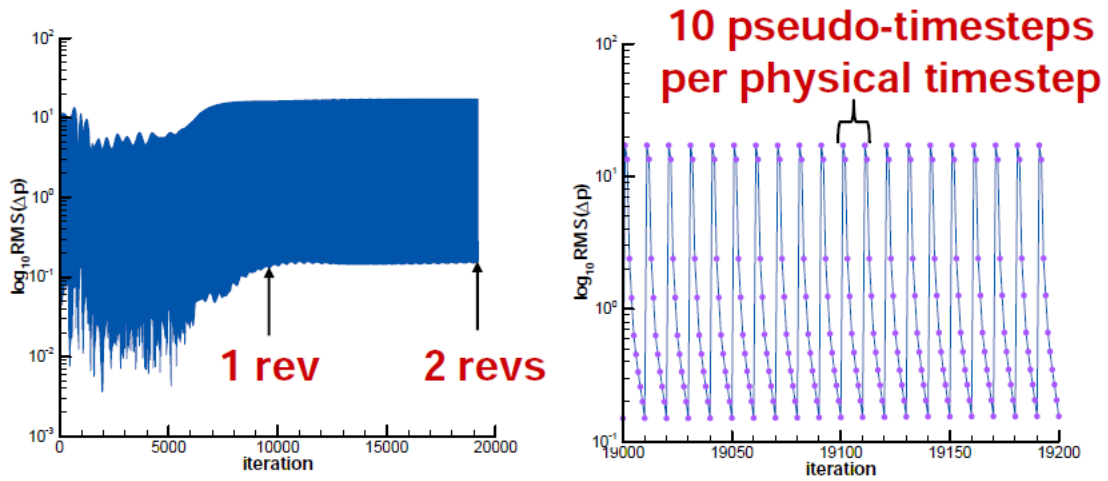
Figure 3.3. Example NPHASE-PSU convergence history.

to elucidate the reasons for the deterioration in solution accuracy observed for the disk case, a number of observations and studies were made. First, it is observed that the measured (and computed) windage loss power levels for the disk are much smaller than the comparably sized spur gear (Gear 1, D $\simeq$ 300 mm). This arises due to the absence of any azimuthal pressure variation in the disc flow - torque losses are due entirely to viscous effects, and these are clearly underpredicted. Indeed the absolute magnitudes of loss underprediction between the disk and Gear 1 are comparable (e.g. $\simeq$ 50W @ $600s^{-1}$), so presumably this underprediction of shear is present in all of the gear simulations, however its relative magnitude is small for Gear 1.

To explore this further, the low-Reynolds number Menter $k-\epsilon/k-\omega$ model [46] was applied to the spinning disk case (using an appropriate sub-layer resolved mesh). Figure 3.5 illustrates that improved turbulence modeling does benefit solution accuracy especially at higher rotation rates. This observation is not as important for the gear cases since the windage torques associated with azimuthally varying pressure forces in the vicinity of the gear teeth dominate the viscous forces as shown in Figures 3.6 and 3.7. It can be seen that, especially at lower rotation rates, the contribution of viscous loss to total windage loss, is quite small. However, it is observed that at higher pitch-line velocities the relative magnitude of the viscous torque increases with respect to the pressure torque. This can be seen with Gear 1 (Figure 3.6) as well as with the smaller of Gear 2 (Figure 3.7). At a
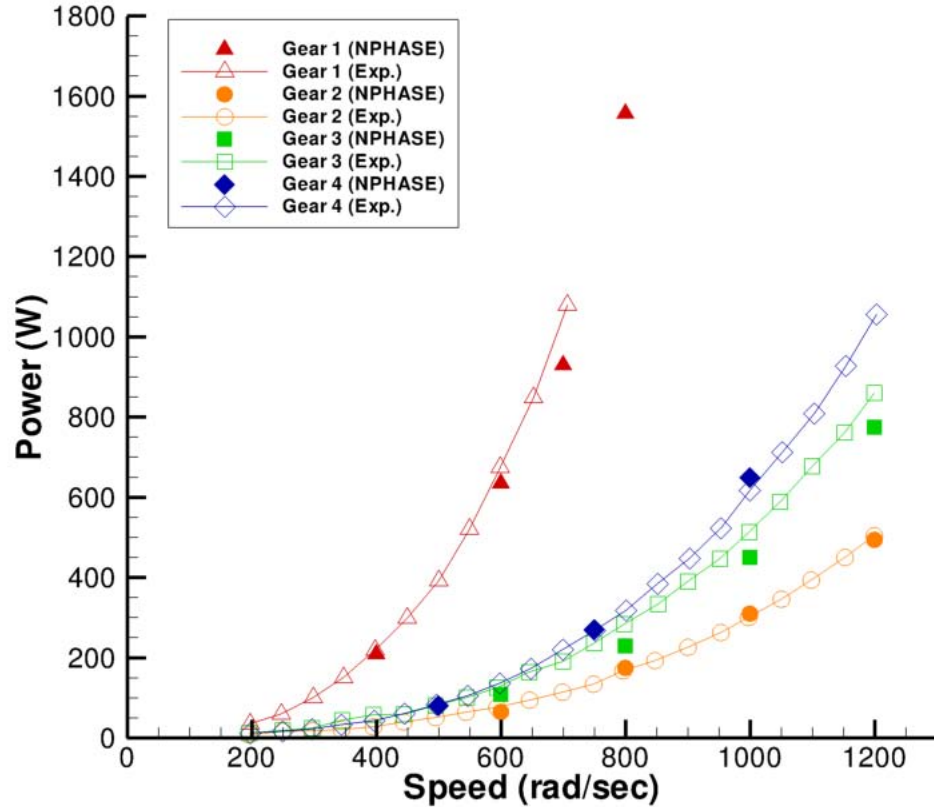
Figure 3.4. Comparison between Diab experimental results and NPHASE-PSU analysis.

rotation rate of 800 rad/s, Gear 1 has a pitchline velocity of 172.6 m/s. Gear 2 reaches a maximum pitch-line velocity of 86.4 m/s at 1200 rad/s.

A number of important physical features of the predicted flow field are available upon interrogation of the CFD simulations. Figure 3.8 shows a view of the predicted secondary velocity vectors on the symmetry plane in the gear relative frame of reference for one of the Diab cases. One can see a significant vortical structure within the gear tooth region, and the tooth-to-tooth periodicity that has been achieved in the transient simulation. Similar flow structures were seen by Al-shibli et al. [30] and Marchesse et al. [34] in their CFD studies of gear windage. Figure 3.9 displays the predicted surface pressure distributions for the four Diab
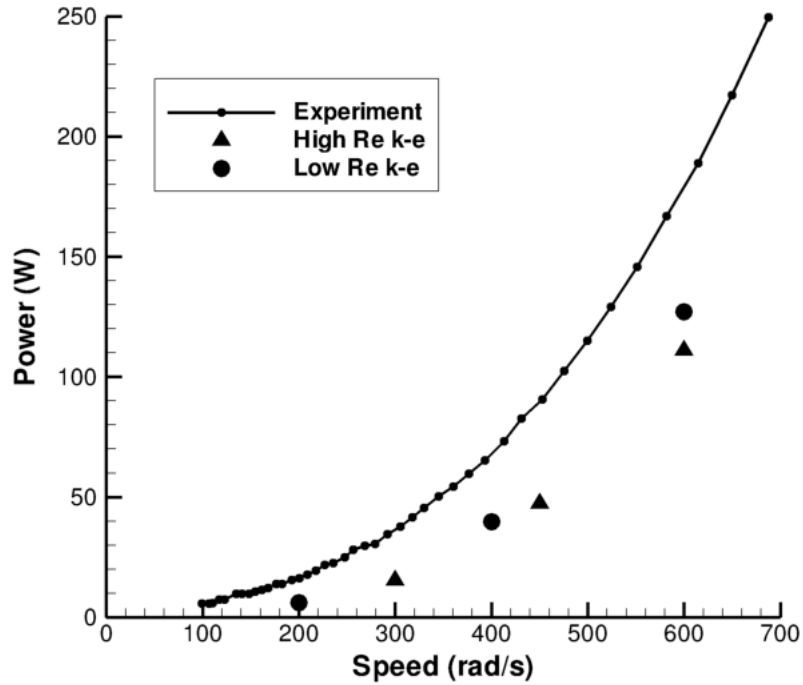
Figure 3.5. Effect of turbulence model selection on viscous work prediction.

gears. Comparatively large pressure differences are observed between the leading and trailing tooth faces - this difference being the source of the pressure component of the spin-down torque. The highly three-dimensional nature of the flow in these spurs gears is also clearly seen (the figure shows only 1/2 of each gear).

In summary the results suggest that for the very high speed gears encountered in rotorcraft (and other high performance aircraft) transmissions, viscous effects will become more important. Secondly, it appears that the windage pressure torques are predominantly located at the edges of the teeth of a spur gear.
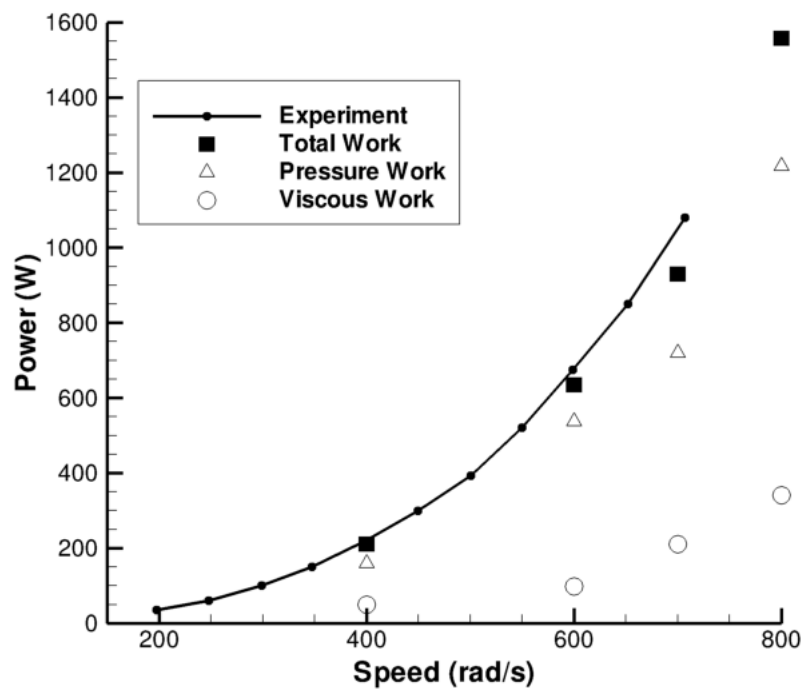
Figure 3.6. Breakdown of windage power losses for Diab Gear 1.
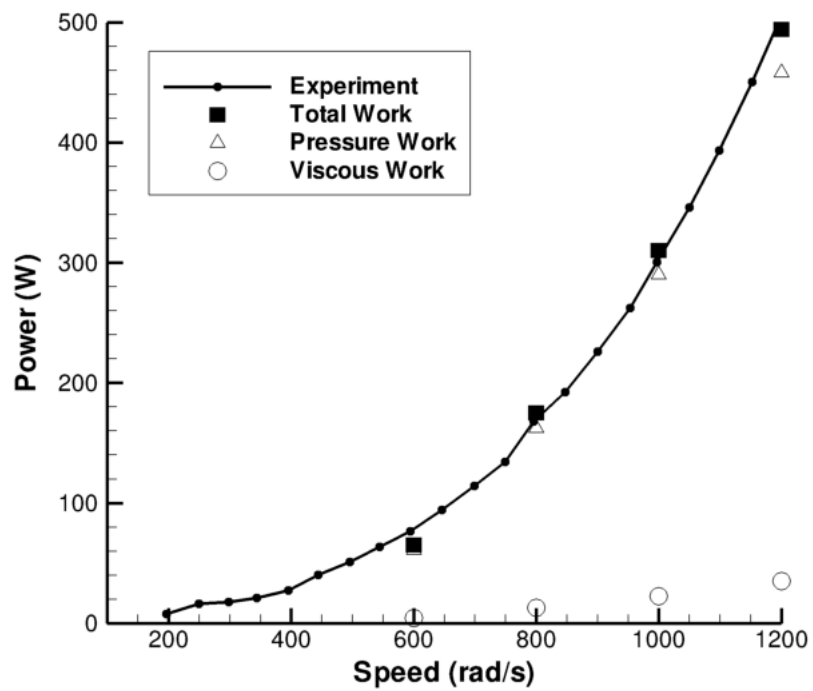
Figure 3.7. Breakdown of windage power losses for Diab Gear 2.
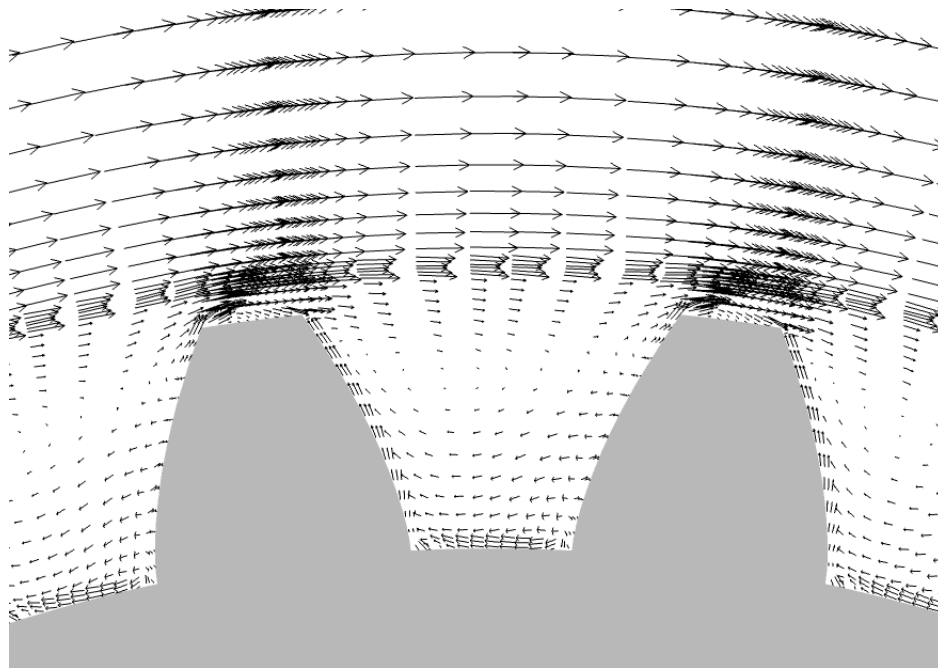
Figure 3.8. Secondary flows within the gear teeth.
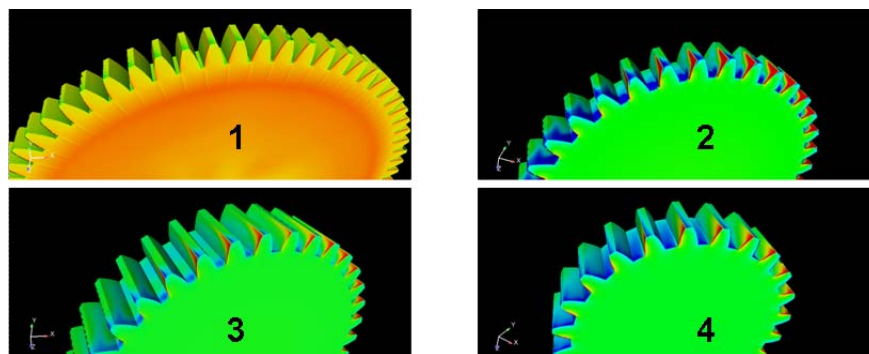
Figure 3.9. Predicted surface pressure distribution for Diab Gears 1-4. Only one side of symmetry plane is shown for each gear. The areas shaded in red indicate high pressure areas.

3.2 OVER-REL RESULTS

In the previous section, NPHASE-PSU was used to study all four gears and the disk of Diab et al. [6]. The NPHASE-PSU simulations exhibited very good agreement with experiment in modeling windage losses for all of the gear configurations. It was also shown that a sub-layer resolved two-equation turbulence model performed better than a high-Reynolds number form with wall functions in predicting viscous losses on a disk. Unfortunately, using sub-layer resolved meshes to describe the geometry of an entire gear and capture the unsteady flow physics is quite computationally expensive. The size of the grids easily exceeded 20 million cells. Although this is not an impossible calculation with modern supercomputers (e.g. Columbia at NASA Ames Research Center), it still requires significant CPU resources and computation time.

Therefore, it was decided to change the overall grid topology to a single "blade-row"/gear tooth and exploit the axial symmetry of gear geometry instead of the planar. This topology is better suited to the present physics exploration analyses due to its efficiency. With this type of topology, the CPU resources that could been used to run one sub-layer resolved NPHASE-PSU case, could be used to run at least ten OVER-REL simulations. The solver OVER-REL is mature and validated for these types of calculations so it was selected. In the present application, the OVER-REL's turbomachinery analysis instrumentation is employed. All simulations are carried out for a single gear tooth with periodic boundary conditions in a non-inertial frame-of-reference rotating with the gear.

First, free spinning simulations were carried out for Diab Gear 1 and disk using OVER-REL. Non-overset multiblock structured meshes were employed for both as shown in Figures 3.10 and 3.11. In Figure 3.11, one of the periodic boundaries is highlighted by the dark blue mesh. The light blue lines represent the edges of the various grid blocks that make up the domain, and the green and purple surface represents the surface of the gear. Not shown in the figure is the outer axial and radial boundaries, which were set as inviscid walls. Near-wall grids were constructed to return wall cell y^+ values < 1 and wall normal stretching ratios < 1.2 everywhere in order to adequately resolve the high Reynolds number boundary layers that arise. The grid topologies, near-wall grid spacing, and grid stretching

ratios were maintained as closely as possible between the gear and disk meshes. In accordance with the periodic boundary conditions employed, one tooth passage $(2\pi/72)$ is modeled for both configurations. For a single tooth passage, the total grid cell count did not exceed 1.6 x 10^6 cells. In order to stably time-march the OVER-REL solution, a very small inflow velocity and a pressure outflow boundary were included adjacent to the maximum and minimum axial boundaries upstream and downstream of the rotating elements. This artificial through-flow velocity was successfully reduced to where no perceptible changes in loss values were returned. Figure 3.12 is an example convergence history of the axial torque component.
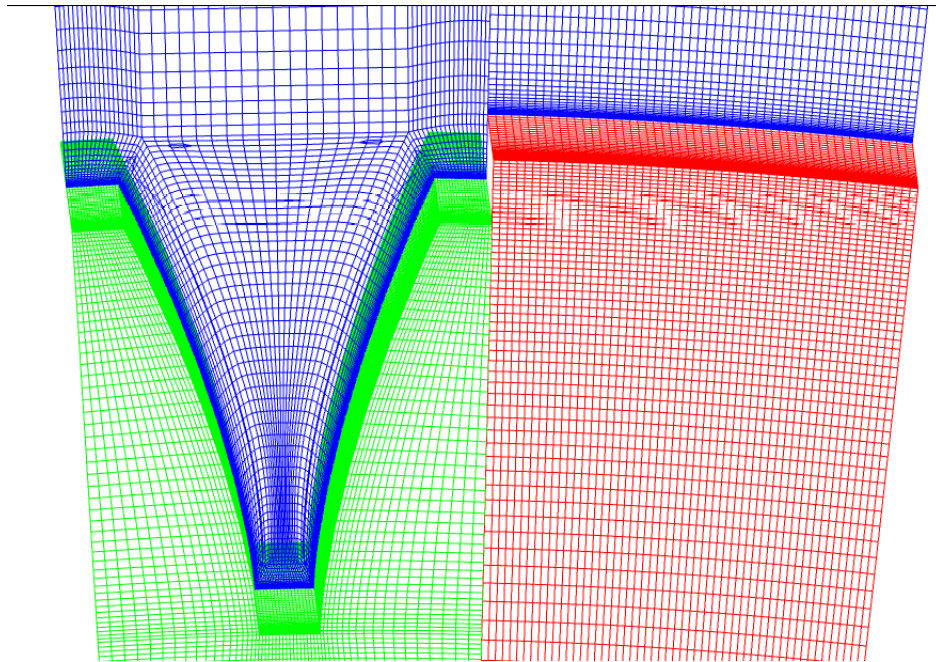
Figure 3.10. Comparison of Diab Gear 1 and disk grids.

Figure 3.13 includes the OVER-REL results for Gear 1 along with the previous results from NPHASE-PSU. Very good agreement with experiment is seen here as well. Figure 3.14 shows that for Gear 1, the pressure torque associated with the integrated pressure difference between leading and trailing tooth surfaces, dominates the loss budget. As the rotation rate increases, viscous losses remain a nearly constant fraction of total loss (10%). Figure 3.15 shows a comparison of loss results between Gear 1 and the disk. The total losses are much smaller for the disk, which are due to viscous shear alone. This large difference between the disk and Gear 1
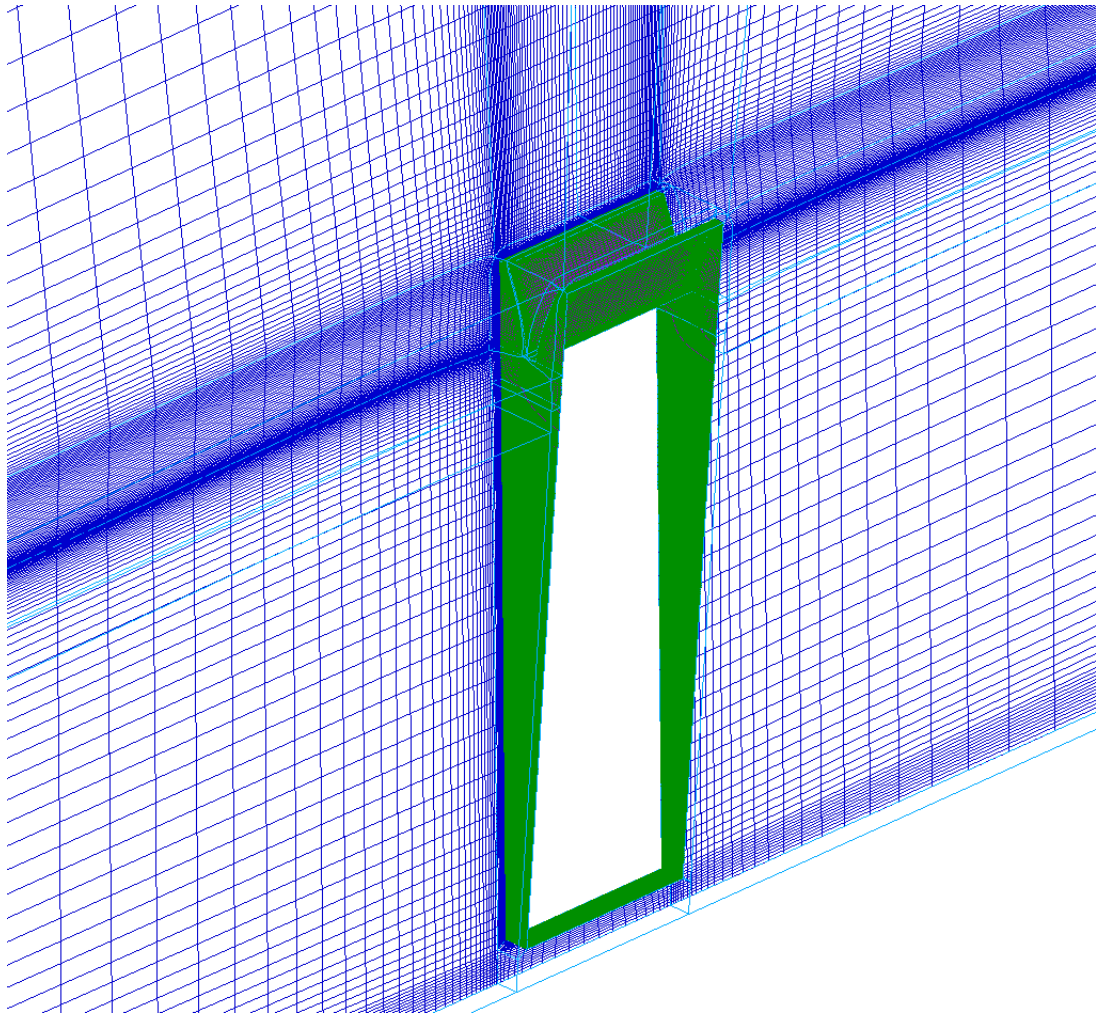
Figure 3.11. OVER-REL grid topology for Diab Gear 1. Periodic boundary is highlighted in blue. Gear surface mesh is highlighted in green.

is particularly striking if we compare their similar sizes as shown in Figure 3.10.

In Figure 3.16, the torque per unit span of radius contributed by viscous shear is compared for the disk (up to its outer radius) and Gear 1 (up to its base radius). The geometry of these systems requires that all of the pressure torque is due to the pressure differences between the leading and trailing tooth surfaces. Figure 3.16 illustrates that the viscous losses are very similar between these configurations (indeed the small differences in predicted viscous power values are due to very small grid differences) indicating that 3-D effects (i.e. non-axisymmetric) associated with pressure forces are almost completely responsible for the significant increase in loss
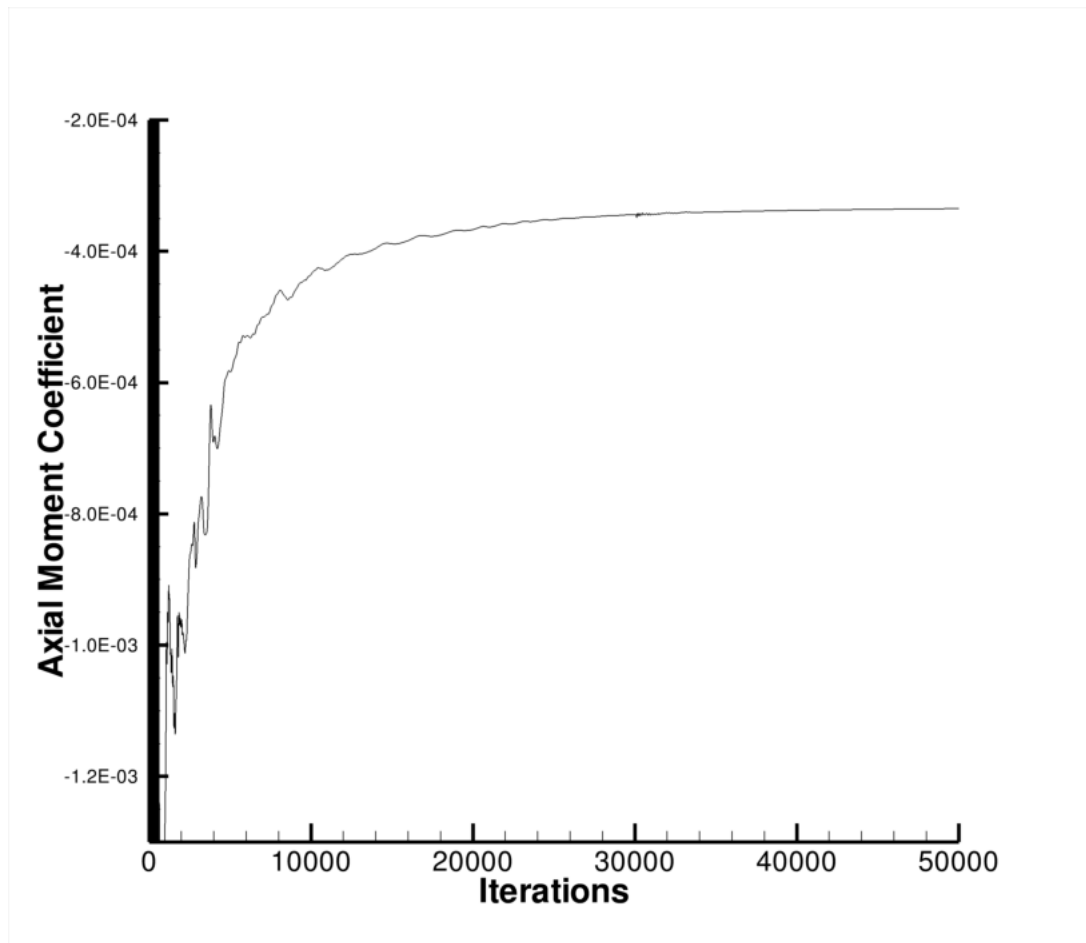
Figure 3.12. Example OVER-REL convergence history of the axial torque component.

for the gear. Appendix B provides the C++ source code used to generate these profiles.
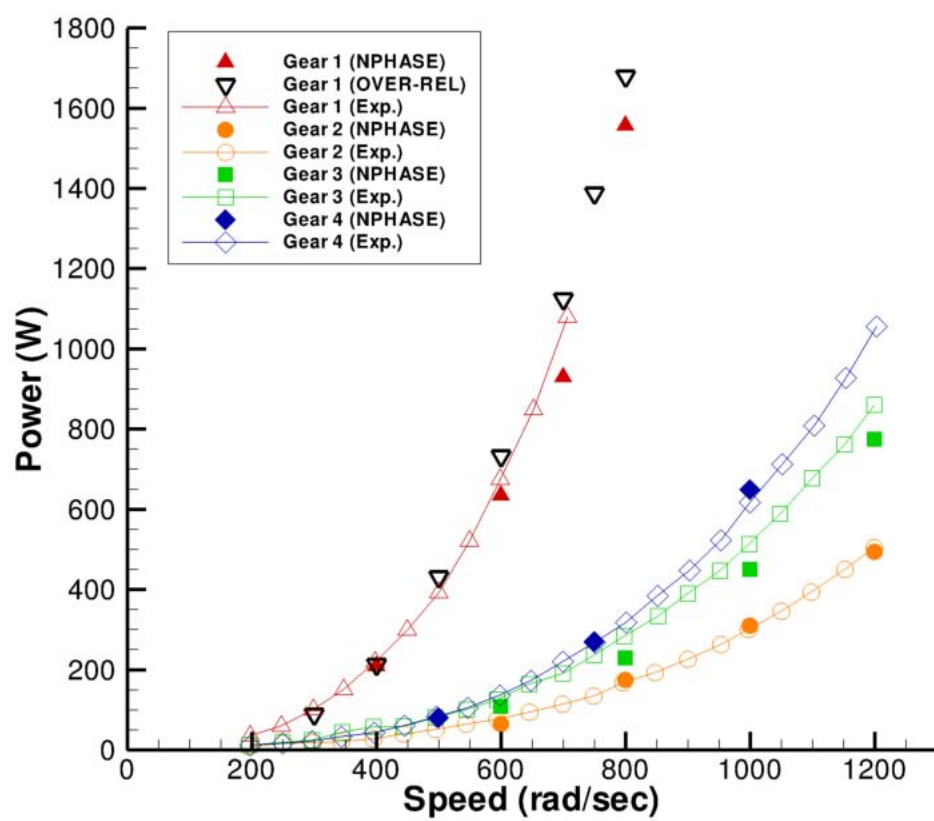
Figure 3.13. Experimental, NPHASE-PSU, and OVER-REL results for Diab Gears 1-4.
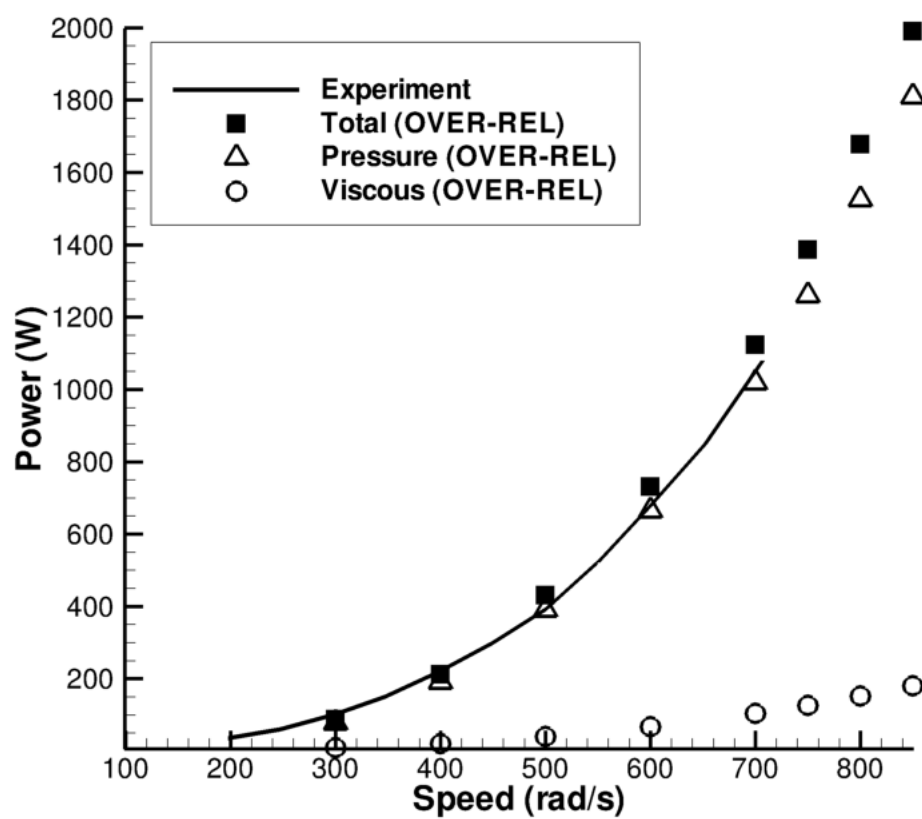
Figure 3.14. Comparison of results from experiment and OVER-REL for Diab Gear 1, including viscous and pressure loss budgets.
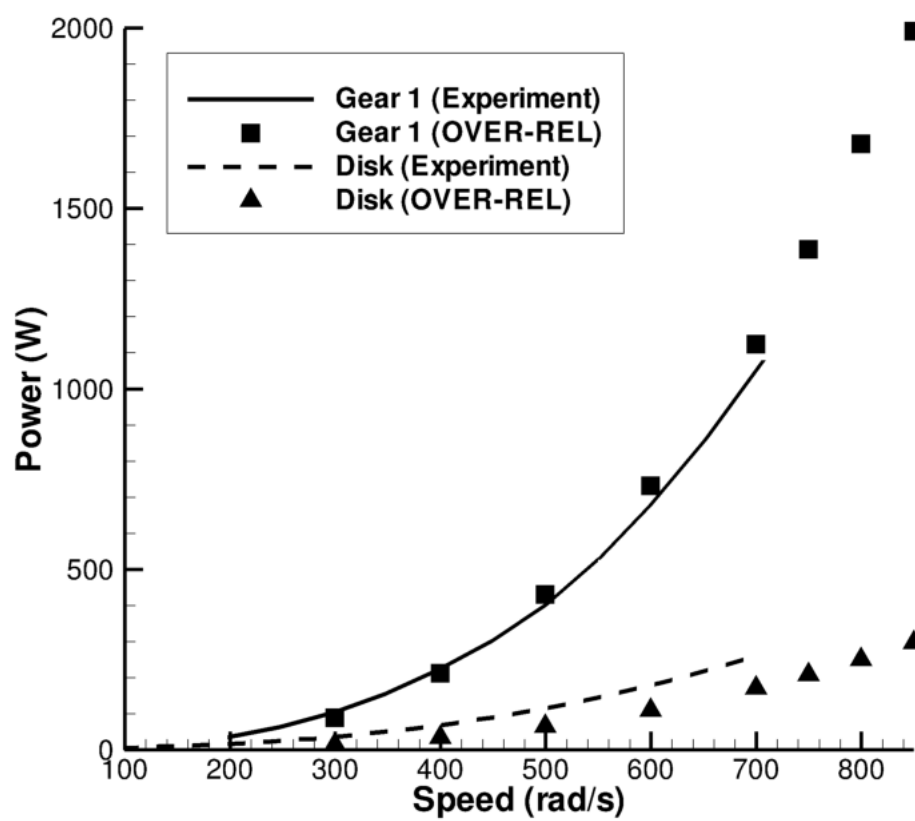
Figure 3.15. Comparison of Diab Gear 1 and disk measurements and OVER-REL solutions.
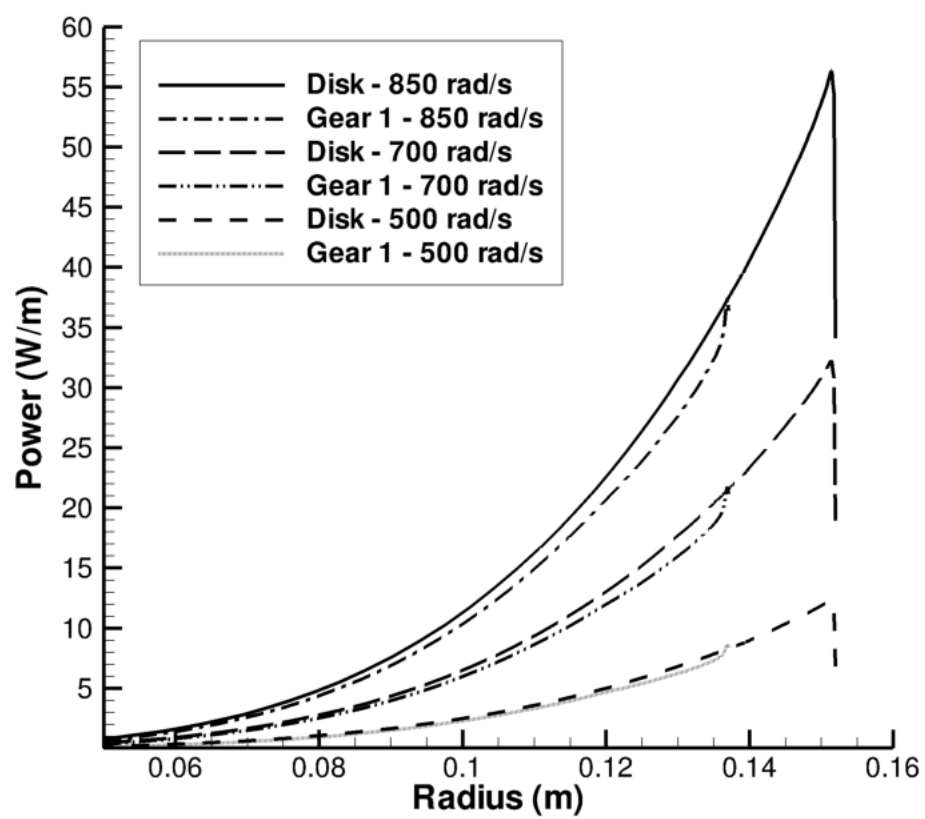
Figure 3.16. Comparison of predicted torque per unit span contributed by viscous shear for the Diab disk (up to its outer radius) and Gear 1 (up to its base radius).

3.3 Details of the 3-D Flow Field

The physical mechanisms associated with the dominant pressure torque are studied by interrogating the CFD results for Diab Gear 1 with OVER-REL. In Figures 3.17 - 3.19, several 3-D visualizations are presented for the 850 rad/s case. In Figure 3.17, a number of relative frame-of-reference streamlines, colored by local static pressure, are plotted. These streamlines are seeded close to the gear face and teeth and integrated in both directions. Some of the high speed (in the relative frame) tangential flow near the gear face plane is diverted into the tooth passage, where strong secondary flows are evident. Due to symmetry this axial transport arises on both sides of the gear and therefore leads to impingement of oppositely directed flows and radial ejection of momentum at the gear centerline. Figure 3.17 also shows an axial view of the same streamlines illustrating the complex secondary motions and an indication of the radial ejection angle. Also evident is the radially outward component of flow close to the face below the teeth. An axial projection of relative velocity vectors is shown in Figure 3.18 at a plane halfway between the gear face and gear centerline. A vector density of 0.5 (vector plotted for approximately every other grid point) is applied for clarity. Contours of local normalized projected relative velocity magnitude are included ($V^* = \sqrt{V_y^2 + V_z^2}/\omega r$). Two counter-rotating passage vortices are present. Peak normalized secondary velocity magnitudes near $\frac{1}{2}\omega r$ are observed indicating the strength of these secondary motions. The flow at this axial location is reminiscent of a rearward facing step and/or cavity flow with attendant vortical recirculation regions. Figure 3.19 shows the same plot but at the gear centerline. Here one sees the very significant radial ejection quite clearly. The flow has a component directed upstream (against the relative flow) near the leading surface at the tip radius. The magnitude of the ejection flow induces significant blockage and we see values of V^* much less than 1 well beyond the tip radius.

In Figure 3.20, contours of static pressure coefficient, ($C_P = (p - p_\infty)/0.5\rho V_{tip}^2$) are plotted for the leading gear tooth surface. As can be seen in the figure, some of the high speed tangential flow near the gear face plane is diverted into the tooth passage. There is a stagnation region where this flow impinges on the leading surface, near the gear face. The leading surface pressure field can be compared
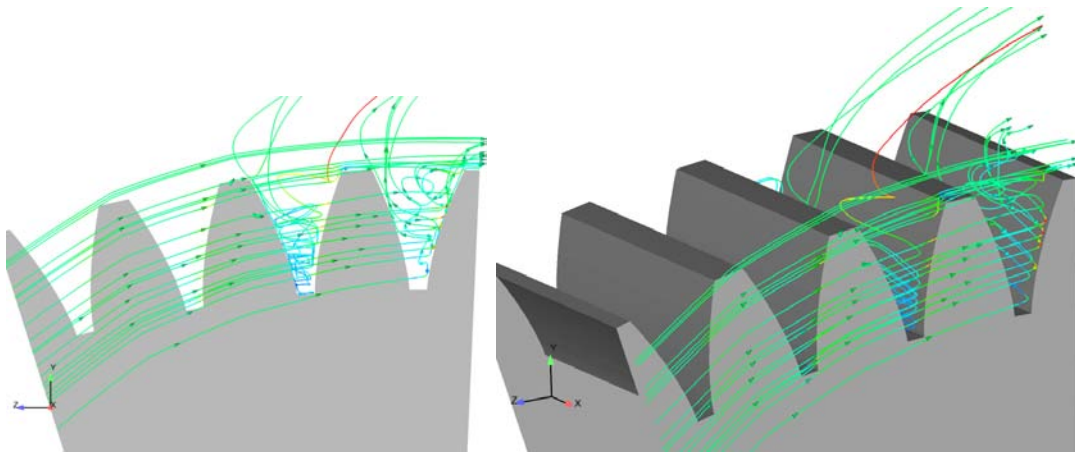
Figure 3.17. Three-dimensional relative frame streamlines colored by static pressure for Diab Gear 1 at 850 rad/s.
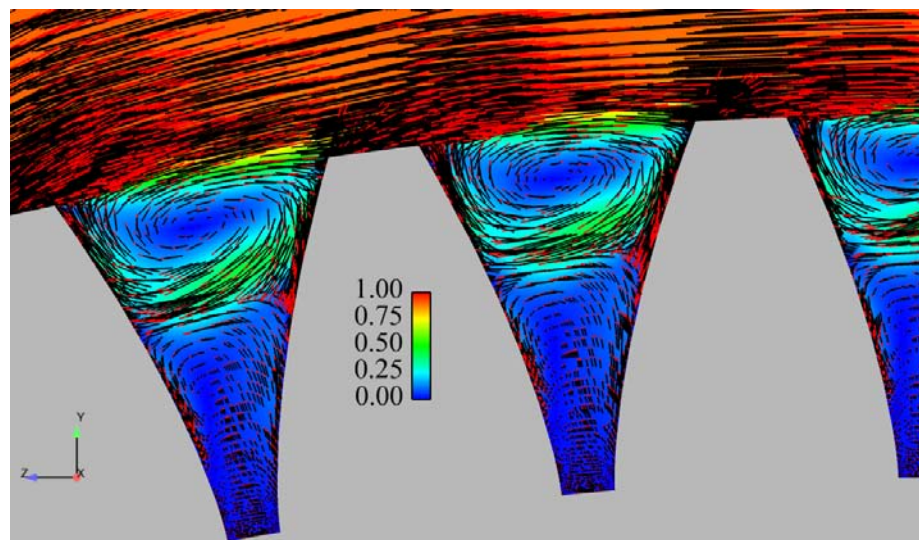
Figure 3.18. Axial projection of velocity vectors halfway between gear face and gear centerline of Diab Gear 1 at 850 rad/s. Vector density of 0.5. Background contours of local normalized projected relative velocity magnitude.

with the much lower surface pressures on the trailing surface. The net axial torque due to pressure effects can be represented by the difference between the leading and trailing surface pressure coefficients, which is shown in Figure 3.21. Clearly the net torque is dominated by the impingement observed in Figures 3.17 and 3.20. In Figure 3.22 the torque per unit width is plotted vs. distance from the gear face.
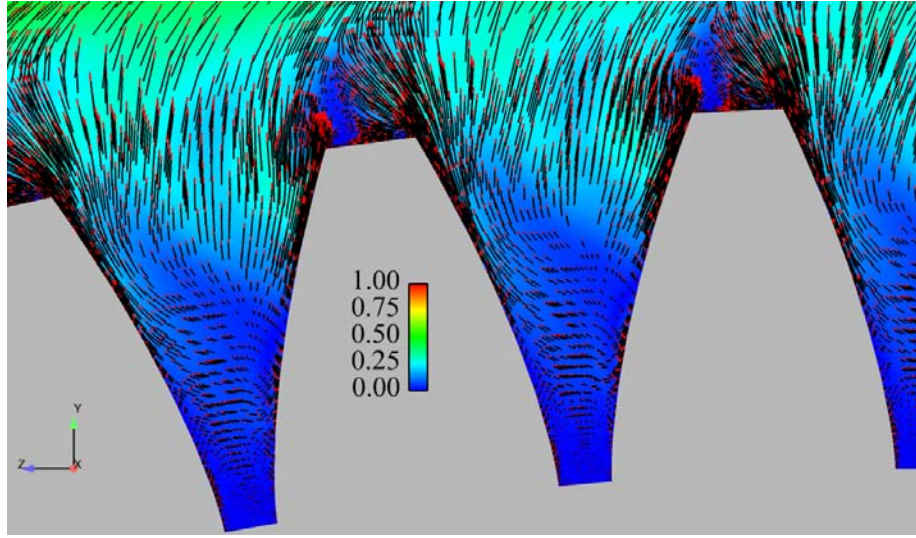
Figure 3.19. Axial projection of velocity vectors near gear centerline of Diab Gear 1 at 850 rad/s. Vector density of 0.5. Background contours of local normalized projected relative velocity magnitude.

Here, torque is nondimensionalized as:

$$T^*(x) = \frac{\int_{r_{inner}}^{r_{tip}} \Delta p \, dA_\theta \, dr}{dx} \left[\frac{1}{\frac{1}{2}\rho V_{ref}^2 L_{ref}^2} \right] \tag{3.2}$$

where Δp is the pressure difference between the grid faces on the leading and trailing surfaces (which have identical x-r vertex coordinates), dA_θ is the tangential projection of the area of the grid face, and r is the radial coordinate of the grid face centroid, and the reference length, L_{ref}, is the gear tip radius. We see that indeed it is the near face region that dominates the pressure windage loss torque.
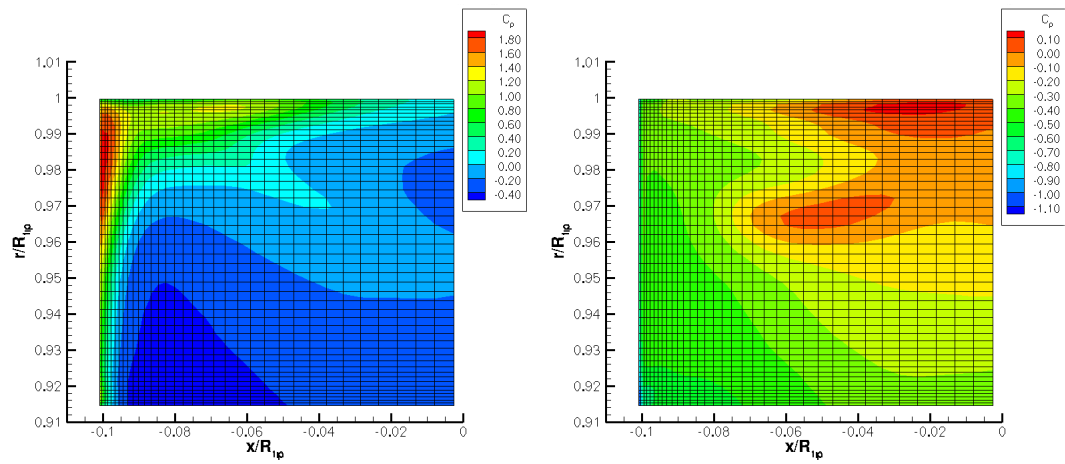
Figure 3.20. Static pressure coefficient contours on the gear leading tooth surface(left) and trailing tooth surface(right) of Diab Gear 1 at 850 rad/s. 1/2 of symmetrical gear shown.
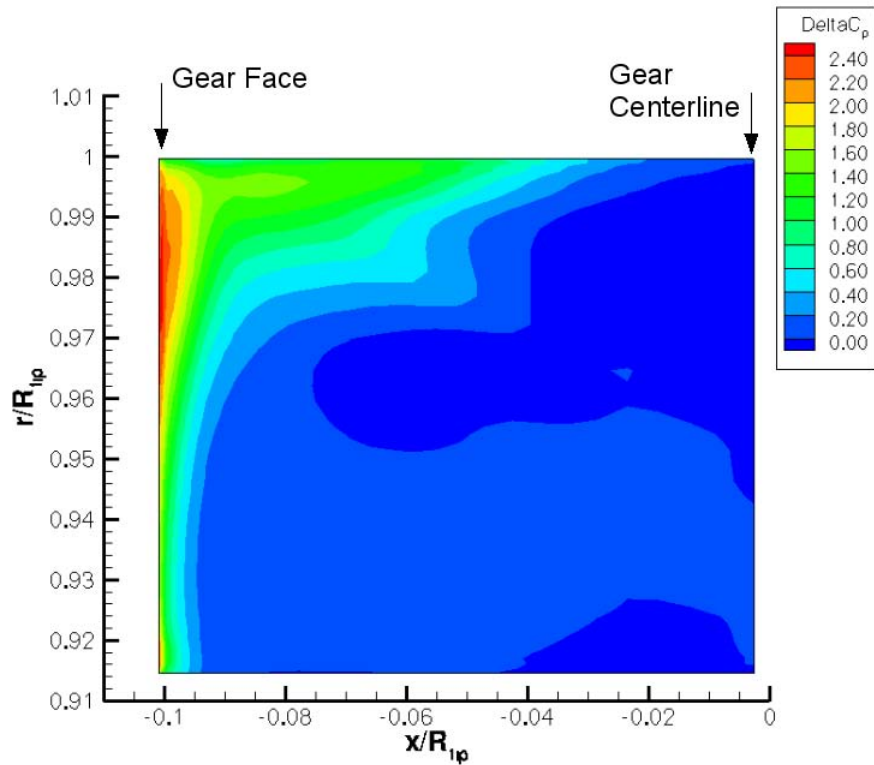
Figure 3.21. ΔC_P between gear leading and trailing tooth surfaces of Diab Gear 1 at 850 rad/s. 1/2 of symmetrical gear shown.
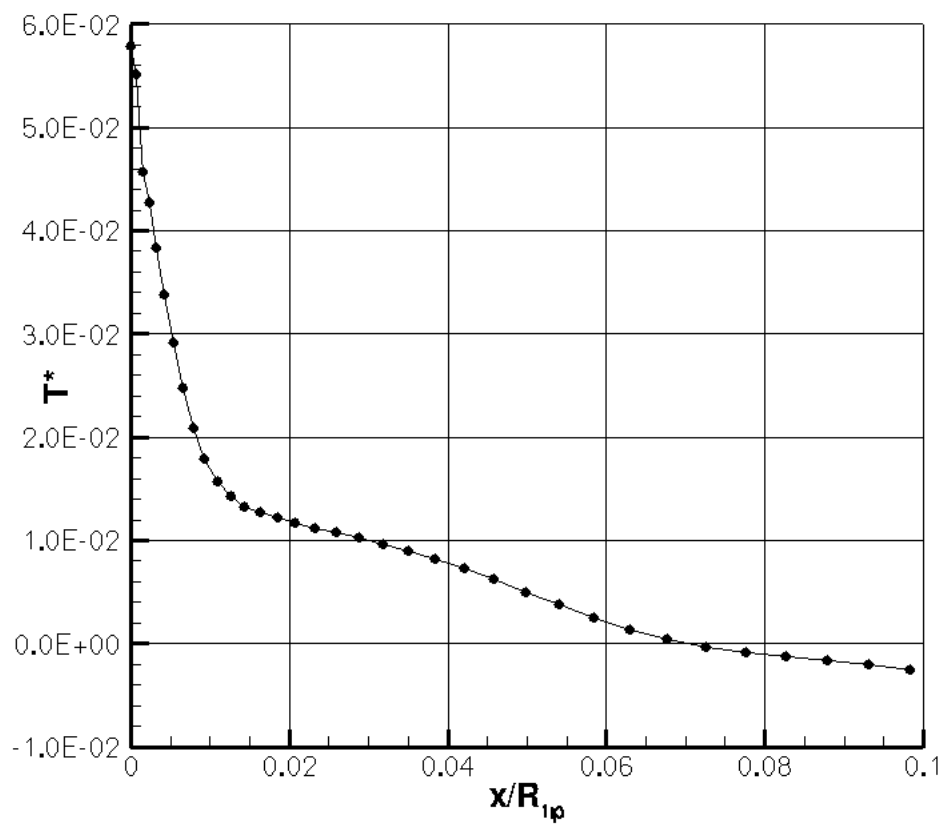
Figure 3.22. Pressure torque per unit width vs. axial coordinate of Diab Gear 1 at 850 rad/s. 1/2 of symmetrical gear shown.

Chapter 4

Aerodynamic Studies of Windage Loss Mitigation Strategies

4.1 Shrouded Diab Gears

As mentioned previously (Section 1.2), several researchers have measured improvements in gear windage loss performance when shrouds of various configurations are employed [8, 10, 4, 38]. In this section the aerodynamics of shrouding are explored in the context of geometrically simple configurations and several conclusions are drawn that may impact design decisions. The Diab Gear 1 configuration studied in Section 3.2 is employed. Four notional shrouding arrangements are examined, nominally: Large-Axial-Large-Radial, Small-Axial-Large-Radial, Large-Axial-Small-Radial, and Small-Axial-Small-Radial. The shroud dimensions are quantified and illustrated in Table 4.1 and Figure 4.1, respectively. These four shroud configurations were chosen to be representative of the extrema of the full-shroud NASA Glenn tests detailed in Section 4.3.

Table 4.1. Diab Shroud Clearances

	Minimum	Maximum
Axial, $(/R_{tip})$	0.0044	0.1733
Radial, $(/R_{tip})$	0.0044	0.0970
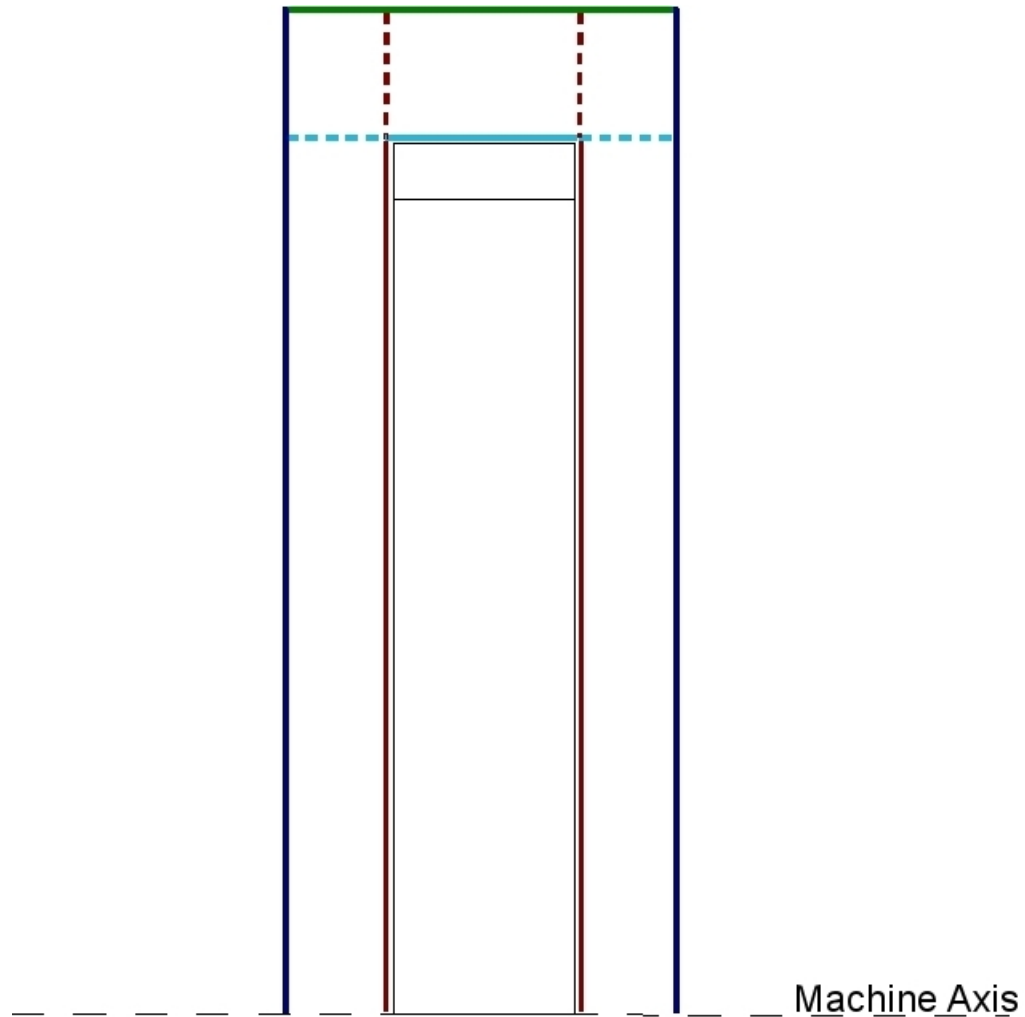
Figure 4.1. Four notional shroud configurations for Diab Gear 1 geometry. Figure is to scale. Black lines define the gear face, tip radius and base radius, dark blue and red lines indicate the Large-Axial and Small-Axial shrouds, green and cyan lines indicate the Large-Radial and Small-Radial shrouds.

Figure 4.2 provides a cross-sectional view of the overall grid topology used in the Large-Axial-Large-Radial configuration. In order to stably time-march the OVER-REL solution and flush out start-up solution transients, a very small inflow velocity and a pressure outflow boundary were included adjacent to the maximum and minimum axial boundaries upstream and downstream of the rotating elements. This artificial through-flow velocity was successively reduced to where no percepible changes in loss values were returned. The smaller axial and radial shroud

clearances gave rise to mesh topology constraints that lead to poor quality block-structured meshes. Therefore, overset meshes were used for these cases. Figure 4.3 is a cross-sectional view of the overset mesh topology for a Small-Radial case. The blue mesh is the boundary layer resolved grid of the shroud; the red mesh is the boundary layer resolved grid of the gear.
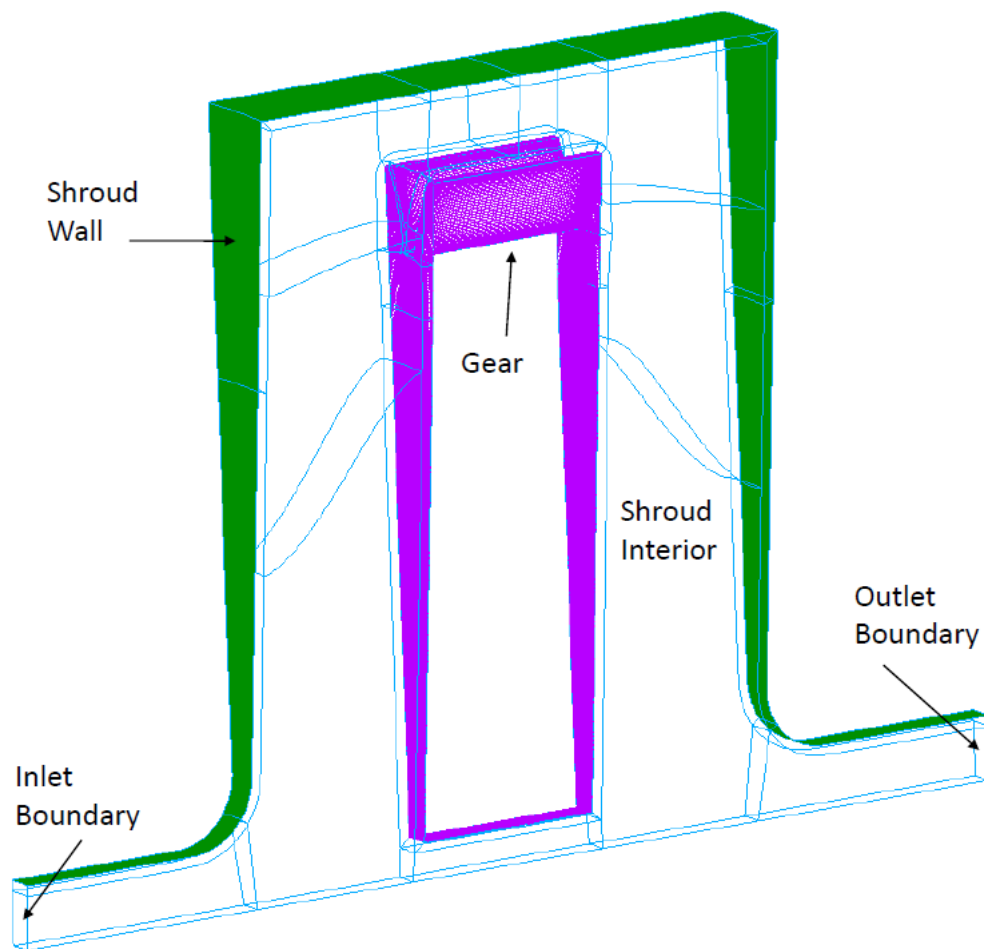
Figure 4.2. Grid topology of the Large-Axial-Large-Radial shroud configuration.

In Figure 4.4, predicted windage loss vs. rotation rate is plotted for the un-shrouded case, validated and studied previously (Section 3.2), and the four shroud configurations. Each of the shrouds give rise to very significant improvements in windage losses. The Large-Axial-Large-Radial shroud provides a 68% decrease in loss at 850 rad/s; the Small-Axial-Small-Radial shroud provides approximately a 81% decrease at the same speed. Indeed, distinguishing the performance gains
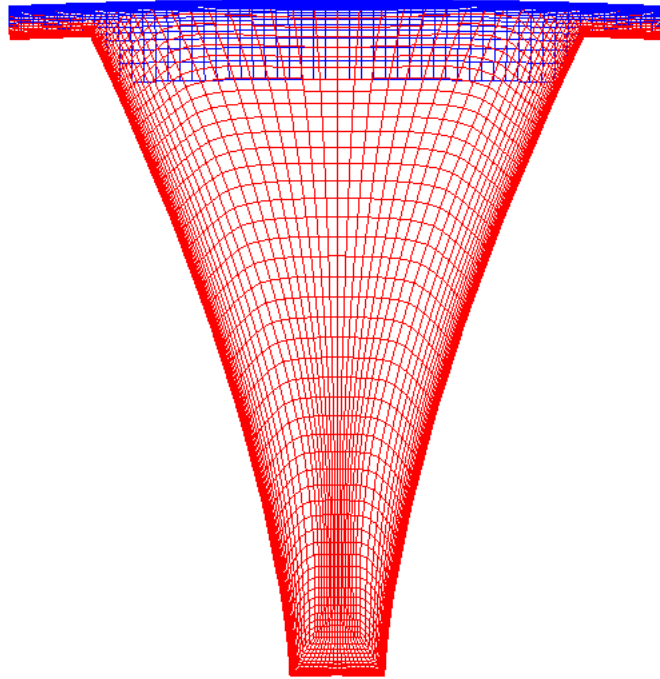
Figure 4.3. Cross-section of overset mesh topology of the Small-Radial shroud.

between the shrouded cases is helped by not including the unshrouded results as in Figure 4.5. Examining this plot we see that reducing the axial and radial clearances from large to small provide approximately the same level of additional benefit over the Large-Axial-Large-Radial case, with the reduction of the radial clearance providing somewhat more benefit in this particular case. Applying both clearance reductions together provides the maximum benefit.

Figures 4.6 and 4.7 show the same pressure coefficient plots reported previously (Figures 3.20 - 3.21), but here for the Large-Axial-Large-Radial shroud case at 850 rad/s. The load distribution on the leading surface shown in Figure 4.6 is qualitatively similar to the unshrouded case (Figure 3.20), including the stagnation region associated with near-face flow diverted into the tooth passage. However, the range of C_P values here are much smaller than for the unshrouded case. (Note that the absolute values of C_P should not be compared between cases here as this level is determined in the incompressible flow solver using a domain "exit" value of $p_\infty = 0$). The trailing surface (at right in Figure 4.6) exhibits a much more axially
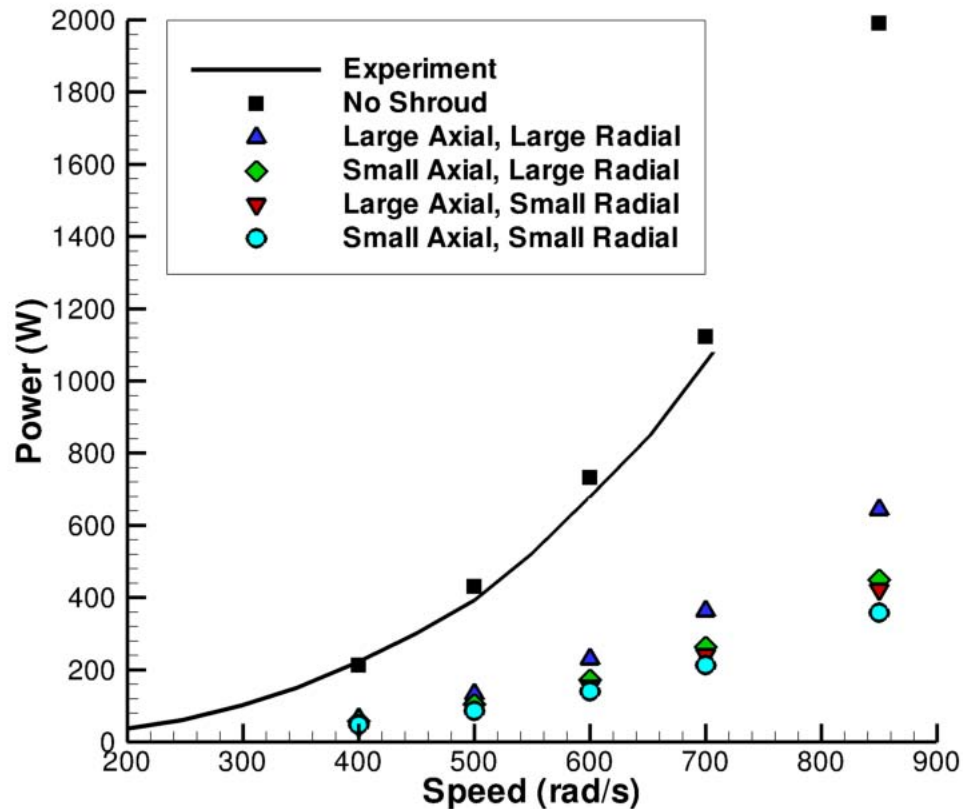
Figure 4.4. Comparison of predicted windage losses between the unshrouded and the four shrouded Diab Gear 1 configurations.

uniform pressure distribution than the unshrouded case (Figure 3.20), and again the range of C_P values here are much smaller. Most importantly, in Figure 4.7 a highly edge loaded ΔC_P between leading and trailing surfaces can be seen, as observed for the unshrouded case, but with a very reduced range of ΔC_P which of course leads to reduced torque. Figure 4.8 shows contours of pressure and surface shear stress lines on the leading surface for the four shrouded cases at 850 rad/s. It can be seen that the general features of impingement/stagnation near the edge remain present for all of the configurations.

In Figure 4.9, the torque per unit width is plotted as a function of distance from the gear face for all four shrouds at 850 rad/s. All four configurations exhibit edge-
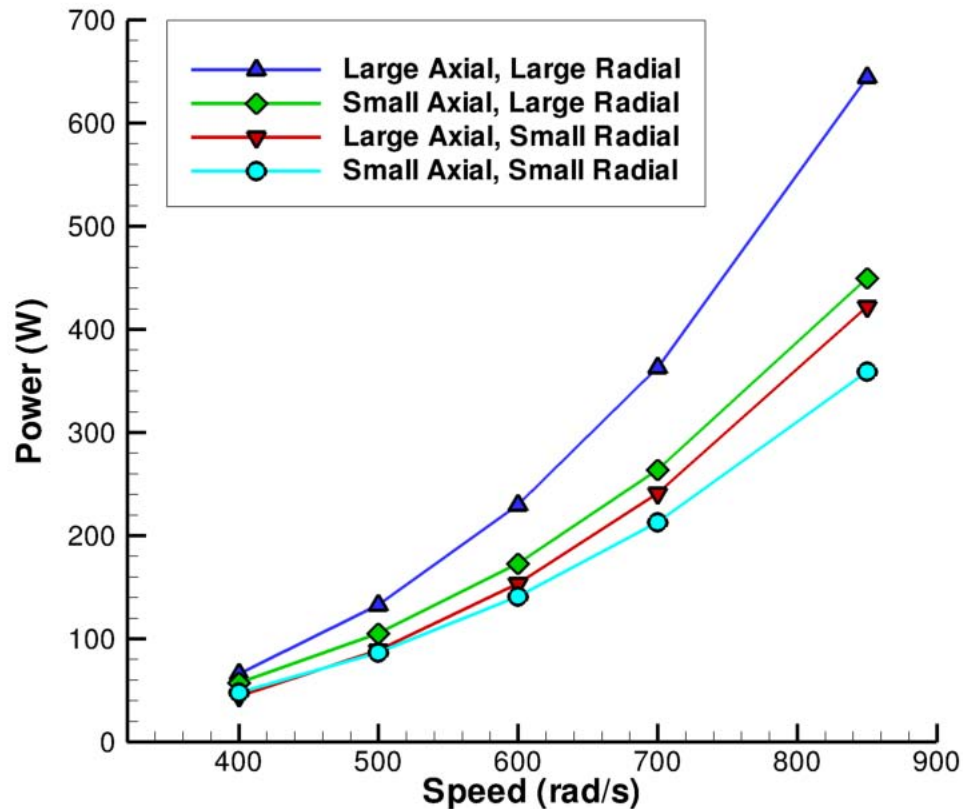
Figure 4.5. Comparison of predicted windage losses between the four shrouded Diab Gear 1 configurations.

loaded profiles, with their integrals consistent with the net loss trend reported in Figure 4.5. Comparing Figure 4.9 with Figure 3.22 shows the dramatic reduction in pressure torque that has been achieved for these configurations, but with retention of the basic features of the pressure torque distribution.

Figure 3.16 plotted viscous losses per unit span for the unshrouded Diab Gear 1 case, illustrating the increase in shear torque with rotation rate and span. The viscous losses per unit span are plotted for each of the four shrouded cases and the unshrouded case at 850 rad/s in Figure 4.10. There is it observed that face shear is smaller for all of the shrouded cases due to the "couette-flow-like" rotational boundary layer that arises in the presence of an outer axial boundary. Also of
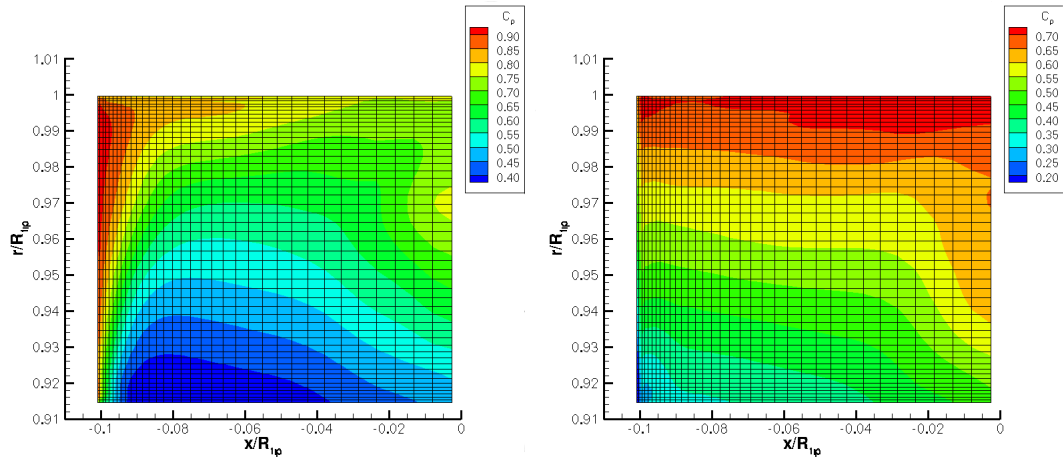
Figure 4.6. Static pressure coefficient contours on the leading tooth surface (left) and the trailing tooth surface (right) of the Large-Axial-Large-Radial shroud case at 850 rad/s. 1/2 of symmetrical gear shown.

interest in this figure is the increase in viscous loss for the Small-Axial shrouds compared to the Large-Axial shrouds. These losses are smaller than for the un-shrouded case but suggest that viscous losses can increase as a percentage of total loss for very small axial shroud clearances.
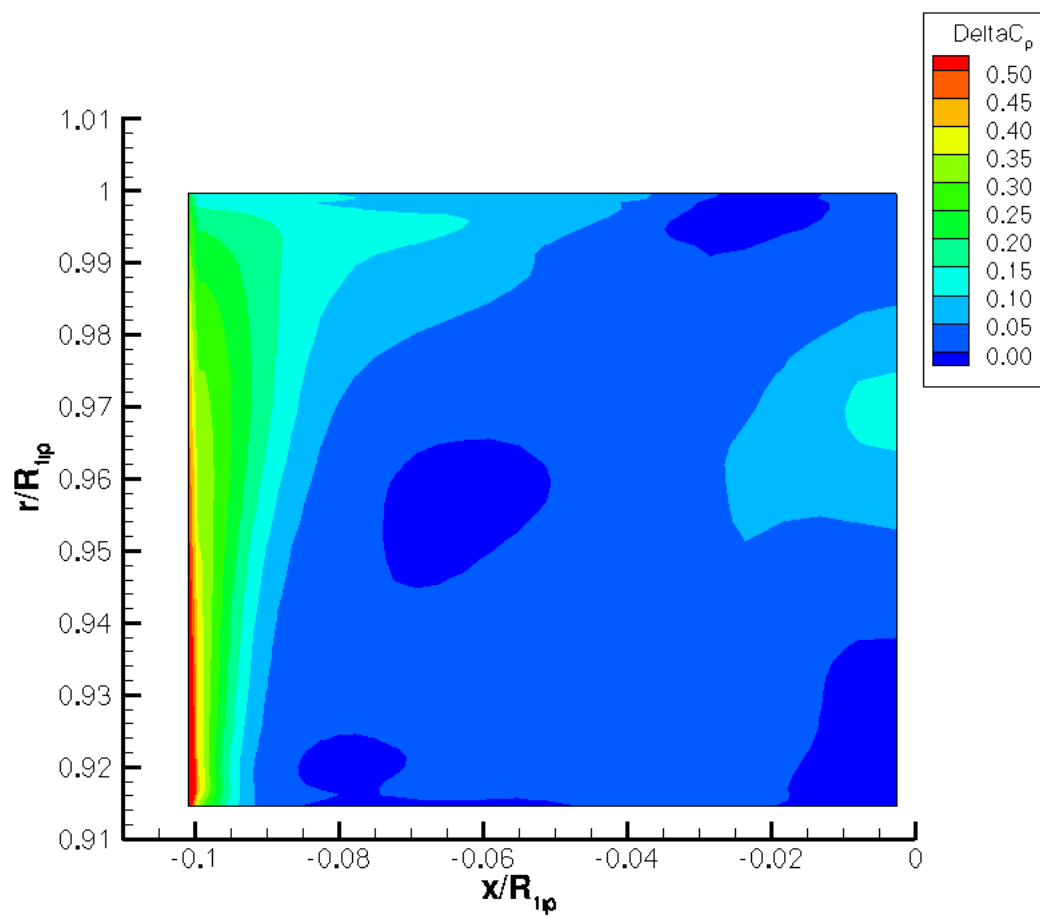
Figure 4.7. ΔC_P between gear leading and trailing tooth surfaces of the Large-Axial-Large-Radial shroud case at 850 rad/s. 1/2 of symmetrical gear shown.
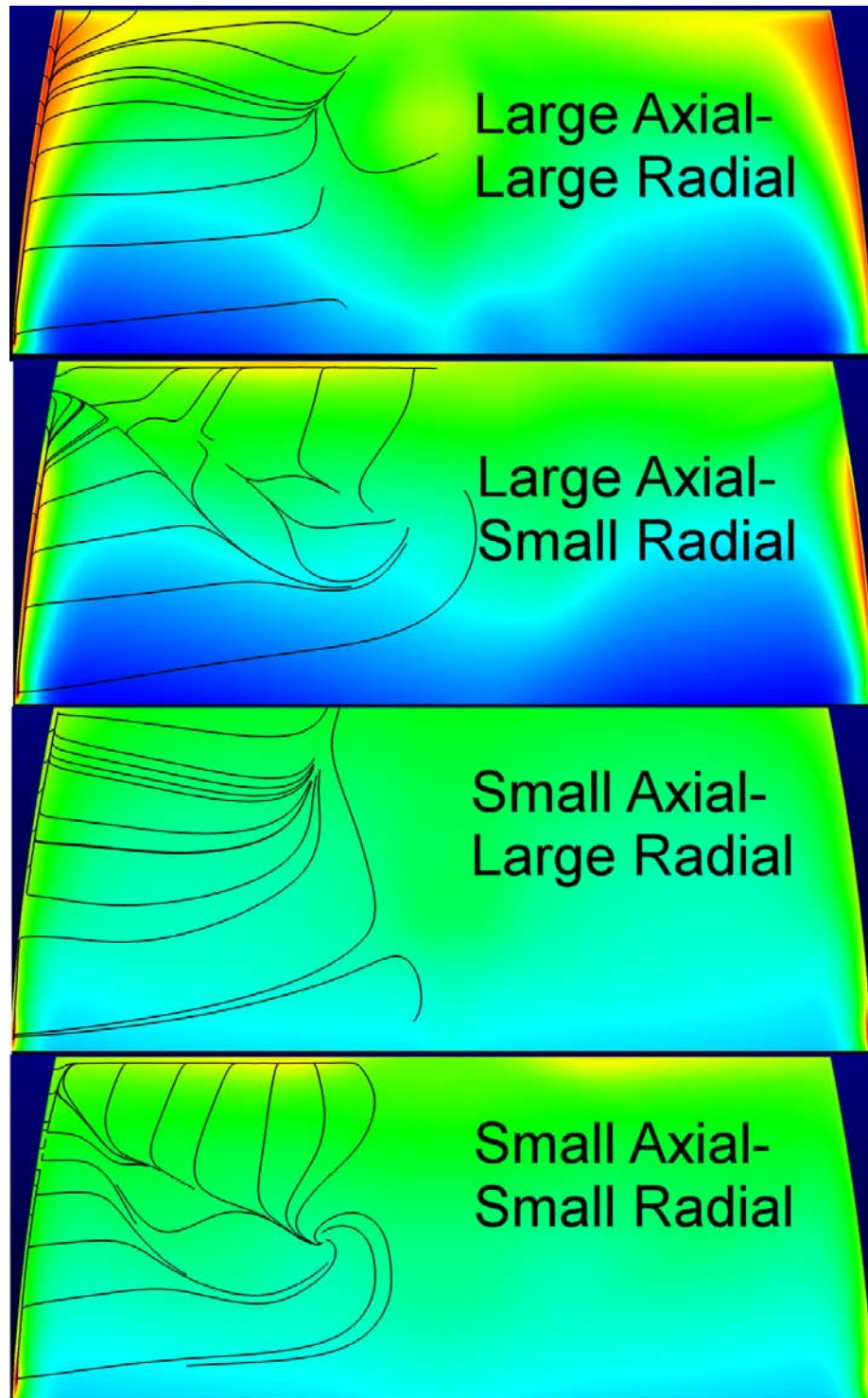
Figure 4.8. Contours of pressure and surface shear stress lines on the leading surface for the four shrouded cases at 850 rad/s.
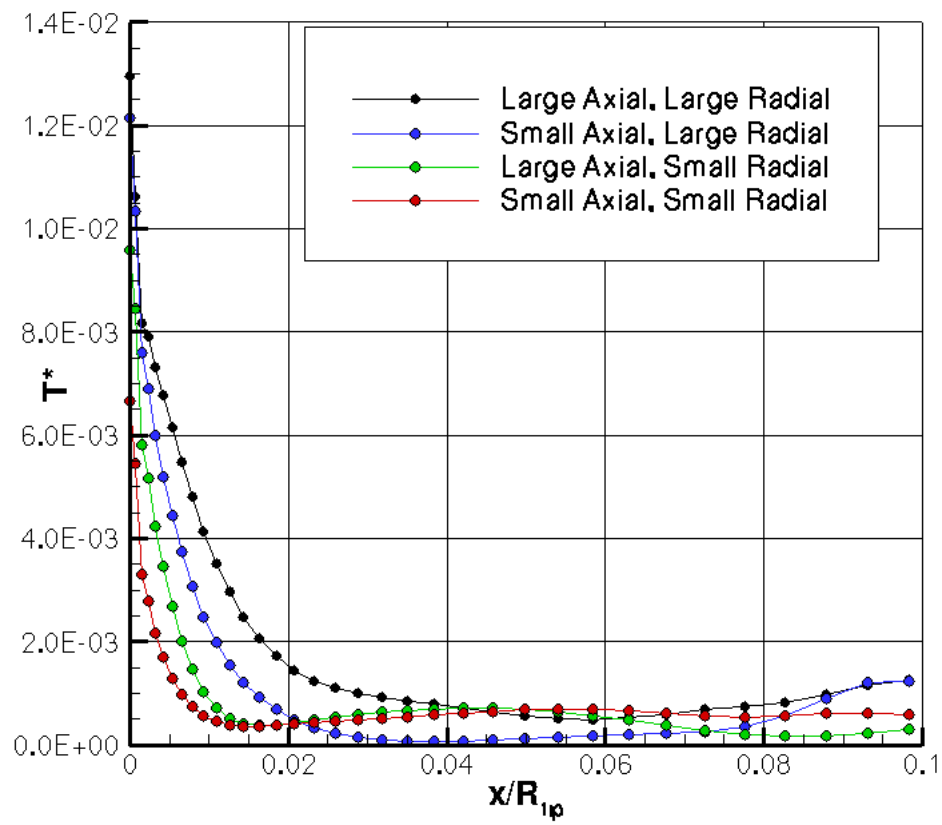
Figure 4.9. Torque per unit width on the tooth face for the four shrouded cases.
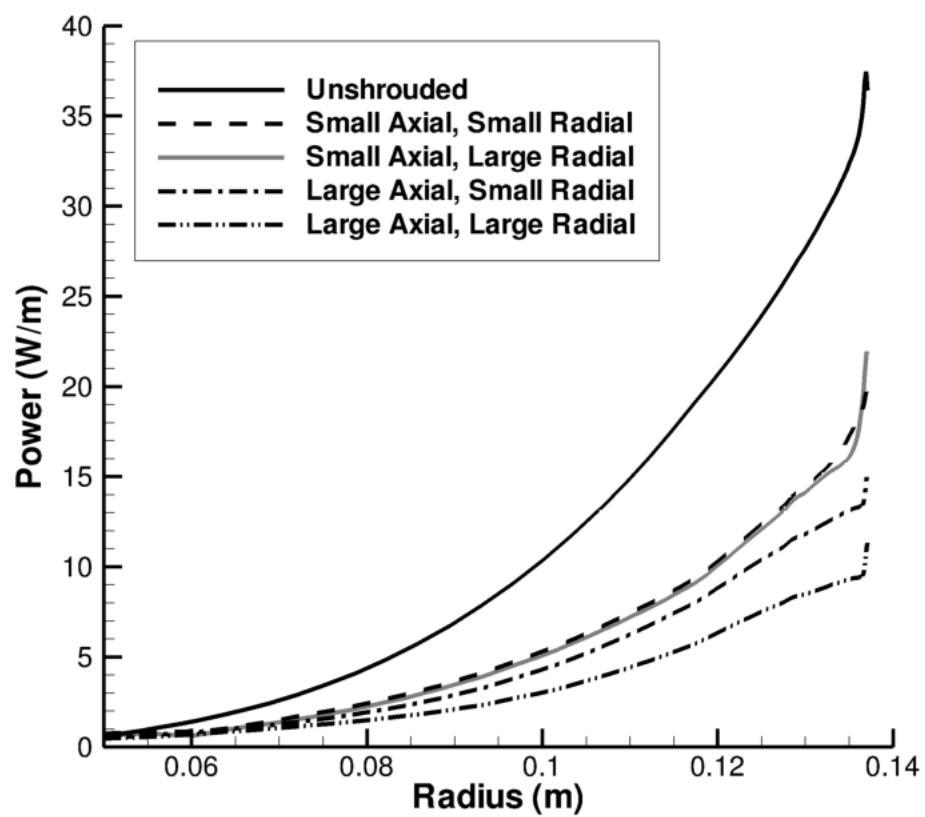
Figure 4.10. Comparison of viscous losses per unit span for Diab Gear 1 at 850 rad/s for unshrouded and four shrouded configurations.

4.2 Investigation of the Aerodynamics of Shrouding

It has been demonstrated both experimentally and computationally that enshrouding a gear reduces windage effects. However, up until now, very little has been revealed about how shrouds actually accomplish this reduction. Winfree [10] observed that shrouding a bevel gear reduced the ability of the gear to pump fluid from the gear axis and through its teeth. Essentially, that interpretation suggests that the shroud acts as a restrictor to limit the amount of fluid that the gear can can actually pump. This hypothesis can be tested for a spur gear with CFD using the results to compute the mass flow rate of fluid that passes through the gear teeth.

Figure 4.11 plots the integrated radial velocity entering/leaving the tooth region, which can be used to represent mass flow ($\dot{m} = \rho A V$) through the teeth (since density is constant) as a function of speed for unshrouded and shrouded configurations of Diab Gear 1. For all cases, the radial velocity is integrated over a surface that spans the tips of the gear teeth as illustrated in Figure 4.12. It can be seen that the mass flow through teeth of the shrouded gears is less than that of the unshrouded case. However, comparing just the unshrouded case with the Large-Axial-Large-Radial case, the difference in the mass flow rates is not significant enough to explain for the large difference in windage losses between the cases as seen previously in Figure 4.4. Thus, these results do support the Windfree hypothesis. Rather an alternative hypothesis has been developed, and this is presented and supported here.

Figures 4.13 and 4.14 provide a cross-sectional view of the solutions for the unshrouded and Large-Axial-Large-Radial cases, respectively, at 700 rad/s. The cut-planes are located along the center of the tooth well and display contours of tangential velocity (u_t^*). A zero tangential velocity (blue) indicates the fluid is close to quiescent. Values of positive tangential velocity indicate the fluid is traveling in the same direction as the rotation of gear. Figure 4.13 shows the radial ejection of the fluid from the teeth of the unshrouded gear at the centerline of the gear. It also shows that the ejected fluid has been given a tangential velocity component by the rotating gear. (The asymmetry in the u_t^* profile of the unshrouded case is
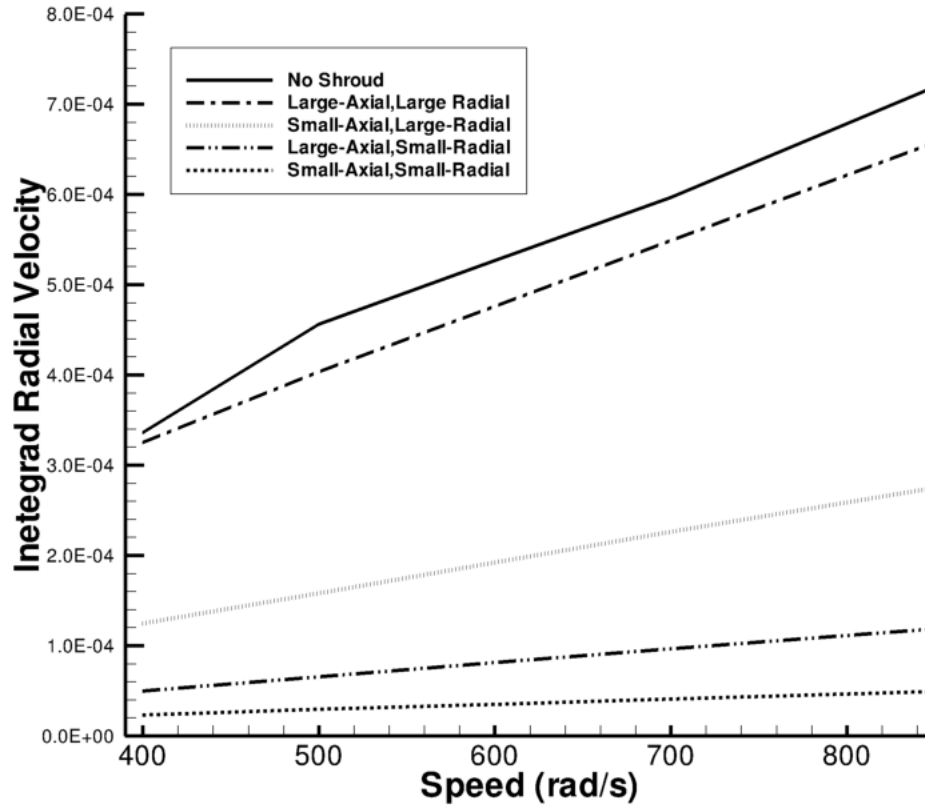
Figure 4.11. Integrated radial mass flow through gear tooth.

due to the small inflow velocity that is required by the CFD solver. This artificial through-flow was not found to effect the results.) However, for the shrouded case, shown in Figure 4.14, the ejected fluid does not completely escape from the gear. The shroud keeps the accelerated fluid within the vicinity of the gear, most notably near the gear teeth. The shroud confines the angular momentum imparted by the gear to the fluid within the vicinity of the teeth.

To further elucidate how this effect impacts windage losses, Figure 4.15 plots the nondimensionalized tangential velocity of the fluid along a line that runs parallel to the gear axis and through the tooth space at a radial location of $R/R_{tip} = 0.95$. It can be seen that as fluid approaches the gear face axially, the flow is immediately accelerated to the local tangential velocity of the gear. In both shrouded and
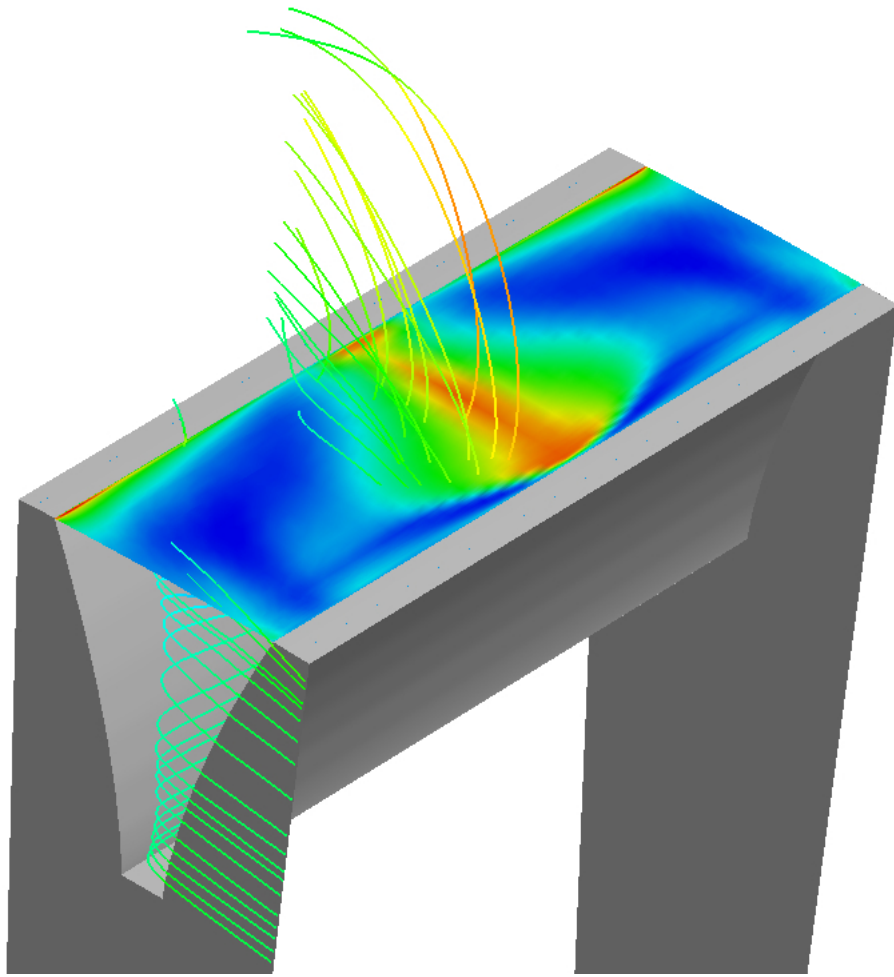
Figure 4.12. Integration surface for radial mass flow.

unshrouded cases, the flow is accelerated to the same tangential velocity upon entering the tooth space, but with the shrouded case experiencing a significantly smaller change in velocity. This difference reveals the dominant mechanism by which shrouding reduces the windage losses. Above it was shown that for all cases studied, shrouded and unshrouded, the near-face, near-tooth flow is drawn into the tooth passage, by virtue of, lower pressures within the tooth passage. This flow impinges on the leading tooth surface and the attendant stagnation pressure rise was observed to give rise to dominant component of the windage torque. The foregoing angular momentum results show conclusively that this deceleration and attendant pressure rise is much smaller for the shrouded gears since the local
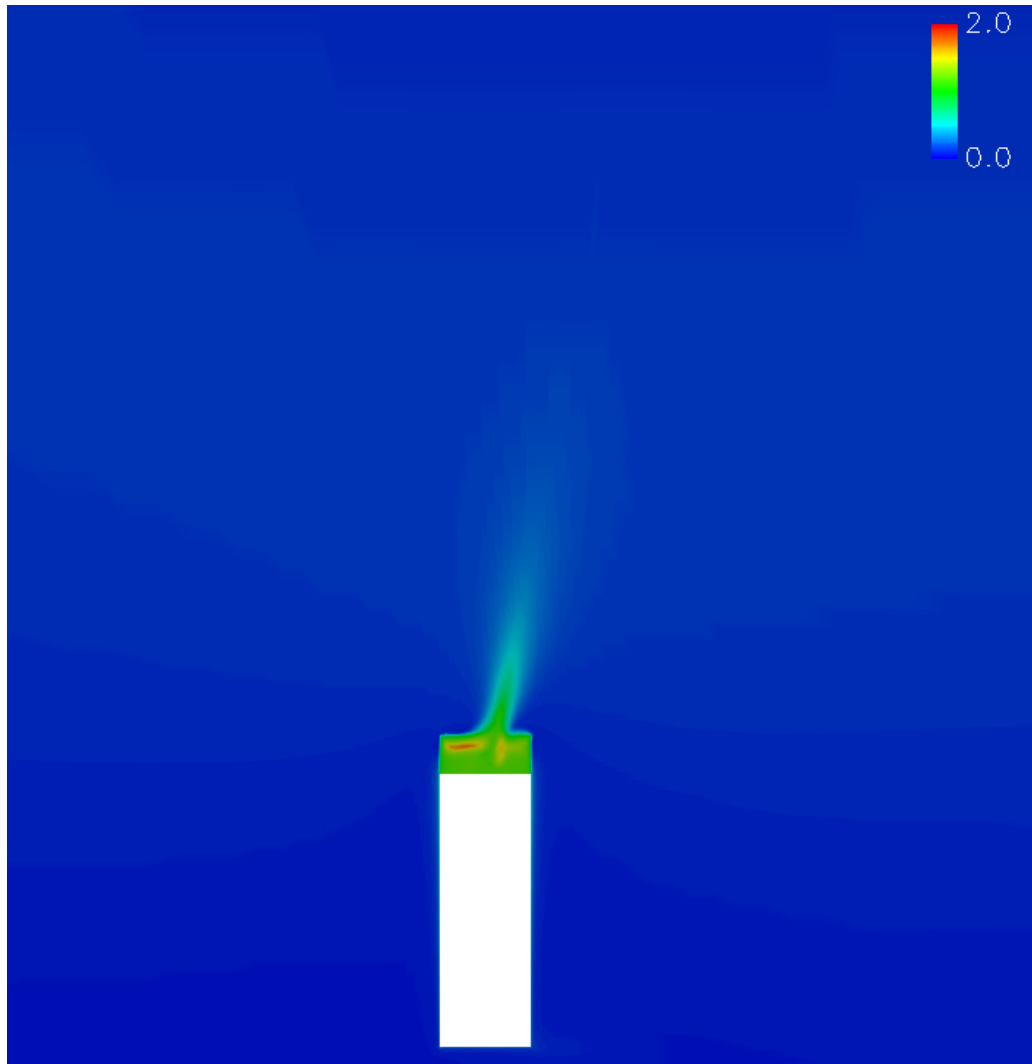
Figure 4.13. Contour plot of tangential velocity for unshrouded Diab Gear 1 at 700 rad/s.

tangential velocity of the flow is much closer to the that of the gear. By conserving the angular momentum imparted by the gear on the fluid, the shrouded gear uses less force to pump the fluid. Examining the tangential velocity profiles at different radial locations in Figure 4.16, it can be seen how viscous shear losses are also affected by shrouding. By conserving the tangential velocity of the fluid near the gear, the viscous drag experienced by the gear is reduced since less work is required to accelerate the fluid to the speed of the gear.
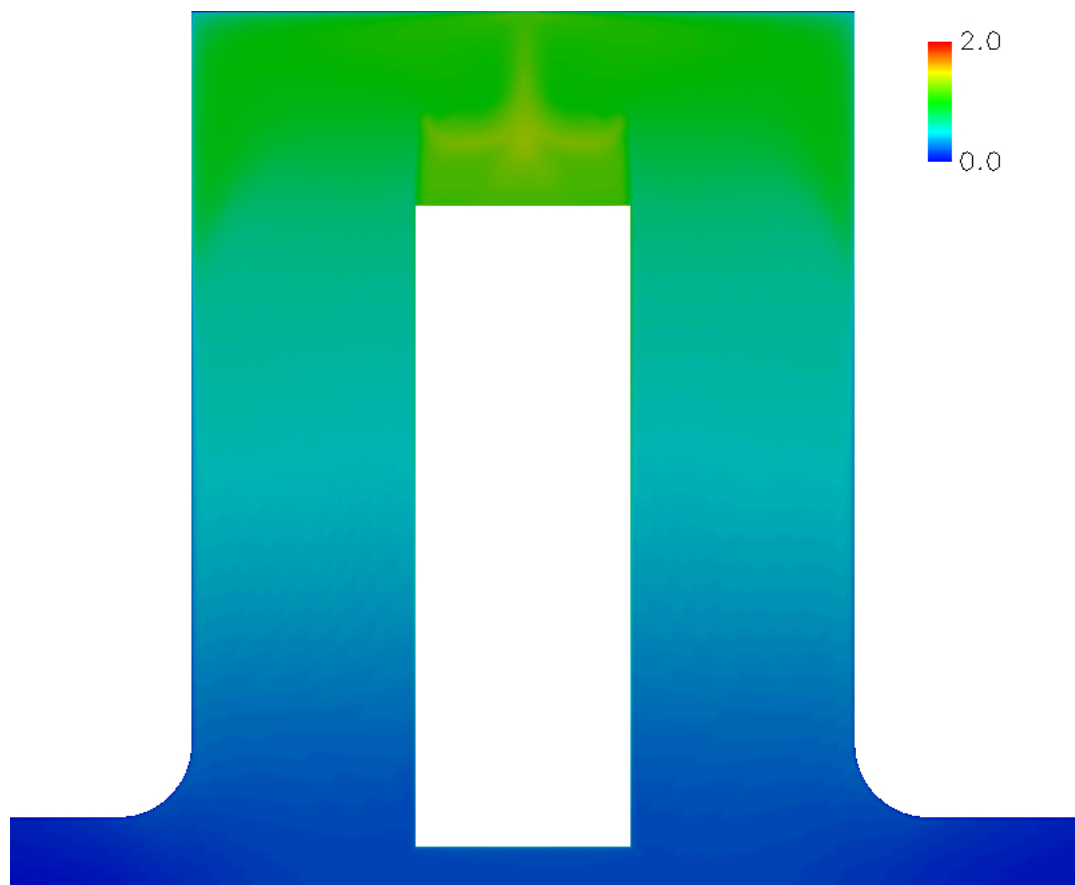
Figure 4.14. Contour plot of tangential velocity for the Large-Axial-Large-Radial shroud case at 700 rad/s.
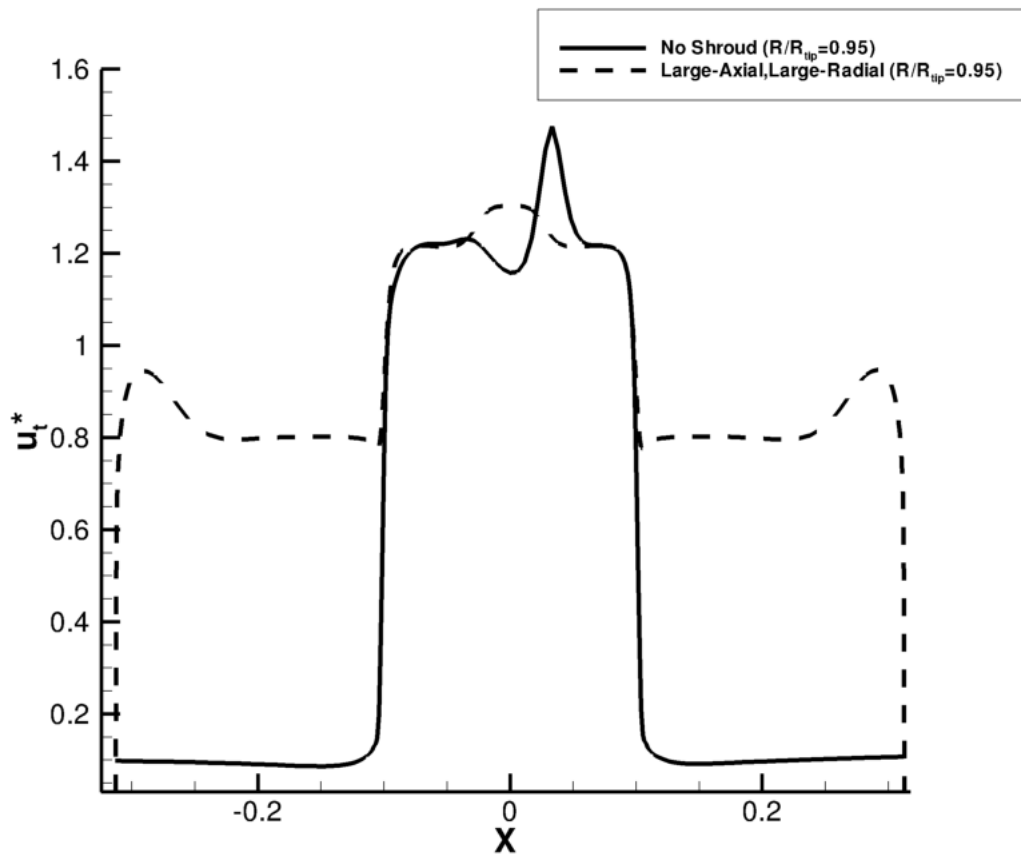
Figure 4.15. Comparison of tangential velocity profiles along $R/R_{tip} = 0.95$ between the unshrouded and the Large-Axial-Large-Radial shroud cases.
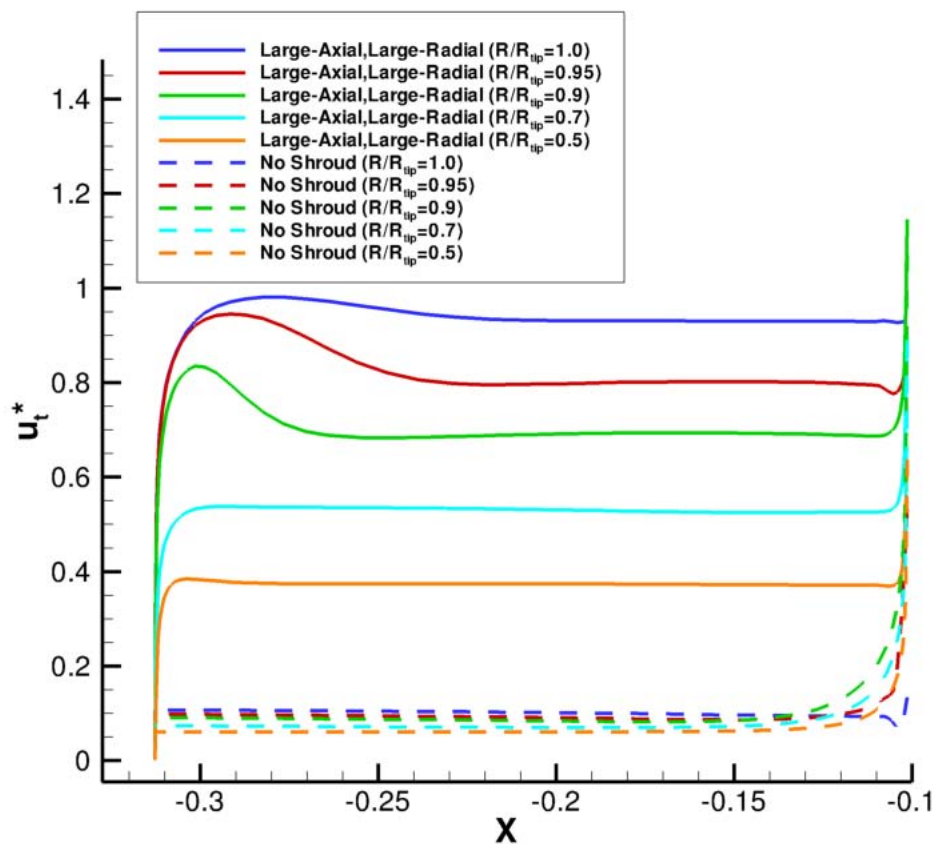
Figure 4.16. Comparison of tangential velocity profiles at different radial locations between the unshrouded and the Large-Axial-Large-Radial shroud cases.

To further examine the physics of shrouding, two modifications of the Large-Axial-Large-Radial shroud configuration were tested. Openings were placed on the outer radial boundary in each case, but at different locations. In the first modification, slots were placed at the corners of the shroud as shown in Figure 4.17. In the second, just a single slot was inserted directly above the center of the gear. Figure 4.18 provides a view of this configuration. It can be seen in both cases that a large outer domain was added to the original grid outside of the shrouded domain. This was done because the flow conditions at the openings were unknown and any outlet boundary condition could impose an arbitrary flow there.
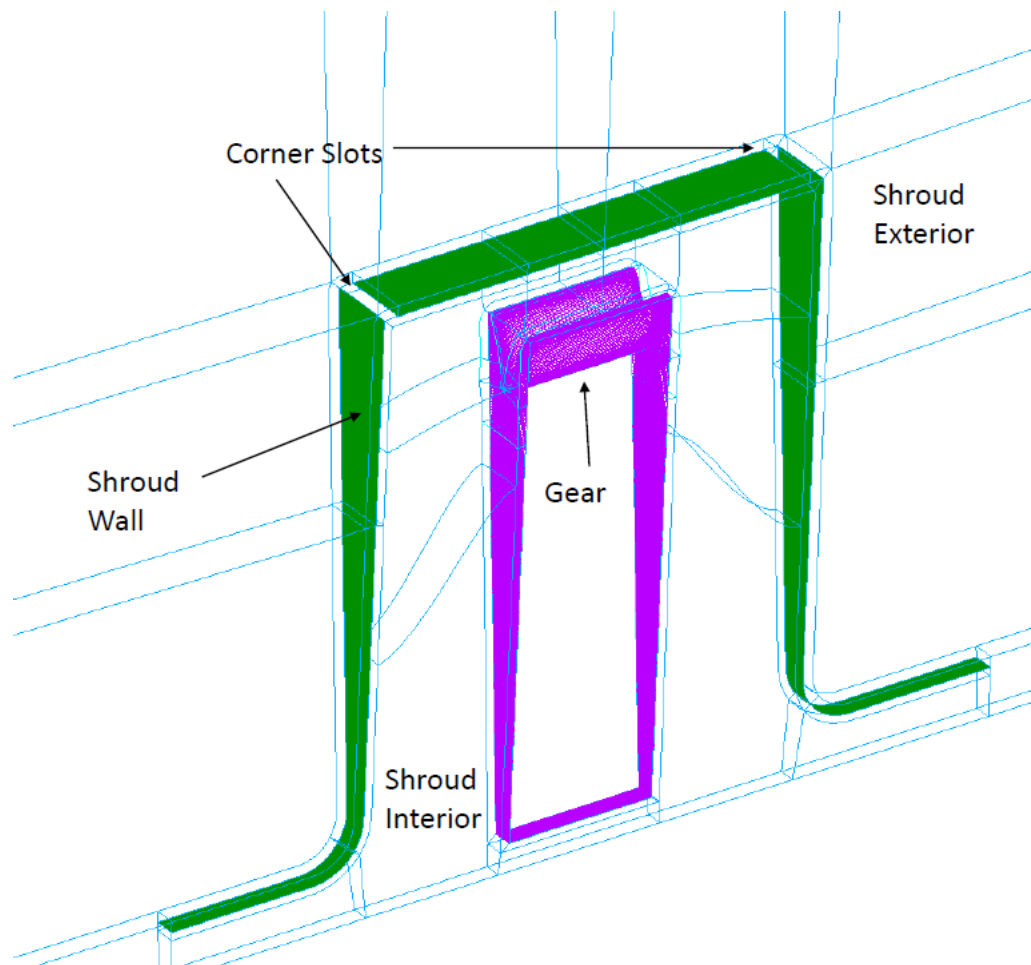
Figure 4.17. Grid topology of the Large-Axial-Large-Radial shroud with corner slots.

Each case was run at a speed of 700 rad/s and in both cases the beneficial effect of the shrouds was significantly reduced. The results are plotted in Figure 4.19.
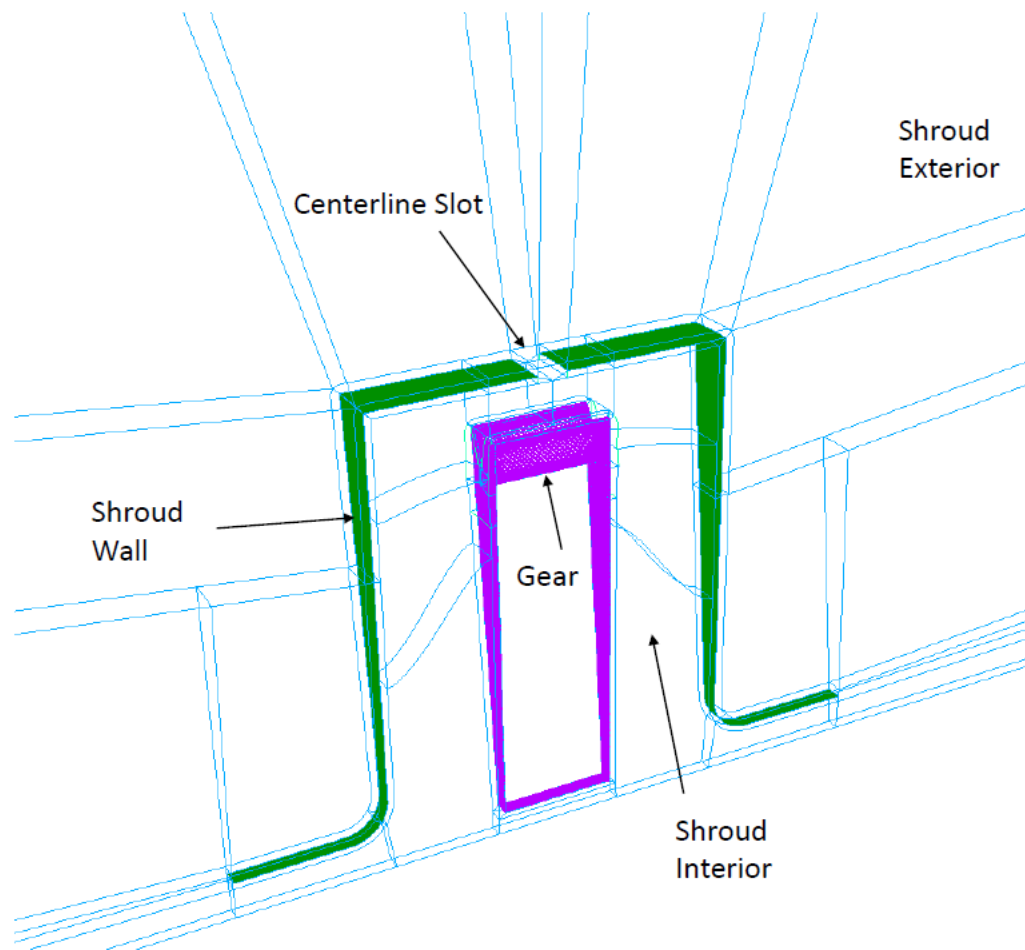
Figure 4.18. Grid topology of the Large-Axial-Large-Radial shroud with centerline slot.

The corner slotted case provided only a 19% decrease in windage compared to the unshrouded case at 700 rad/s and the centerline slotted case returned a 13% decrease in windage loss at the same speed. In contrast, the fully shrouded configuration provided a 68% decrease at 700 rad/s. As can be seen in Figures 4.20 - 4.23, the slots allow the fluid accelerated by the gear to escape away from the gear. Figures 4.20 and 4.22 provide contour profiles of tangential velocity of the two configurations. Figures 4.21 and 4.23 include three dimensional absolute frame streamlines with the contour profiles of tangential velocity showing the leakage of angular momentum from the shroud. This effect is further quantified by Figure 4.24 which plots the nondimensionalized tangential velocity in the same manner

as Figure 4.15. Here we see that the tangential velocity of the fluid entering the teeth is much closer in value to the unshrouded case than the fully shrouded case.
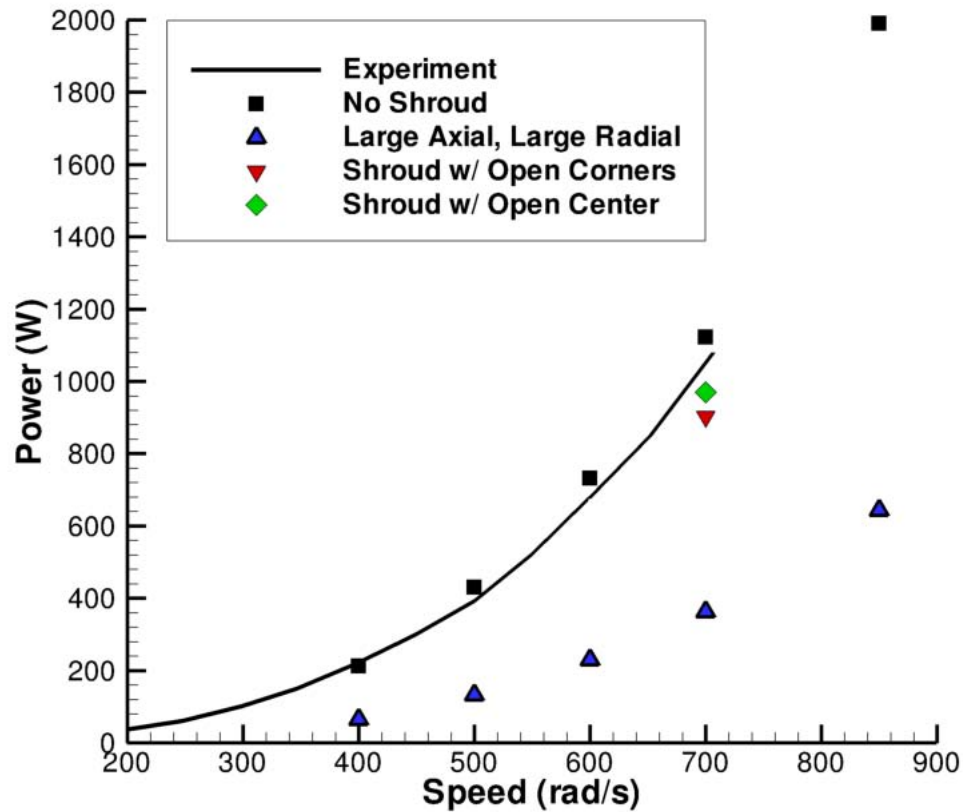
Figure 4.19. Comparison of predicted windage losses between the unshrouded, the fully enclosed Large-Axial-Large-Radial shroud, and slotted Large-Axial-Large-Radial shroud configurations.

Figure 4.25 provides the tangential velocity profiles along $R/R_{tip} = 0.95$ for the unshrouded and fully shrouded gear configurations. Here it seen why the large axial shroud cases experience less viscous torque than the small axial cases as first observed in Section 4.1. The tighter clearances do not leave much room between the walls of the shroud and the gear face to decrease the Δu_t between the surfaces. Figures 4.26 - 4.28 provide contour profiles of tangential velocity of the Large-Axial-Small-Radial, Small-Axial-Large-Radial, and the Small-Axial-Small-Radial cases,
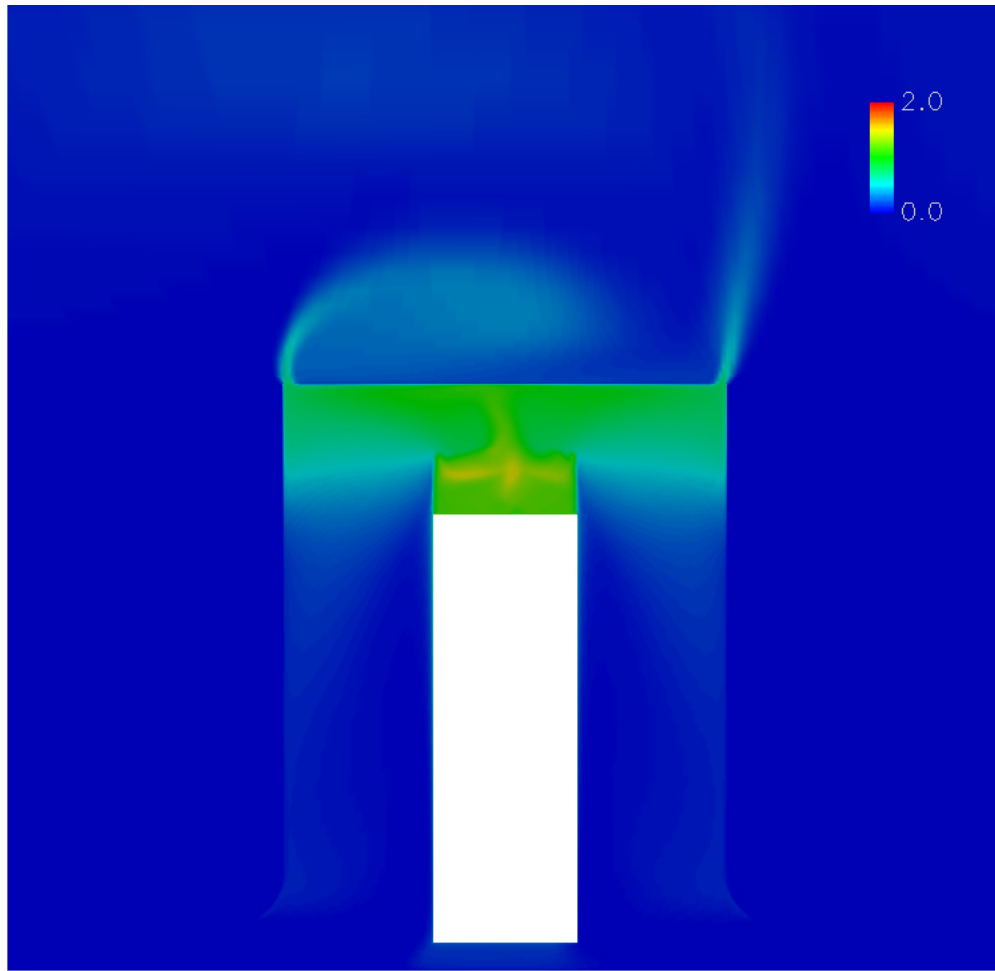
Figure 4.20. Contour plot of tangential velocity for the Large-Axial-Large-Radial shroud with corner slots at 700 rad/s.

respectively. Here, it is observed that the tighter shrouds keep the accelerated flow much closer to vicinity of the gear teeth. Figure 4.25 also shows that the Δu_t is greater for the tighter three shroud configurations, yet windage losses are still smaller for these cases. This is explained by recalling Figure 4.12. The three tighter shroud configurations experience less mass flow through the teeth and are thus accelerating less fluid per unit time than the Large-Axial-Large-Radial case. Thus these cases experience less windage power loss.
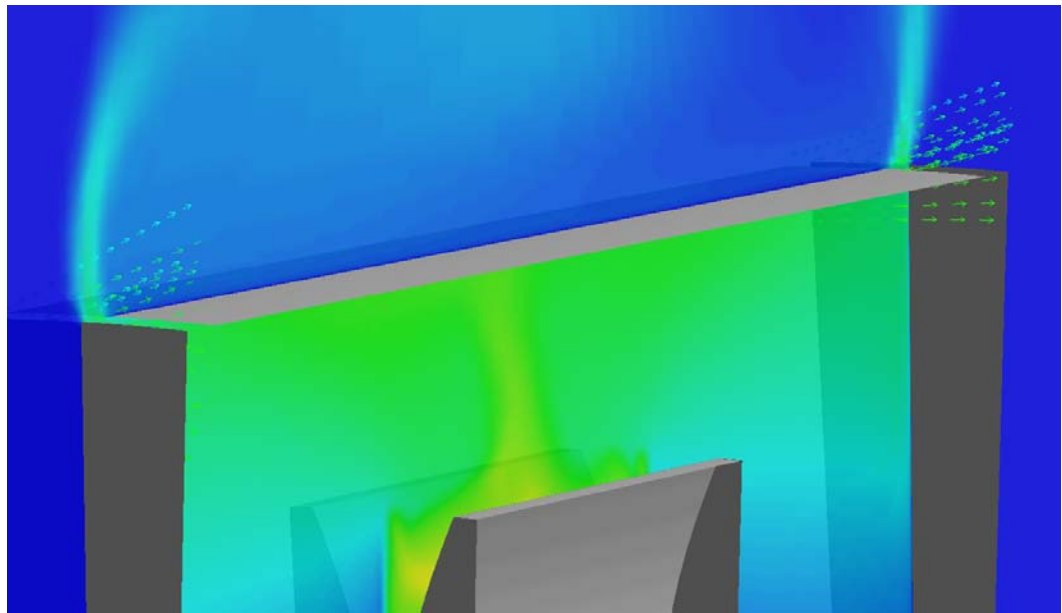
Figure 4.21. Three-dimensional absolute frame streamlines for the Large-Axial-Large-Radial shroud with slots at the corner at 700 rad/s.
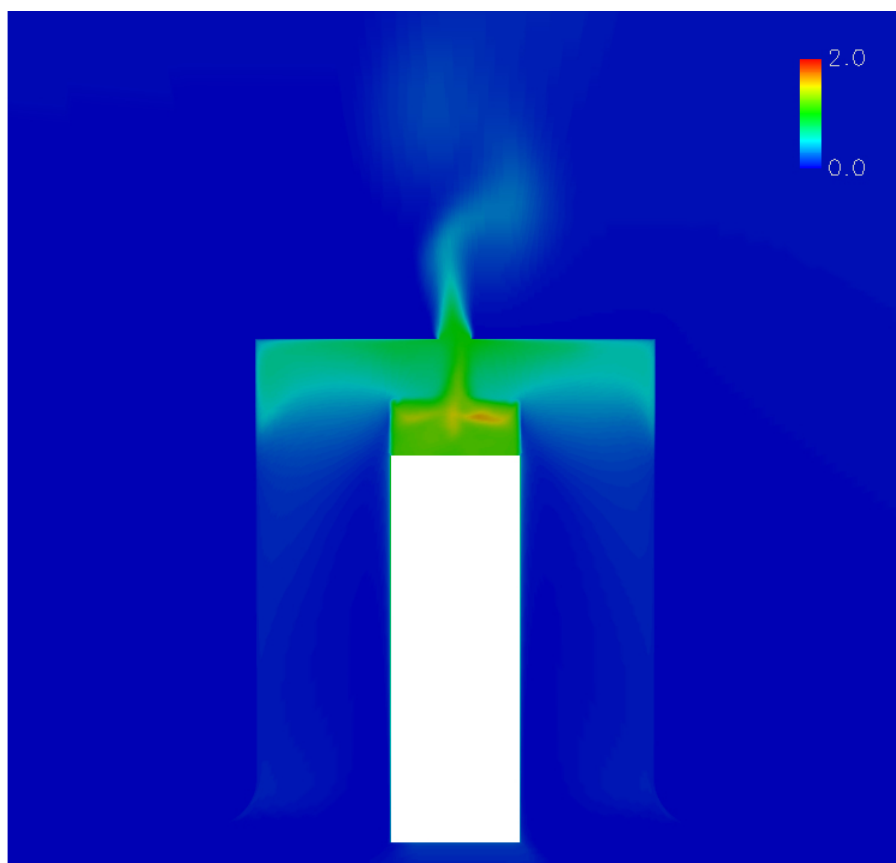
Figure 4.22. Contour plot of tangential velocity for the Large-Axial-Large-Radial shroud with centerline slot at 700 rad/s.
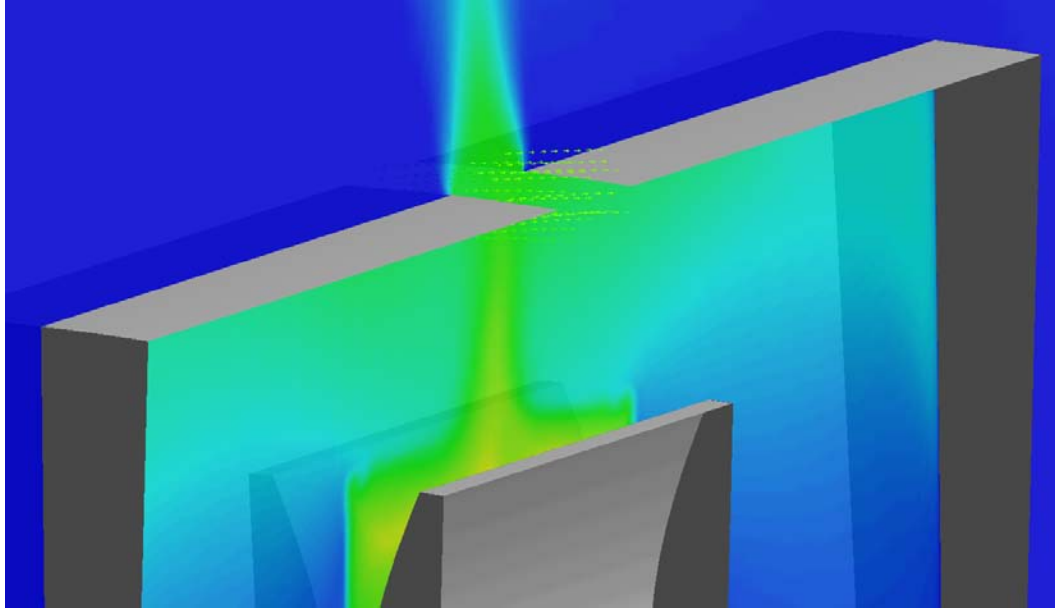
Figure 4.23. Three-dimensional absolute frame streamlines for the Large-Axial-Large-Radial shroud with centerline slot at 700 rad/s.
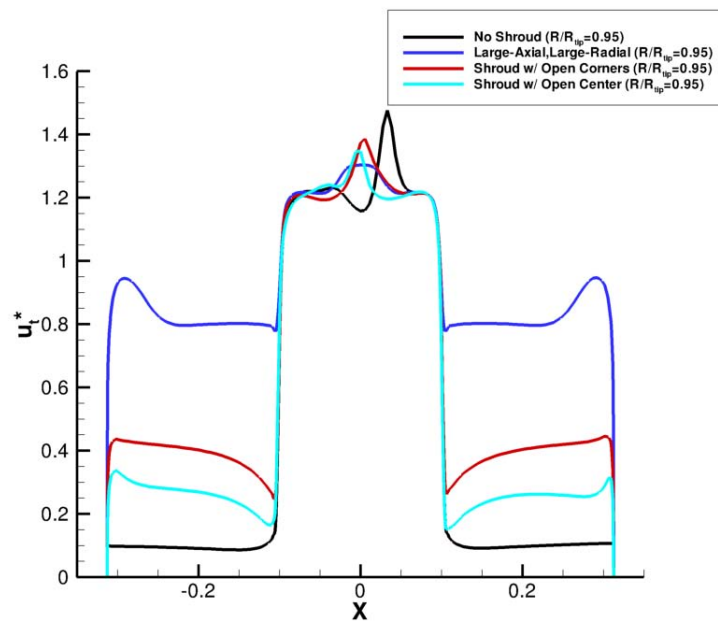

**Figure 4.24.** Comparison of tangential velocity profile along $R/R_{tip} = 0.95$ between the unshrouded, the fully enclosed Large-Axial-Large-Radial shroud, and slotted Large-Axial-Large-Radial shroud configurations.
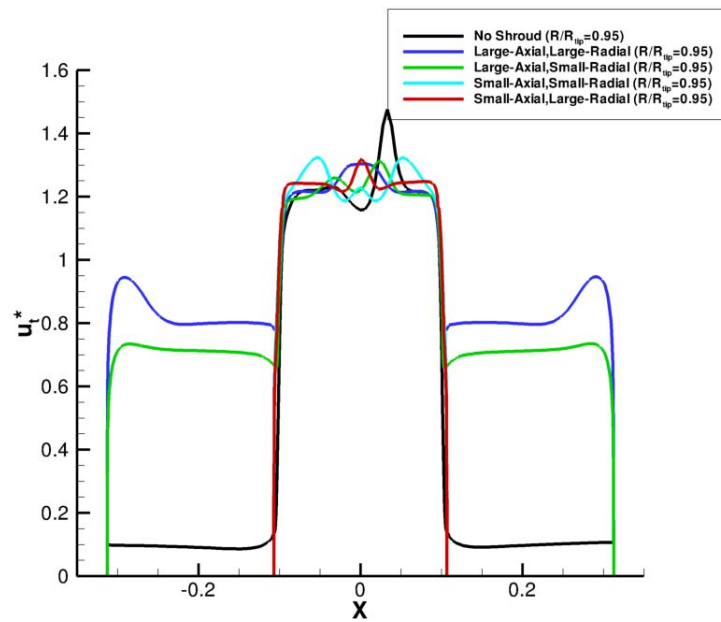
Figure 4.25. Comparison of tangential velocity profile along $R/R_{tip} = 0.95$ for the unshrouded and the four fully enclosed shroud configurations.

Figure 4.26. Contour plot of tangential velocity for the Large-Axial-Small-Radial case at 700 rad/s.
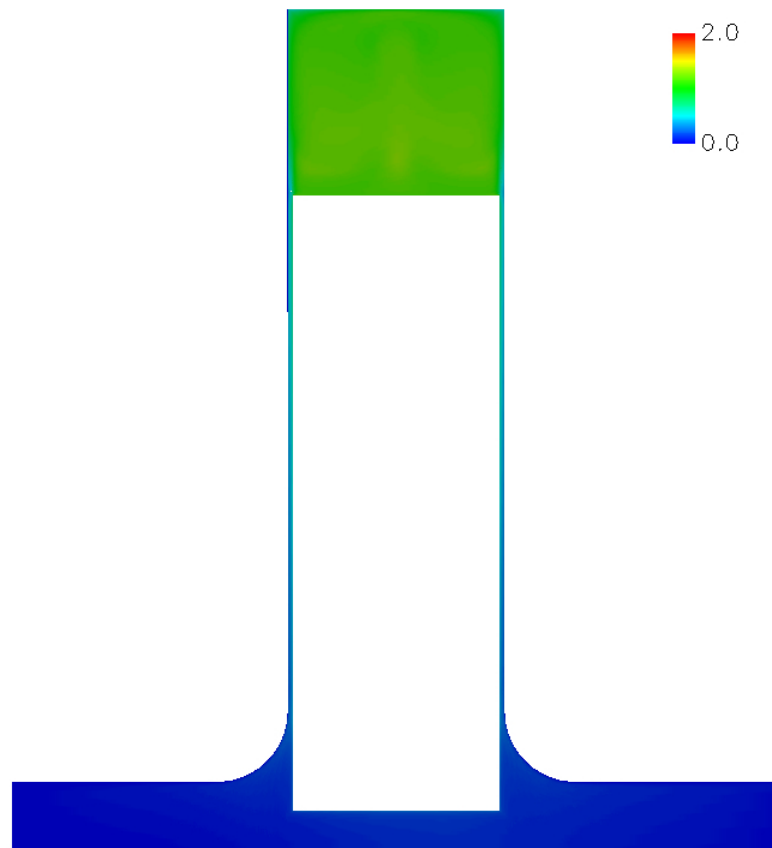
Figure 4.27. Contour plot of tangential velocity for the Small-Axial-Large-Radial case at 700 rad/s.
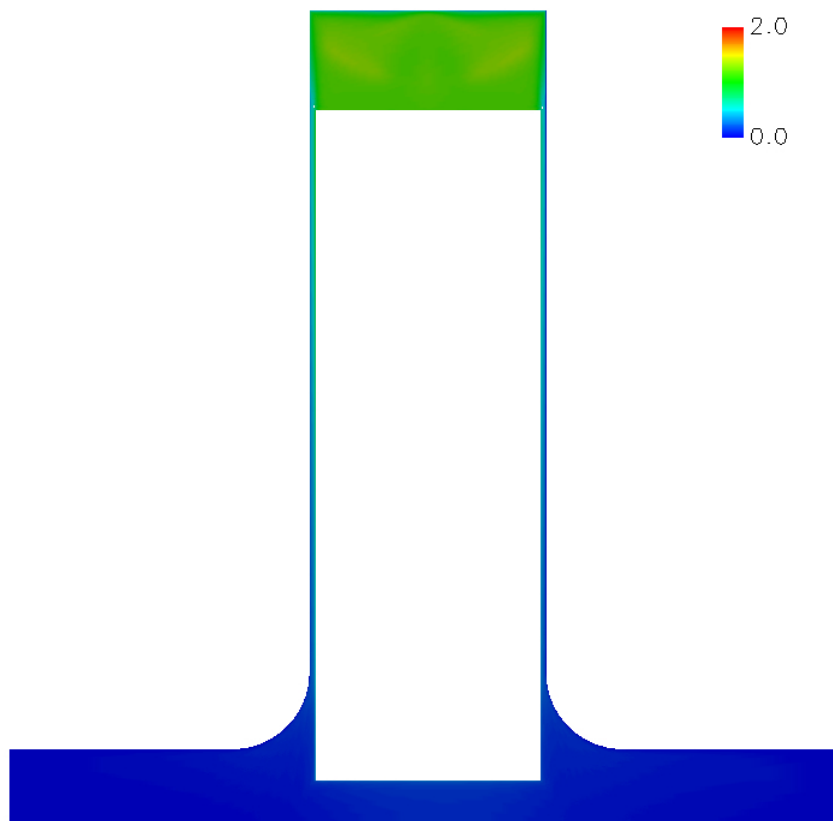
Figure 4.28. Contour plot of tangential velocity for the Small-Axial-Small-Radial case at 700 rad/s.

4.3 NASA Glenn Tests

The NASA Glenn Research Center has recently installed a gear windage test facility [7]. The test facility is designed to parametrize the effects of gear geometry, shroud geometries and sizes, different lubrication system configurations, system pressures and temperatures, and gear meshing on windage loss. A sketch of the test facility is shown in Figure 4.29 and Figure 4.30 is a photo of facility. The facility has a 150 hp (112 kW) DC drive motor that is connected to a 5.7:1 speed-up gearbox. The output of the speed-up gearbox is then connected to a torque meter prior to a coupling connection of the input shaft to the test gearbox. The input and output shafts have hydraulically operated clutches that allow the facility (in single or dual shaft mode) to be disconnected from the power source and/or magnetic brake attached to the output shaft. With the speed capability of the drive motor and speed increasing gearbox and the dimensions of the test specimen, the pitch line velocity can be as high as 280 m/s (55,000 ft/min).

The test gears can be run in the gearbox with or without shrouding. The shrouding clearance can be adjusted radially and axially. The details of the gear under study here is given in Table 4.2 and the maximum and minimum shroud clearances are provided in Table 4.3. The gear has some modest geometric complexities compared to the idealized Diab gear studied previously. These include chamfered teeth, filleted teeth roots, and a narrower body width between the teeth and the hub. This dissertation reports the data for and analyses of the four extreme shroud configurations: Large-Axial-Large-Radial, Large-Axial-Small-Radial, Small-Axial-Large-Radial, and Small-Axial-Small-Radial. A sketch of the shrouding arrangement is shown in Figure 4.31.

Table 4.2. Basic Gear Dimensions

Number of teeth	52
Module (Diametral Pitch), mm (1/in.)	6.35 (4)
Face Width, mm (in.)	28.4 (1.12)
Pitch Diameter, mm (in.)	330.2 (13.0)
Pressure Angle, deg.	25.0
Outside Diameter, mm (in.)	342.65 (13.49)
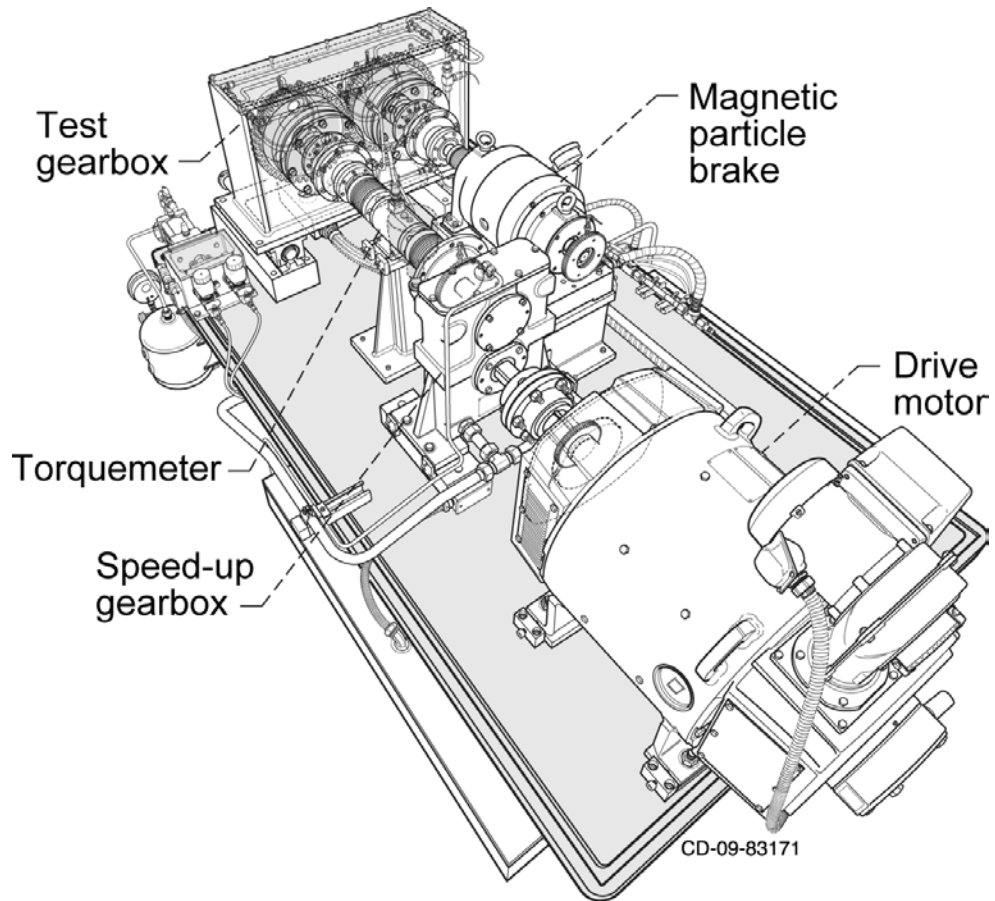
Figure 4.29. Overview sketch of the the NASA Glenn Research Center Gear Windage Test Facility. [7]

Table 4.3. Shroud Wall Clearances Studied

	Minimum	Maximum
Axial, mm (in.)	0.762 (0.030)	29.718 (1.17)
Radial, mm (in.)	0.762 (0.030)	16.65 (0.655)

Data from the NASA Windage Test Stand was measured in the following manner. Speed data is measured using inductive pickups that read a 60 tooth disc on the end of each of the shafts. The output from the sensor (pulse / sine wave) is sent to a frequency-to-voltage converter. The output from the converter is then sent to a National Instruments card and read by Labview. Data was taken at 10
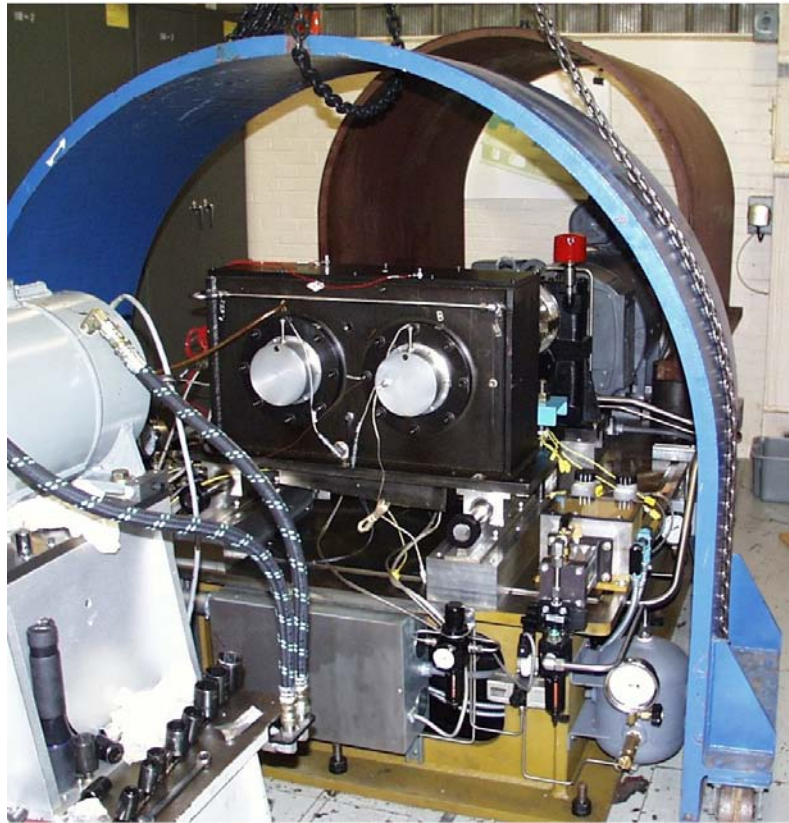
Figure 4.30. Photograph of the NASA Glenn Gear Windage Test Facility with containment shielding in place.

Hz. The facility was operated at a series of increasing drive motor speeds. At each of these conditions several different data were collected. The drive motor speed, torque applied to rotate the test hardware, internal shroud (fling-off) temperature, and internal shroud static pressure data were taken at steady drive motor speed conditions. Data was taken and then the speed was incremented from a given drive motor speed of 500 to 3125 RPM (or 2587 to 16168 RPM of the gear shaft). The data was taken from motor controller speed, a commercially available torque meter for torque, a thermocouple for inside shroud temperature (oil fling-off), and a manometer. In order to determine the effects of the gear-only windage a separate test was conducted with the entire system in place minus the gear [7].

Figure **??** was adapted from Ref. [7] and reports the air-only gear windage power loss results for a number of tested configurations. This figure includes air-only data from the unshrouded configuration, the fully enclosed shroud configurations, and
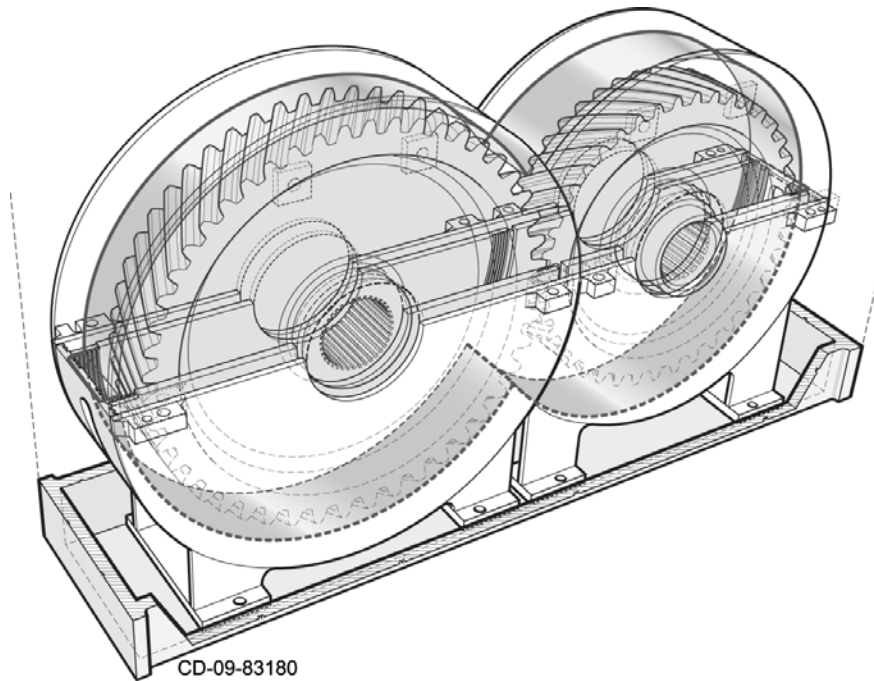
Figure 4.31. Shroud assembly for test facility. [7]

the slotted shroud configurations. The slotted shroud configurations include a 1-inch circumferential drain slot at the bottom of the shroud to allow for lubrication testing. Figures 4.32 and 4.33 demonstrate the effect that was observed in the CFD analysis performed in Section 4.2. By adding an opening at the periphery of a shroud, the windage losses increase on a spur gear.

4.3.1 NPHASE-PSU Results

An overset grid system was developed for the 13-inch pitch diameter spur gear configuration. The grid system was designed to facilitate comparisons between different shroud configurations. One grid system describes the gear, and different shroud designs are simply swapped out using the overset grid methodology provided by SUGGAR. The gear is described by a mesh consisting of 234 component grids that add up to 15.7M cells. Figure 4.34 depicts the near-body grid topology of the grid. Figure 4.35 illustrates the overset topology of the unshrouded configuration which has 23.4M total cells. Like the previous NPHASE-PSU simulations (Section 3.1), the single plane of symmetry at the gear centerline was exploited in
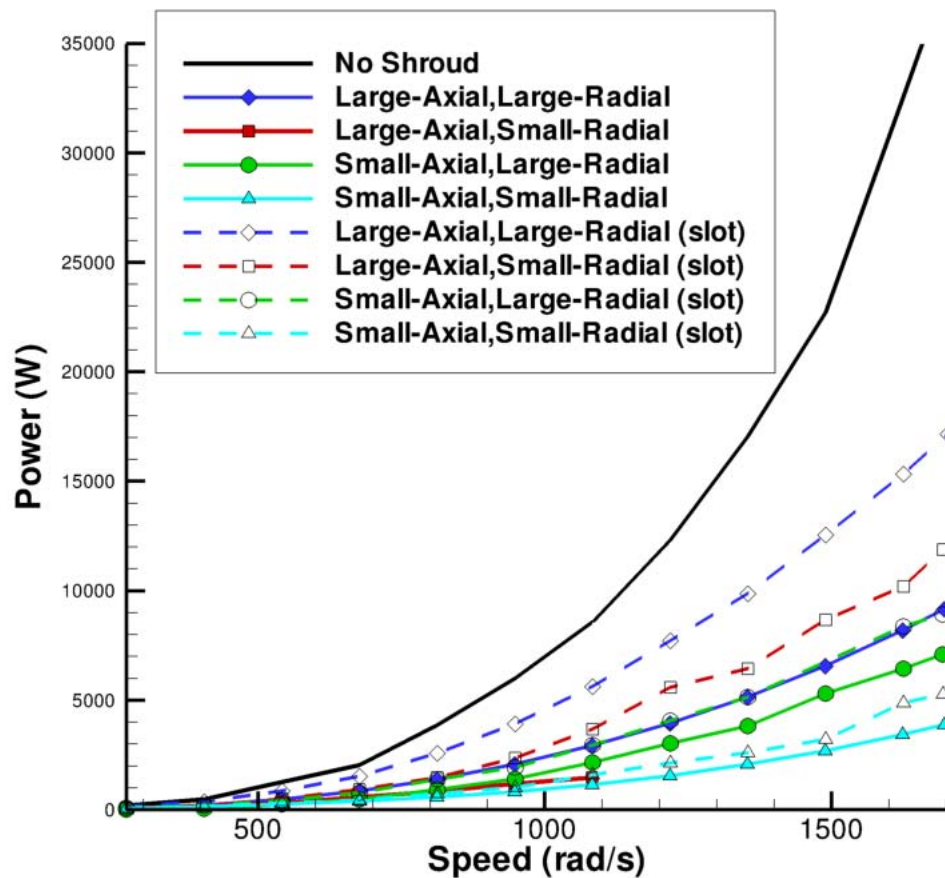
Figure 4.32. NASA experimental gear windage power loss data for 13-inch spur gear for the shrouded and unshrouded configurations. [7]

the grid construction to reduce grid size.

Overset meshes were also constructed for the Large-Axial-Large-Radial and the Large-Axial-Small-Radial configurations. The Large-Axial-Large-Radial configuration had a total cell count of 26M cells and the Large-Axial-Small-Radial case had approximately 36.6M cells. Reducing the clearances between the gear and shrouds required an increase in the number of cells in order to provide sufficient overlap between the overset meshes. Unfortunately, these cases were never able to achieve a converged solution.

Figure 4.36 shows NPHASE-PSU results against experimental data for the unshrouded 13 inch NASA spur gear. The NPHASE-PSU results slightly over-
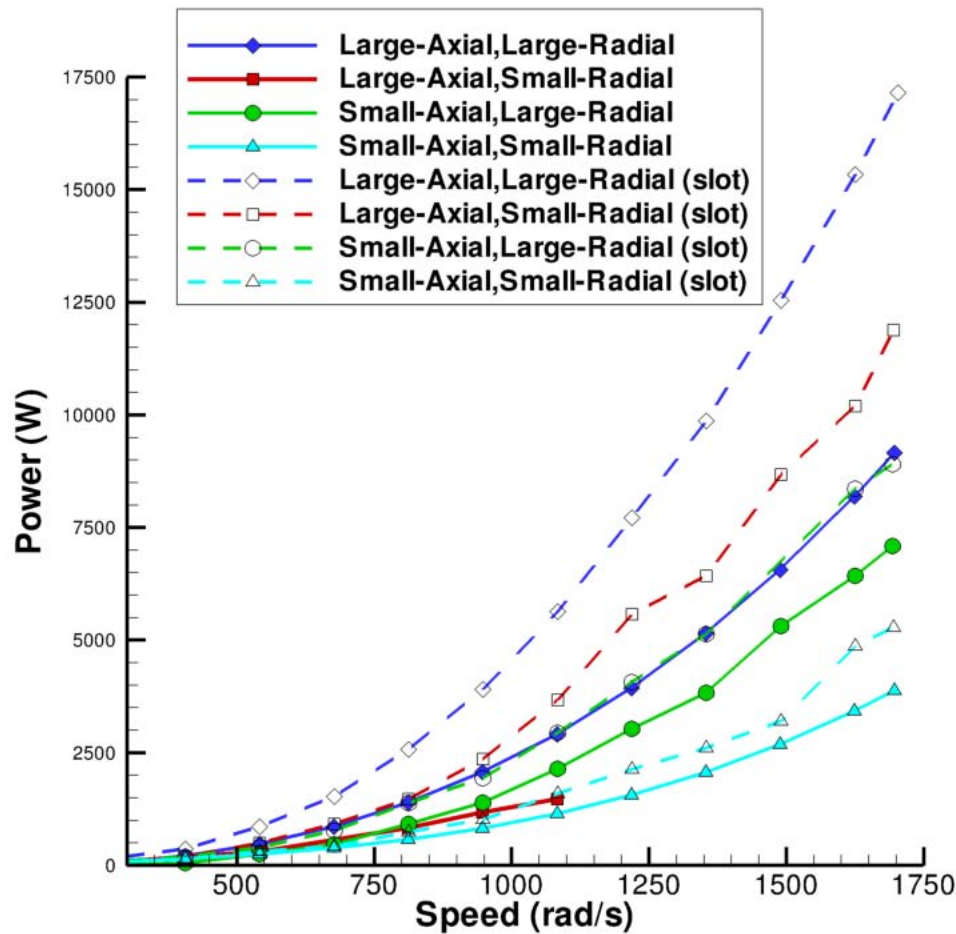
Figure 4.33. NASA experimental gear windage power loss data for 13-inch spur gear for only the shrouded configurations. [7]

predict the experimental results, which is not unexpected, but there is otherwise good agreement with the experimental data. In the unshrouded experiment, the shroud assembly and the top lid of the gearbox are removed. However, the rest of the gearbox housing remains in place. In the CFD model, the outer walls of the gearbox were not included. As was demonstrated in Section 4.1, even open shrouds will provide some reduction in windage losses. Figure 4.37 shows the predicted relative frame streamlines at 1000 rad/s along with iso-surfaces of high pressure. This figure exhibits several of the features observed for the idealized case including the diversion of the near face flow into the tooth passage and its impingement on the leading surface, a strong axial secondary vorticity in the tooth
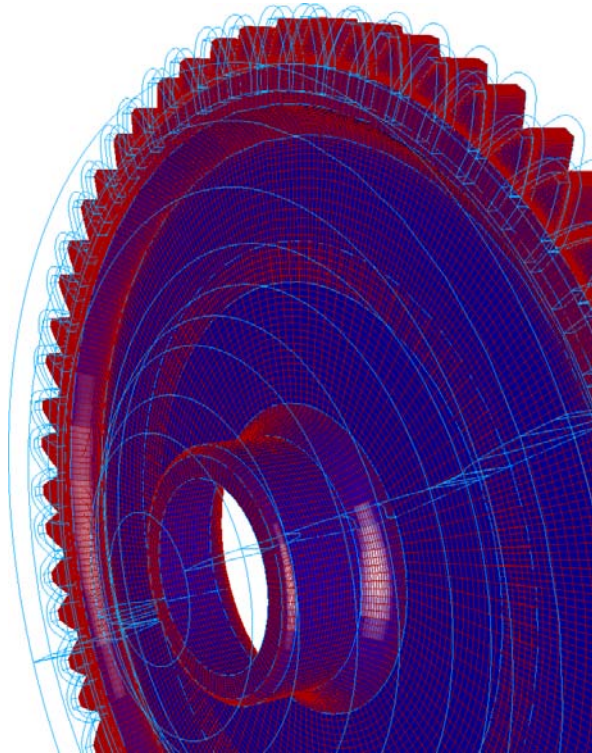
Figure 4.34. Surface topology of the overset mesh used to describe the NASA Glenn 13-inch spur gear.

passage, a strong ejection of this flow near the tooth centerline and radial flow of the near-face streamlines below the base of the teeth.
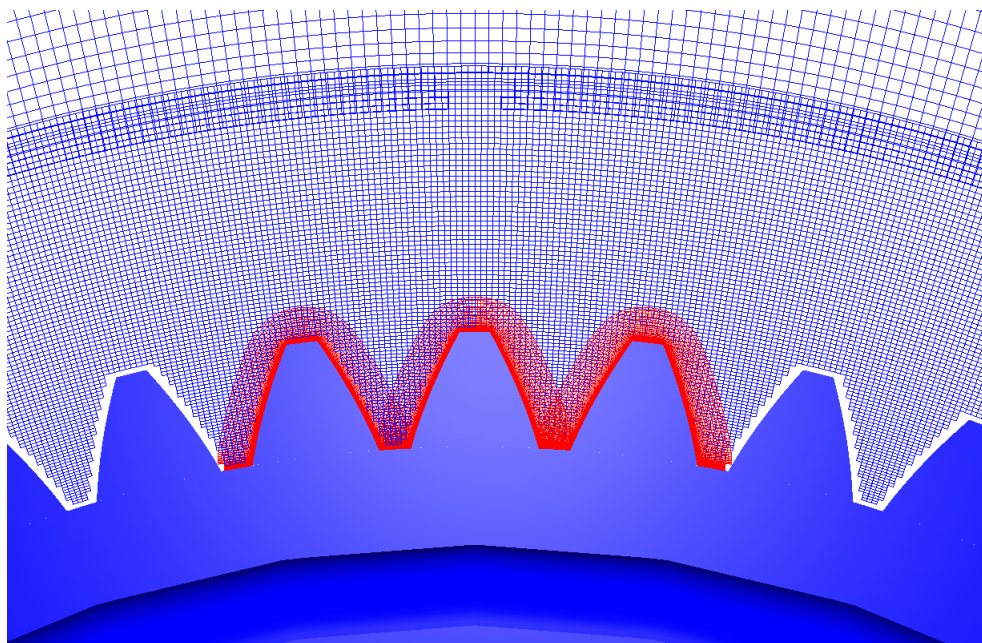
Figure 4.35. Overset mesh topology of the NASA Glenn 13-inch spur gear.
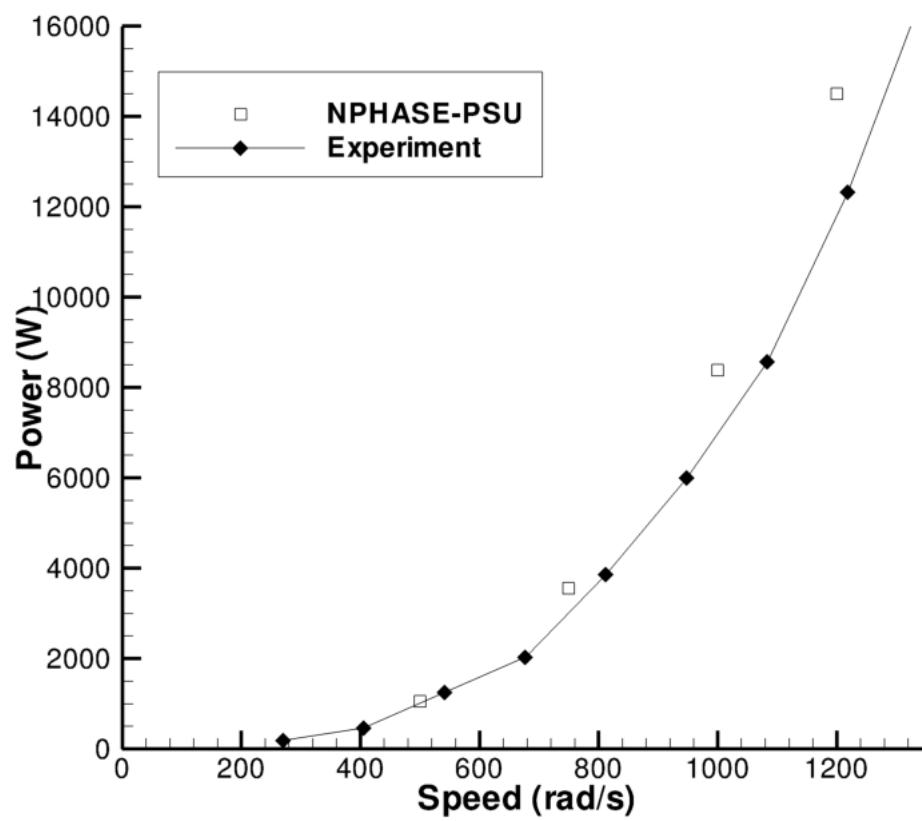
Figure 4.36. NPHASE-PSU results for the unshrouded NASA Glenn 13-inch spur gear.
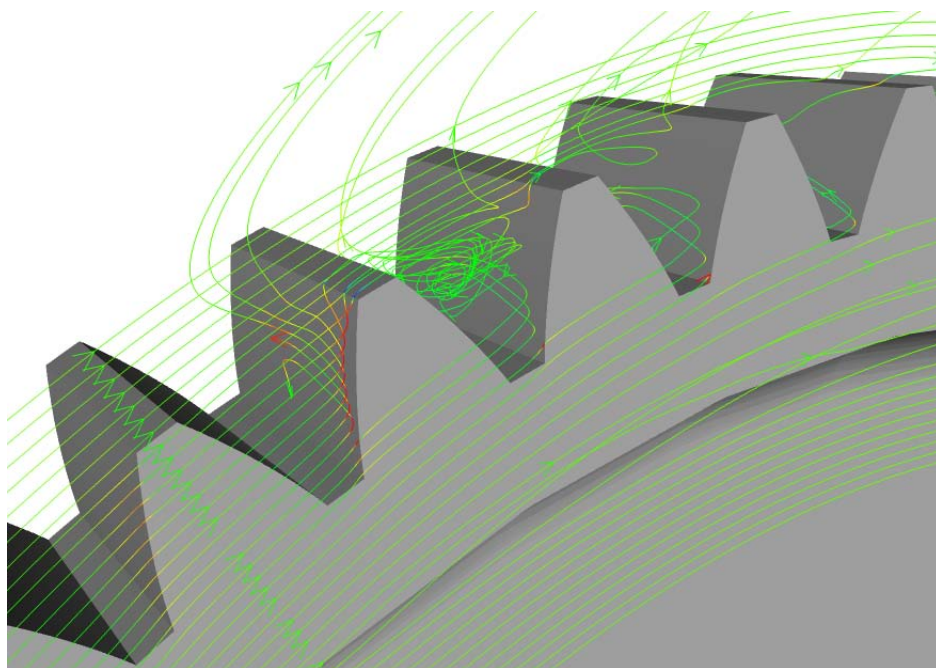
Figure 4.37. Three-dimensional relative frame streamlines for the unshrouded NASA Glenn 13-inch spur gear at 1000 rad/s.

4.3.2 OVER-REL Results

Grids were developed for the 13-inch pitch diameter spur gear configuration using similar topologies as the Diab cases (Section 4.1). Grids were created for all four of the shroud configurations listed in Table 4.3.

Figure 4.38 shows comparisons of the NASA Glenn experimental data and the OVER-REL predictions for the four shroud configurations. The data shows the same trends as the idealized Diab gear CFD studies reported in Section 4.1. Specifically, the Large-Axial-Large-Radial shrouding exhibits the highest loss levels, and the Small-Axial-Small-Radial shrouding exhibits the lowest loss levels. The benefit realized by reducing both clearances is somewhat more substantial than for the Diab case. The CFD results are seen here to provide fairly good agreement with the measured values. An interesting observation in the CFD results is that the Large-Axial-Small-Radial and Small-Axial-Large-Radial results are nearly identical along the entire speed line.

The qualitative correspondence between the Glenn and idealized Diab cases presented earlier, suggests that the same physical loss mechanisms are acting on both of them. Figure 4.39 shows a view of the predicted relative streamlines colored by pressure for the Large-Axial-Large-Radial shroud case at 700 rad/s. This image exhibits several of the features observed for the idealized case including diversion of the near face flow into the tooth passage and impingement upon the leading surface, strong axial secondary vorticity in the tooth passage, strong ejection of this flow near the tooth centerline and radial flow of the near-face streamlines below the base of the teeth.

4.4 Design Studies

It was demonstrated previously (Section 4.1) that axial and radial shrouding can reduce windage losses. Some of the physics of these loss reduction schemes were studied there. Despite the experimentally and computationally observed differences in loss magnitudes between unshrouded and various shrouded configurations, in all cases a significant component of the torques associated with spin down arose from impingement onto the leading surface of the high velocity relative-frame flow
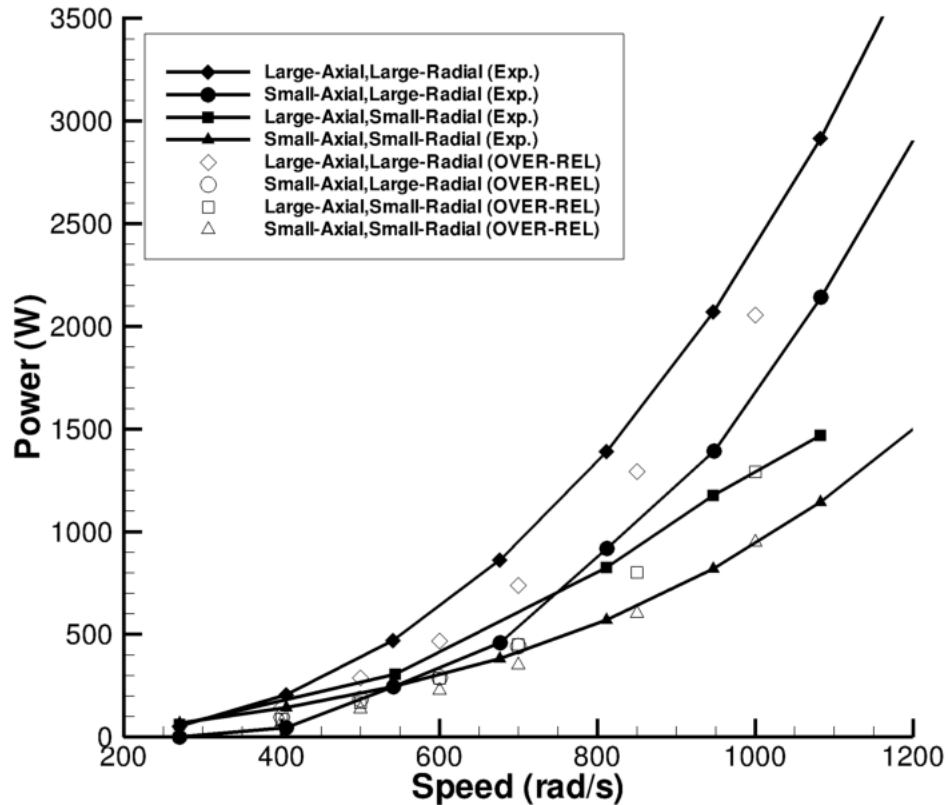
Figure 4.38. Experimental and CFD results for the 13-inch pitch diameter NASA spur gear

drawn into the tooth passage. Accordingly, in this section we return to the geometrically idealized Diab Gear 1 configuration, and experiment numerically with four proposed tooth geometry modifications aimed at mitigating this impingement and attendant spin down torque. Figure 4.40 shows an oblique view of the four alternative geometries considered: 1) leading surface tooth-edge rounding, 2) leading+trailing surface tooth-edge rounding, 3) double slots on the top of the teeth and, 4) trailing surface ramp.

Figure 4.41 shows a comparison of these four simulations in the baseline Large-Axial-Large-Radial case. The leading surface rounding and double slot geometries return nearly identical windage loss. The leading+trailing surface rounding returns
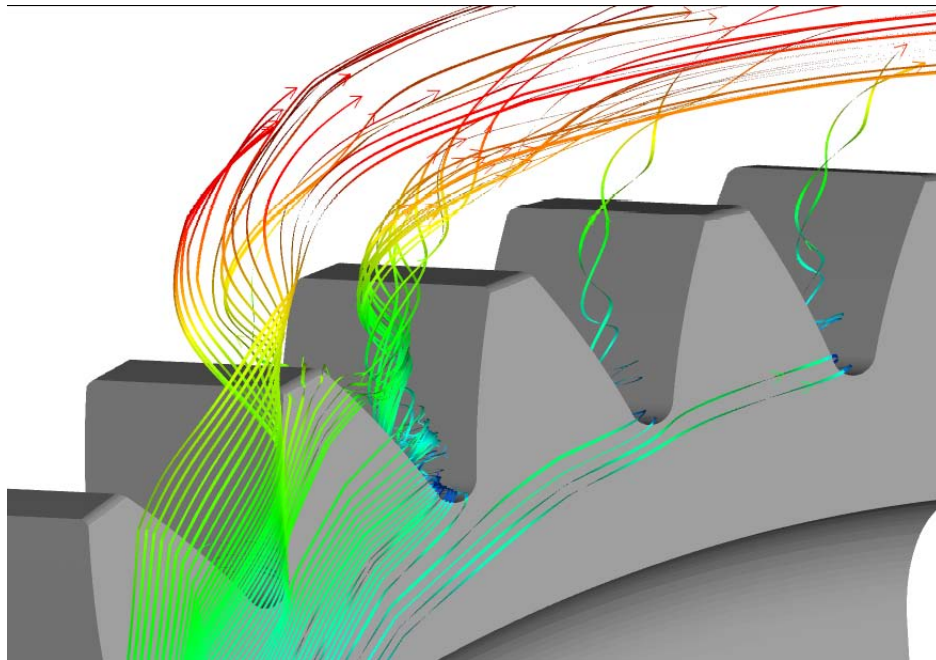
Figure 4.39. Three dimensional relative frame streamlines colored by static pressure for the 13-inch pitch diameter NASA spur gear, Large-Axial-Large-Radial shroud, 700 rad/s.

somewhat higher loss. However, the net loss obtained using the trailing surface ramp is approximately 30% lower than the baseline configuration. The torque per unit width for the five geometries is plotted in Figure 4.42. There it can be seen that the ramp configuration exhibits much smaller torques within the tooth channel and this clearly results in the reduced integrated loss for the entire gear.

Figures 4.43 - 4.47 are presented to further elucidate the physics involved in these numerical studies. In each of these figures, predicted surface pressure coefficients contours are plotted along with selected surface skin friction lines. The baseline and two rounded geometries exhibit largely the same qualitative flow features, with the rounded cases "smearing" the leading face impingement and trailing face detachment gradients. The tooth slots were conceived to "flush" the peak axial vorticity/low pressure regions of incoming relative flow with higher velocity thereby reducing the axial pressure gradient and thereby diverting the high relative velocity near-face flow into the passage. This appears here to not have achieved the desired result. The trailing surface ramp geometry did have a signif-
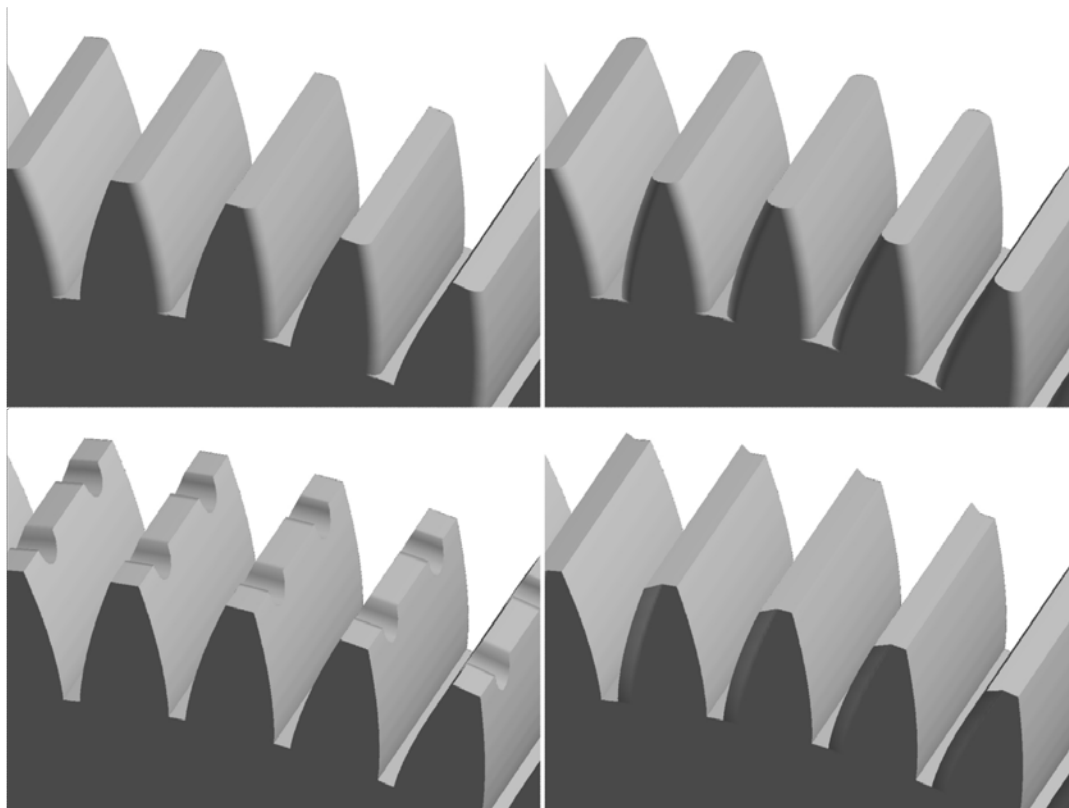
Figure 4.40. Tooth geometry alternatives: leading surface rounding (top left), leading+trailing surface rounding (top right), slotted (bottom left), and trailing surface ramp (bottom right).

icant impact on the aerodynamics. Specifically, the relative flow near the face is turned away from the gear. This turning induces a local pressure rise on the ramp which contributes to spin-down torque. However, this flow has been diverted away from the tooth enough that subsequent diversion of this flow into the tooth passage has been virtually eliminated, resulting in almost no pressure rise on the leading surface. This gives rise to the much smaller torques as shown in Figure 4.42. So the improved net performance of the ramp configuration observed in Figure 4.41 is clearly due to the reduced integrated tooth passage torque more than offsetting the increased torque associated with the ramp turning itself. Finally, Figure 4.48 shows the integrated radial velocity versus speed for the baseline shrouded and unshrouded configurations and the ramp case.
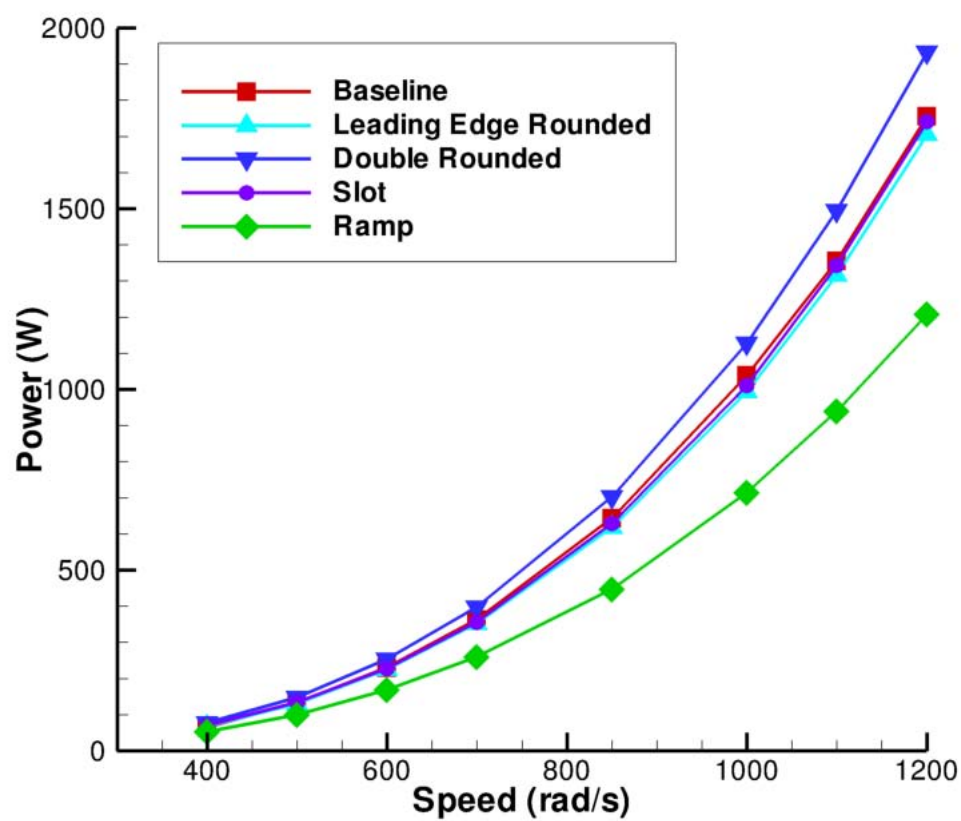
Figure 4.41. Windage loss predictions for the baseline tooth geometry (Diab Gear 1 with Large-Axial-Large-Radial shrouds) and four geometric alternatives.
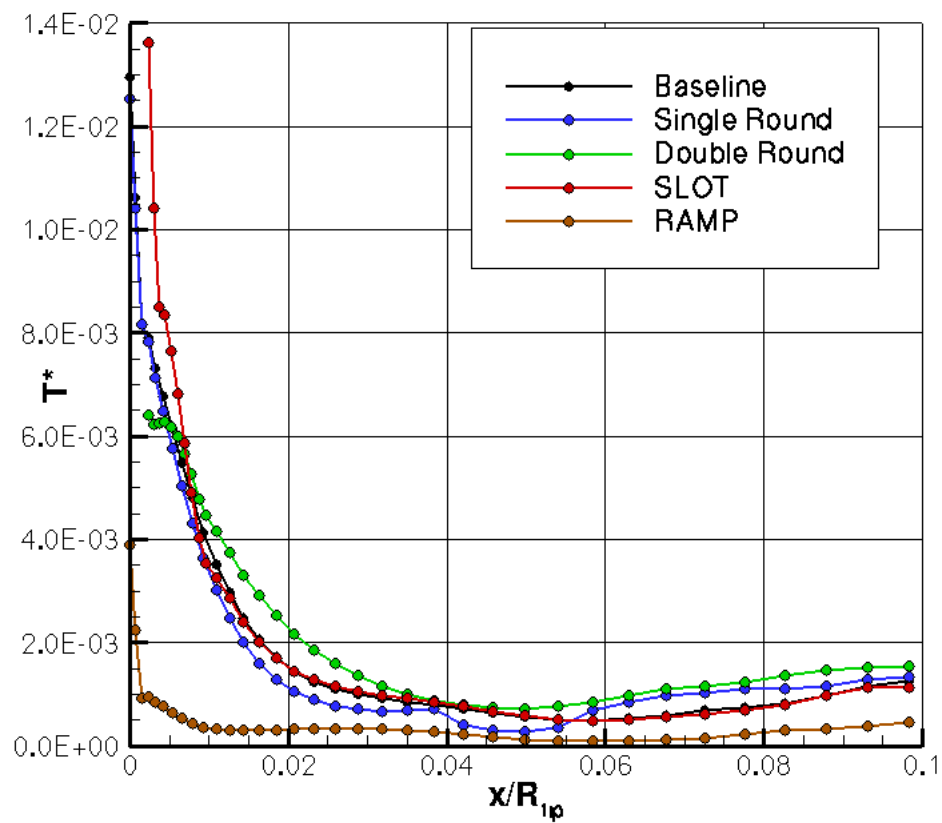
Figure 4.42. Torque per unit width predictions for the baseline tooth geometry (Diab Gear 1 with Large-Axial-Large-Radial shrouds) and four geometric alternatives at 850 rad/s.
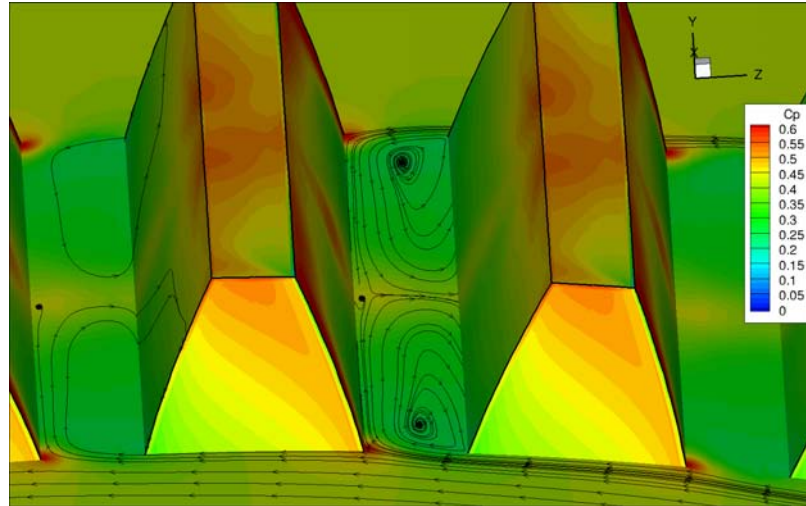
Figure 4.43. Predicted surface pressure coefficient and skin friction lines for baseline tooth geometry.
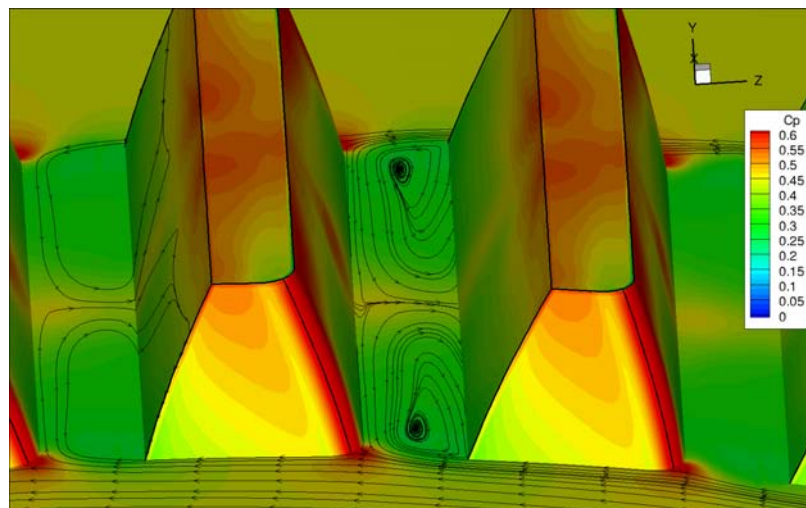
Figure 4.44. Predicted surface pressure coefficient and skin friction lines for tooth geometry alternative: leading surface rounding.
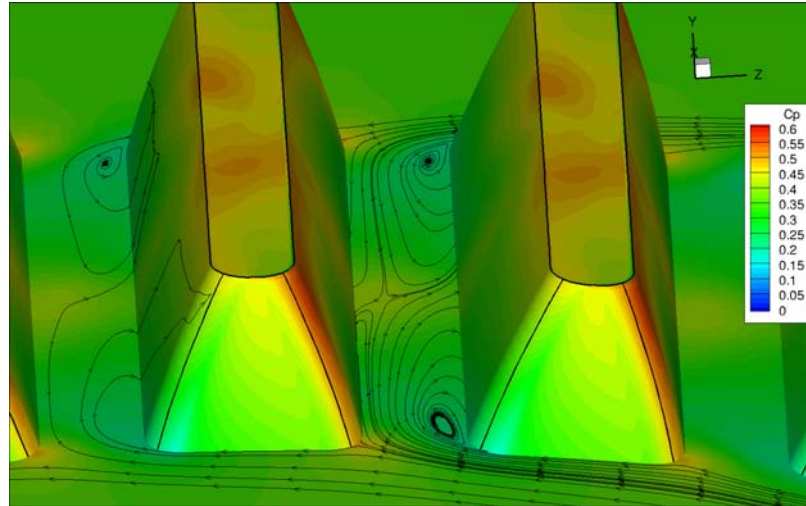
Figure 4.45. Predicted surface pressure coefficient and skin friction lines for tooth geometry alternative: leading+trailing surface rounding.
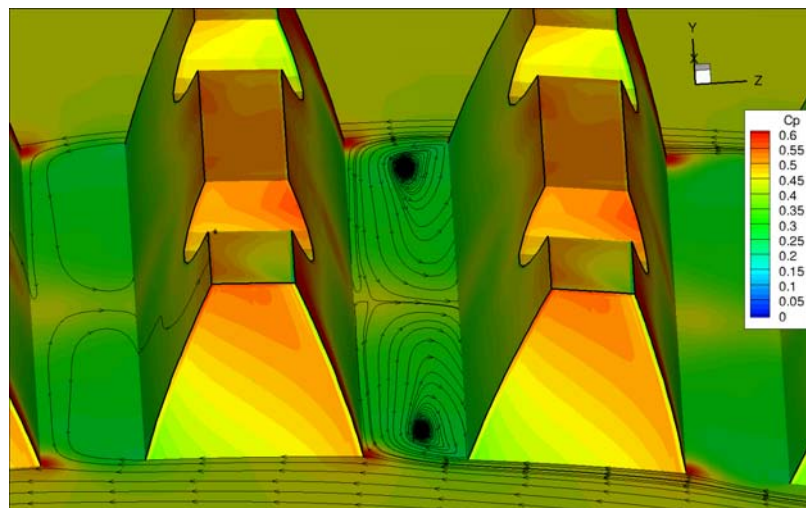
Figure 4.46. Predicted surface pressure coefficient and skin friction lines for tooth geometry alternative: tooth slot.
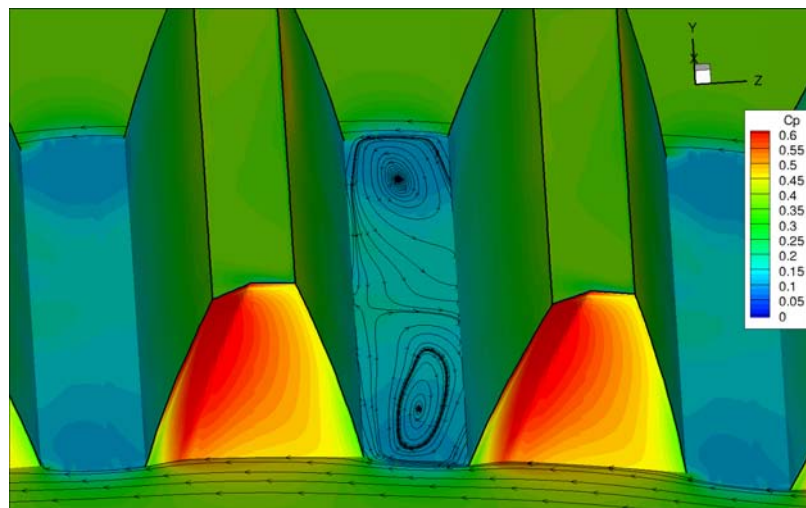
Figure 4.47. Predicted surface pressure coefficient and skin friction lines for tooth geometry alternative: trailing surface ramp.
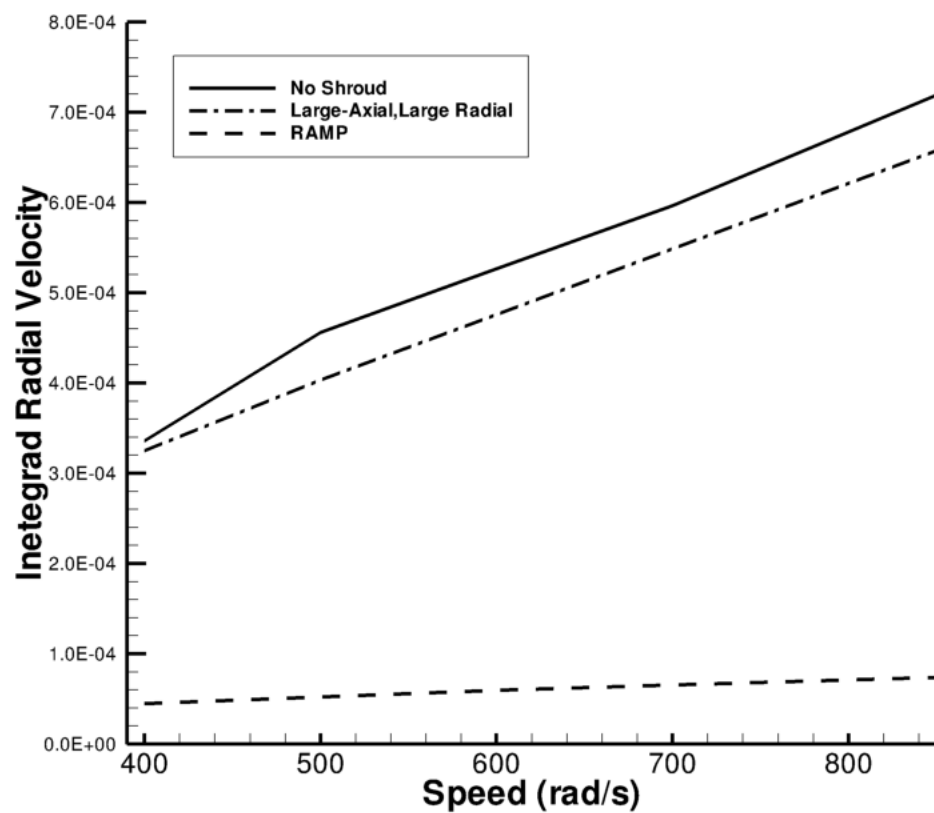
Figure 4.48. Comparison of integrated radial mass flow from gear teeth between the unshrouded, the baseline Large-Axial-Large-Radial shroud case, and the Large-Axial-Large-Radial case with tooth trailing surface ramps.

4.5 Bell Helical Gear Analysis

Bell Helicopter has recently developed their own gear windage test facility to test shroud design configurations for a helical gear train. The facility consists of two helical gears in mesh. Table 4.4 lists the properties of the gears under test. The test facility is designed to parametrize the effects of gear geometry, shroud geometries and sizes, different lubrication system configurations, system pressures and temperatures, and gear meshing on windage loss.

Table 4.4. Bell Helical Gear Data

	Input Gear	Bull Gear
Number of teeth	51	139
Pitch Diameter, mm (in.)	154.7 (6.09)	431 (16.97)
Helix Angle, degree	12	
Module (Diametral Pitch), mm (1/in.)	3.033 (8.375)	
Face Width, mm (in.)	67.2 (2.625)	
Reduction Ratio	2.7255:1	

Grids were developed for the helical gears using similar grid topologies as the Diab (Section 4.1) and NASA Glenn (Section 4.3.2) studies. Figures 4.49 - 4.52 provide views of the surface grid topology at the gear teeth and the overall grid topology. One shrouded and one unshrouded configuration was tested for each gear. In the shrouded cases, both cases had an axial clearance of 2 mm at the gear teeth. The smaller 51-tooth (51T) drive gear had a 1 mm radial clearance and the 139-tooth (139T) gear had a 1.5 mm radial clearance. The geometry and dimensions of the shroud were provided by Bell Helicopter. Table 4.5 lists the total number of grid cells used in each case. Cases were run in the manner described in Section 3.2.

Table 4.5. Total Number of Cells (in millions) of Bell Helical Gear Grids

Gear	Shrouded	No Shroud
51T	2.81	5.62
139T	3.85	6.20
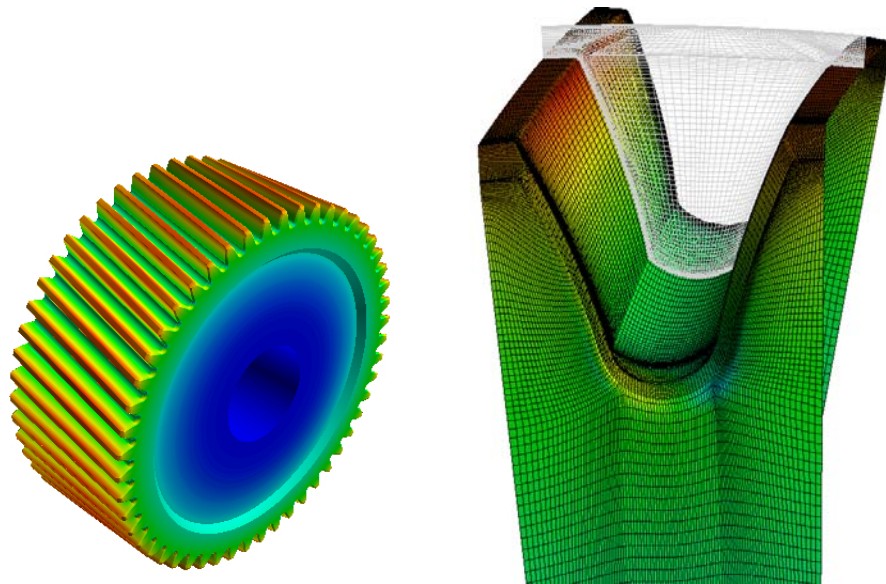
Figure 4.49. Bell 51-tooth helical gear and surface mesh.

Figures 4.53 and 4.54 show the predicted power loss as a function of speed for the 51-tooth and 139-tooth gears, respectively. Both figures clearly show the effect of shrouds in reducing windage losses. Figures 4.55 and 4.56 show the predicted viscous and pressure loss budgets for the two cases. Shrouding has a profound influence on the pressure losses. Pressure losses are greatly reduced and they are no longer dominant over viscous losses. Figure 4.57 compares the total windage losses of all four cases together. In this figure, pitch-line velocity replaces rotation speed on the x-axis. Figure 4.58 plots power loss ratio between the large and small helical gears as a function of speed. In the unshrouded configuration, the power loss ratio remains fairly constant with speed. However, in the shrouded case, power loss ratio decreases as speed increases. This is probably due to the fact that the losses experienced by the small gear are quite small at low speed.

Figures 4.59 and 4.60 present a 3-D visualization of the flow through the gear teeth of the smaller Bell gear. The streamlines colored in blue represent the flow that enters the teeth from the leading edge of the gear. The red is for the flow from the trailing edge. The surface of the gear is colored by the static pressure coefficient. Figures 4.61 and 4.62 do the same for the larger gear. It is observed in the unshrouded cases (Figures 4.60 and 4.62), that the flow from the leading edge
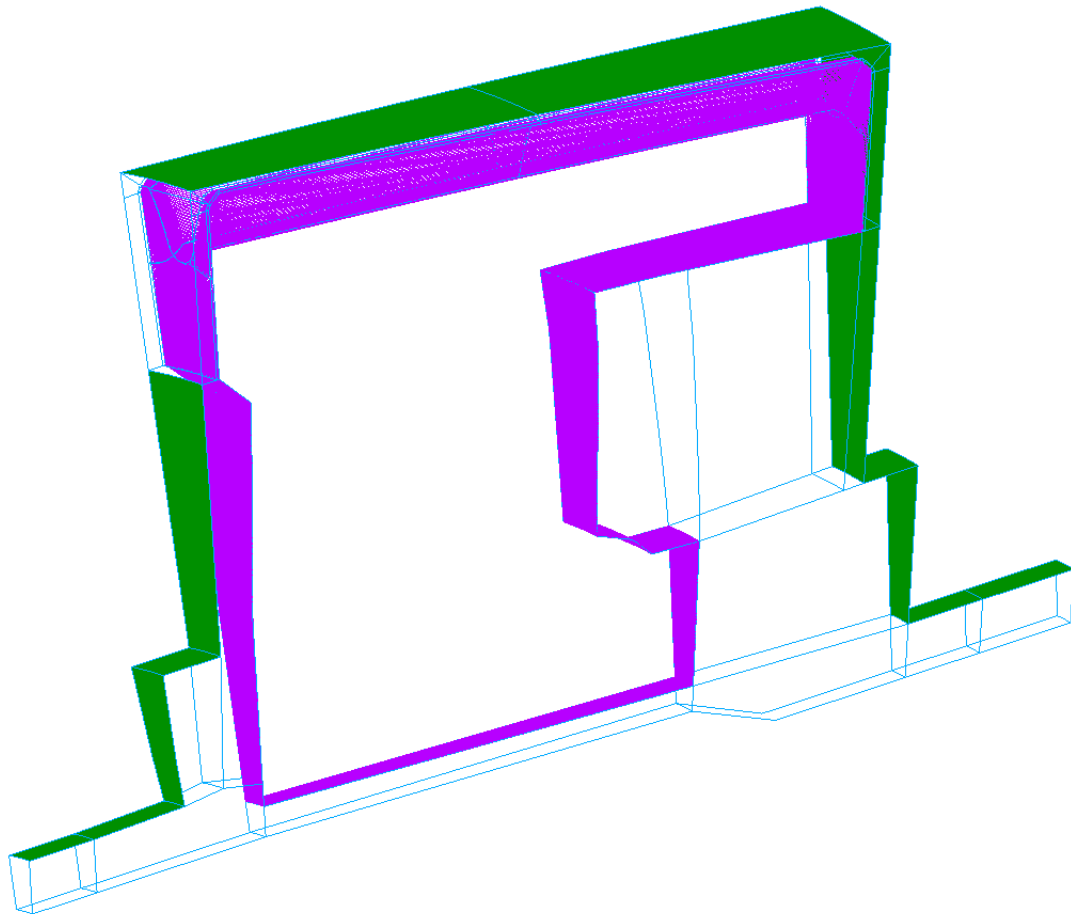
Figure 4.50. Shrouded Bell 51-tooth helical gear grid domain.

dominates. Any flow that enters from the opposite end, is quickly expelled over the teeth. A very large stagnation region on the leading edge side is also clearly visible in both cases. With the addition of shrouding (Figures 4.59 and 4.61), there is still a strong flow from the leading side, but the flow from the trailing side is able to penetrate deeper into the tooth well before being turned away. These different flow patterns also explain the difference of observations made by Dawson [4] and Houjoh et al. [23] of the flow through helical gear teeth. The helical gears in Houjoh et al. [23] were held in a moderately sized enclosure. Also the large stagnation region at the leading edge has disappeared, replaced with
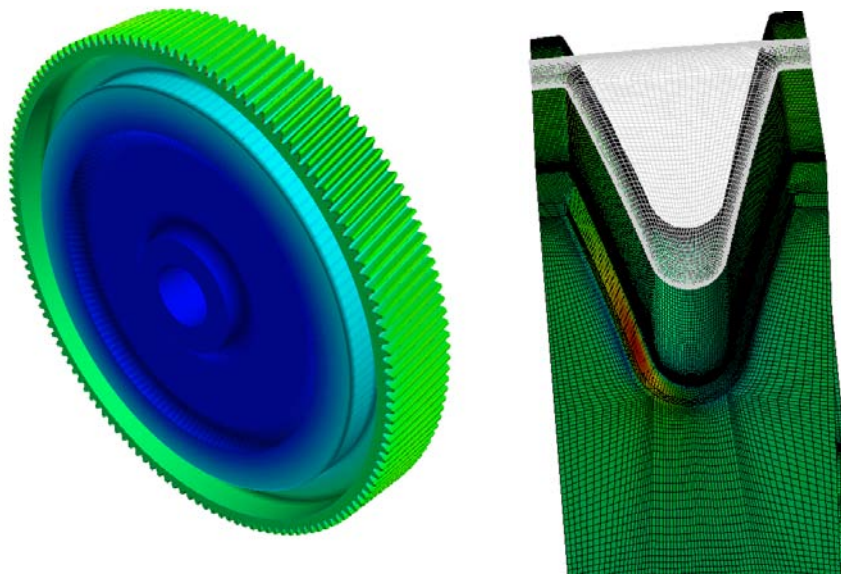
Figure 4.51. Bell 139-tooth helical gear and surface mesh.

two small stagnation regions close the base of the rounded edges. It should be noted that Figure 4.59 can be misleading. It appears that there is a high pressure stagnation region on the leading tooth face along the entire width of the gear that should yield higher torque values. However, this is countered by the high pressure region on the opposite trailing tooth face, providing for a lower ΔC_p between faces. It was explained previously in Section 3.3 that the net axial torque due to pressure effects was due to the difference between leading and trailing surface pressure coefficients.
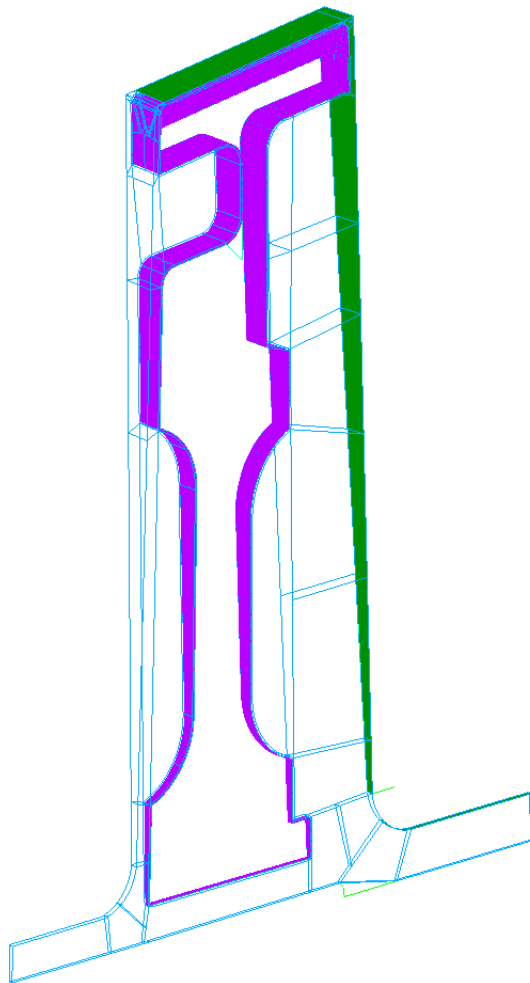
Figure 4.52. Shrouded Bell 139-tooth helical gear grid domain.
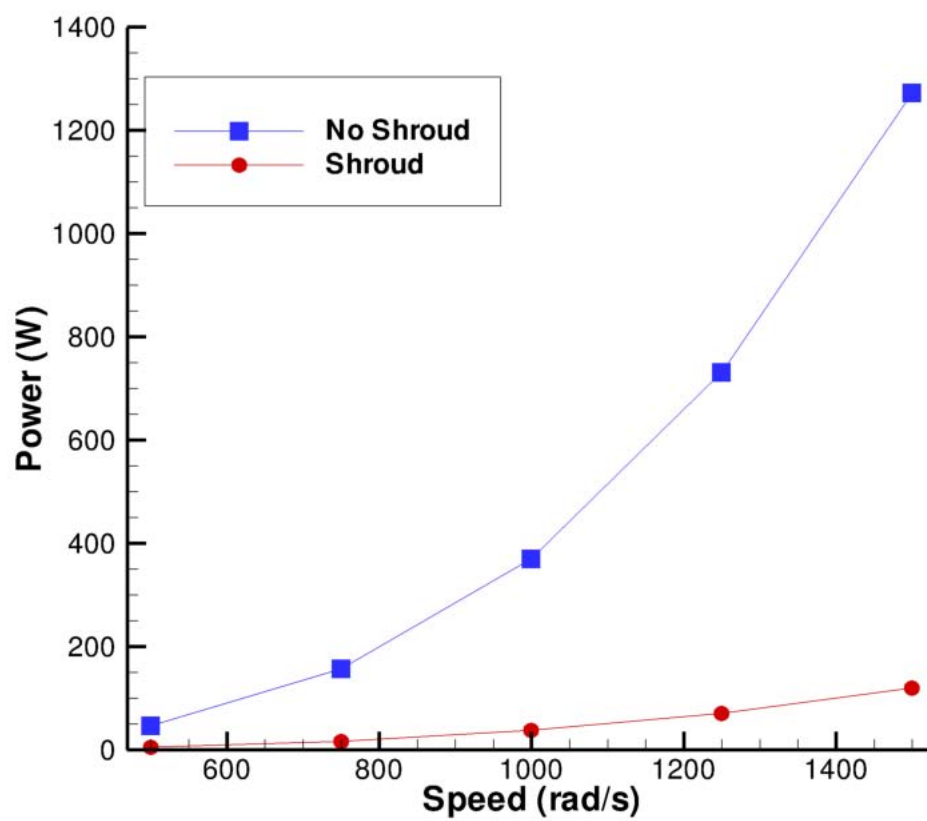
Figure 4.53. CFD predictions of windage power loss vs. speed for Bell 51-tooth helical gear.
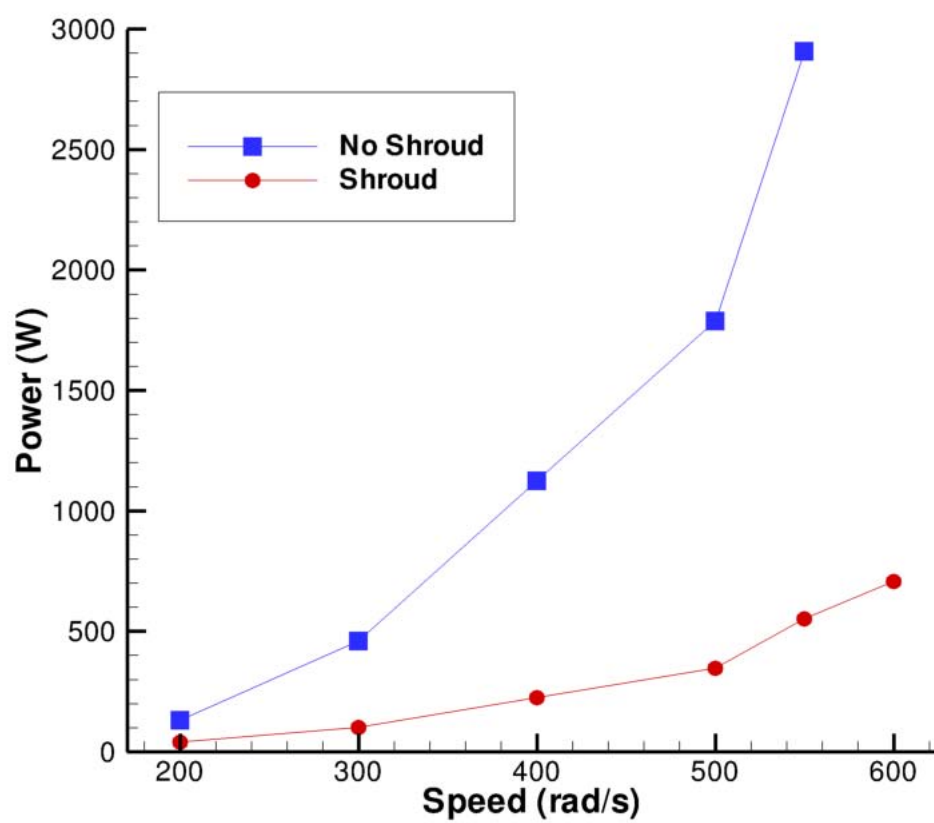
Figure 4.54. CFD predictions of windage power loss vs. speed for Bell 139-tooth helical gear.
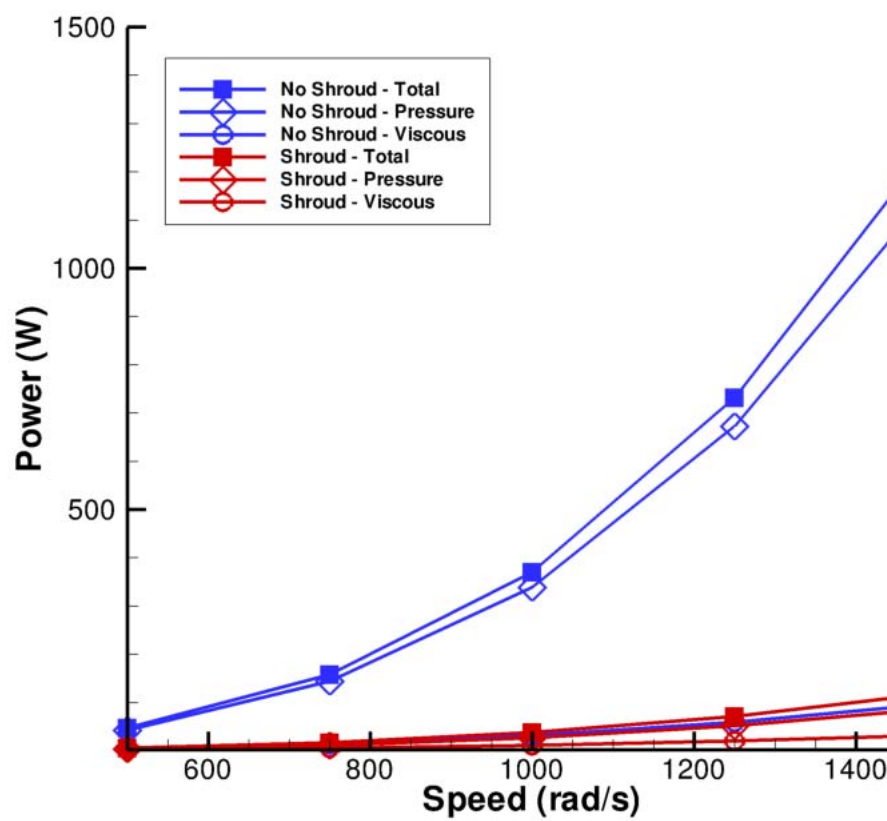
Figure 4.55. Breakdown of pressure and viscous windage power losses for Bell 51-tooth helical gear.
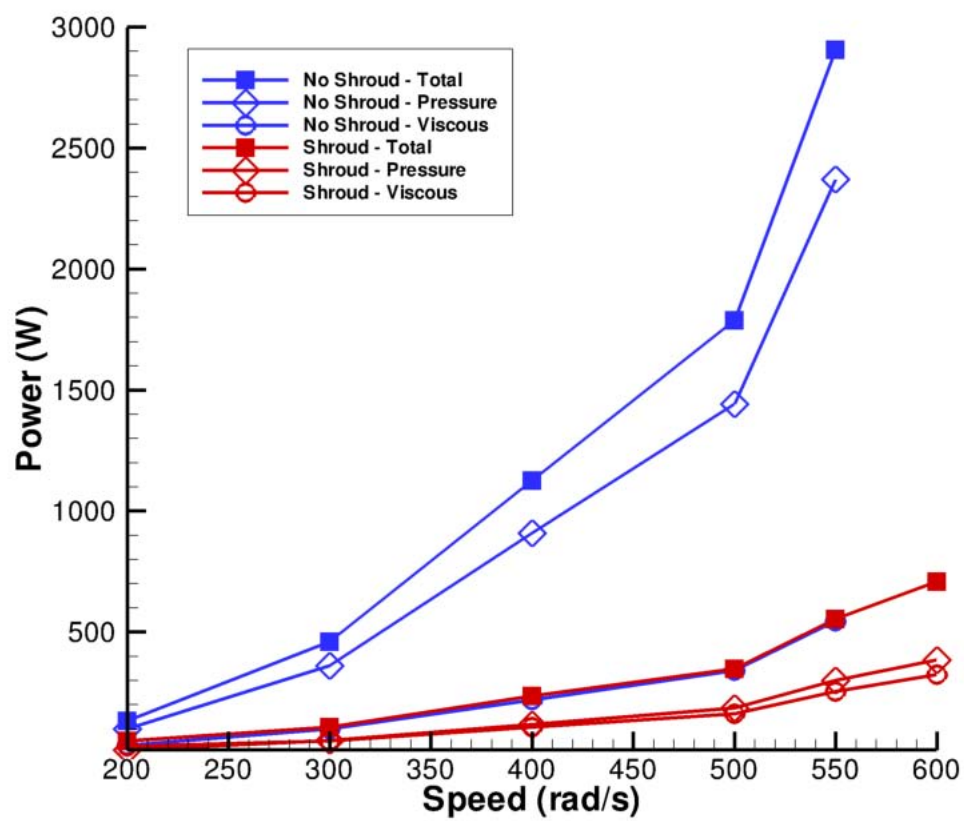
Figure 4.56. Breakdown of pressure and viscous windage power losses for Bell 139-tooth helical gear.
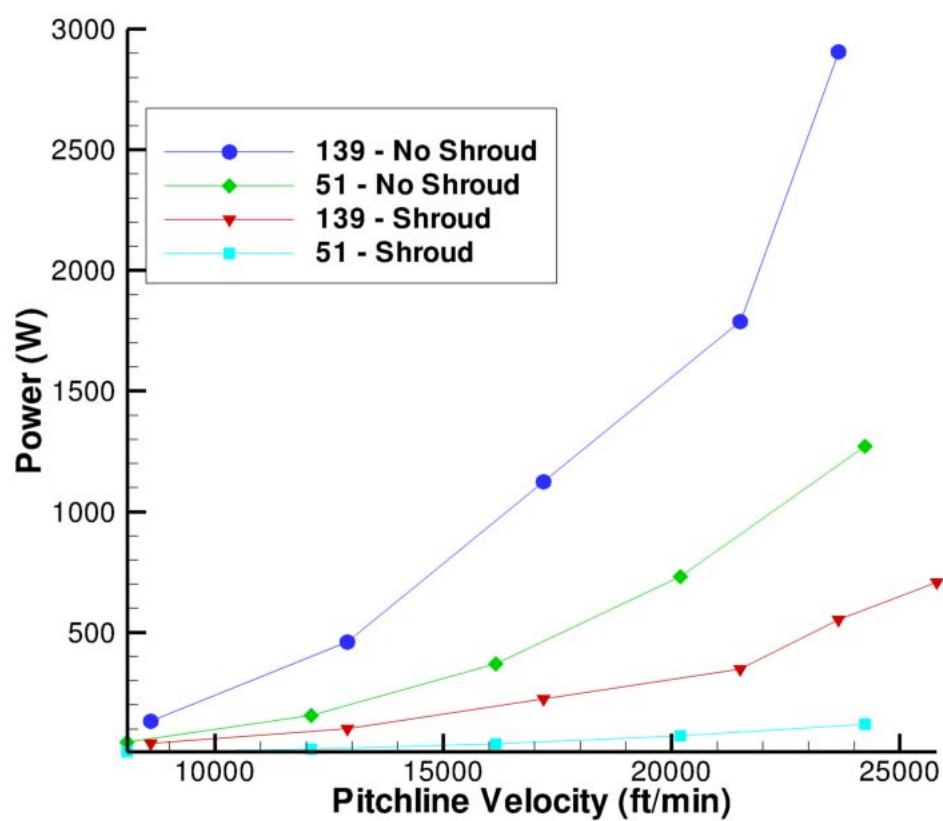
Figure 4.57. CFD predictions of windage power loss vs. pitchline velocity for Bell helical gears.
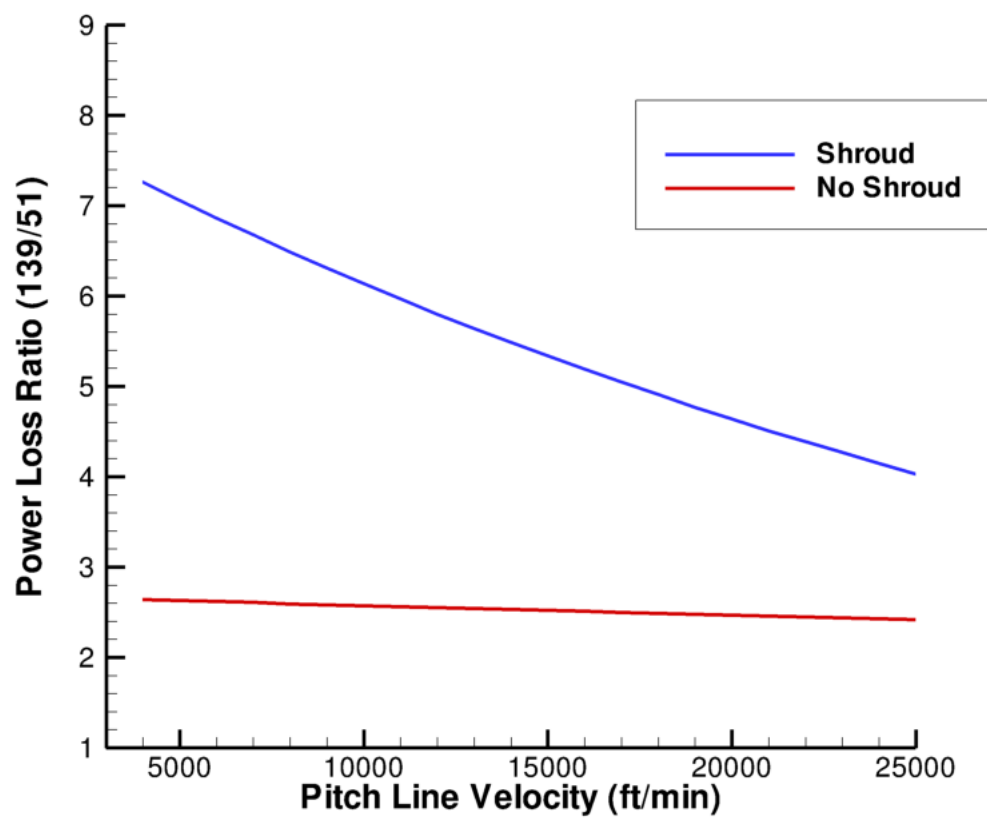
Figure 4.58. Predicted power loss ratio vs. pitchline velocity between the 139-tooth and 51-tooth helical gears.
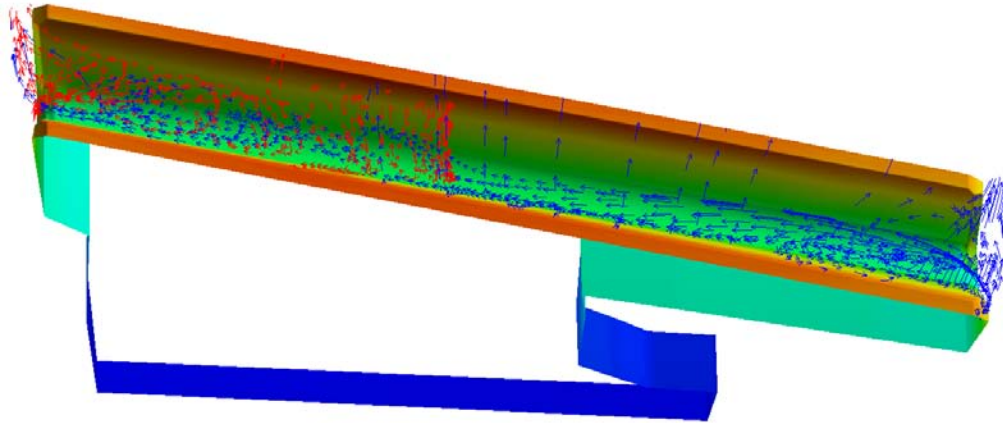
Figure 4.59. Three-dimensional relative frame streamlines colored entrance location for shrouded Bell 51-tooth gear at 1500 rad/s.
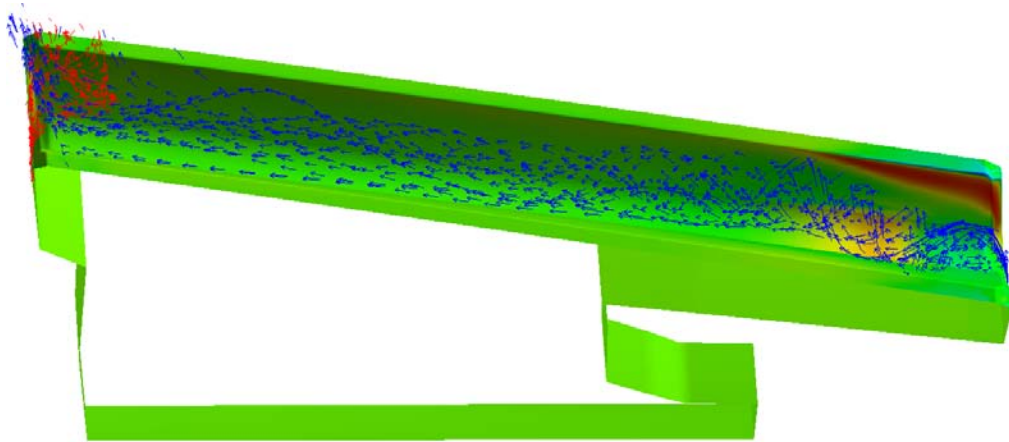
Figure 4.60. Three-dimensional relative frame streamlines colored entrance location for unshrouded Bell 51-tooth gear at 1500 rad/s.
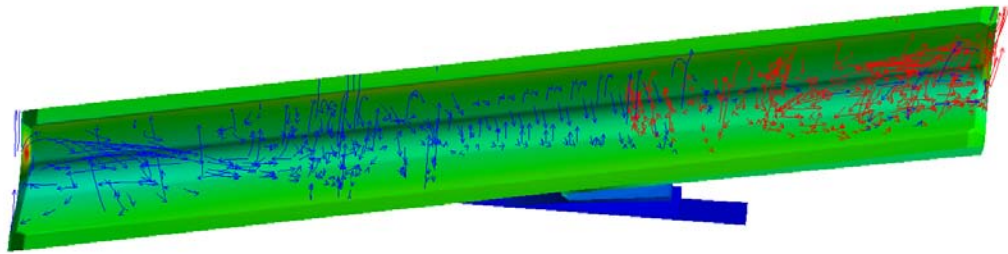
Figure 4.61. Three-dimensional relative frame streamlines colored entrance location for shrouded Bell 139-tooth gear at 550 rad/s.
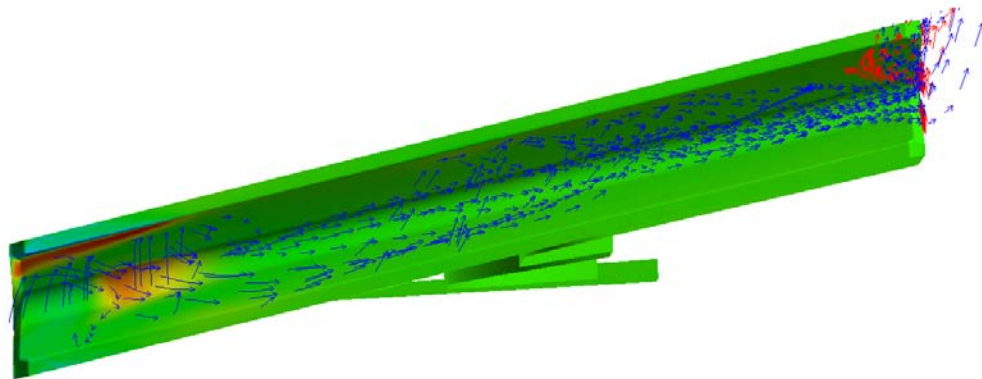
Figure 4.62. Three-dimensional relative frame streamlines colored entrance location for unshrouded Bell 139-tooth gear at 550 rad/s.

4.5.1   Design Alternatives

Like the design space exploration that was performed on the Large-Axial-Large-Radial shrouded Diab Gear 1 (Section 4.4), a similar exploration was performed on the unshrouded 139-tooth Bell gear. Analysis of the unshrouded gears showed a strong axial flow from the leading edge to the trailing edge of the gear teeth. Therefore, two modifications were tested to reduce this axial flow. The first modification was to simply block the leading edge inlet with a wall, similar to that of Dawson [4]. This was accomplished by taking advantage of grid block boundaries located near the leading edge of the teeth. The original block-to-block boundaries were simply changed to inviscid wall boundaries. A no-slip wall boundary condition would have required extensive modifications to the grid blocks to meet y^+ wall spacing requirements. The inviscid wall is shown in Figure 4.63 shaded in grey. The second modification was based on the tooth ramp design study presented in Section 4.4. However, unlike the spur gear study, the ramp was only added to the leading edge side. Figure 4.64 illustrates the tooth ramp geometry.
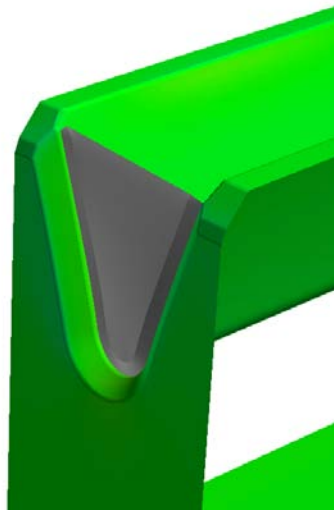
Figure 4.63. Bell 139-tooth helical gear with blocked leading edge.

Both cases were only run at a speed of 550 rad/s, which is the maximum operational speed for this gear. A 30% decrease in windage losses was achieved with both configurations as shown in Figure 4.65. Figures 4.66 and 4.67 provide
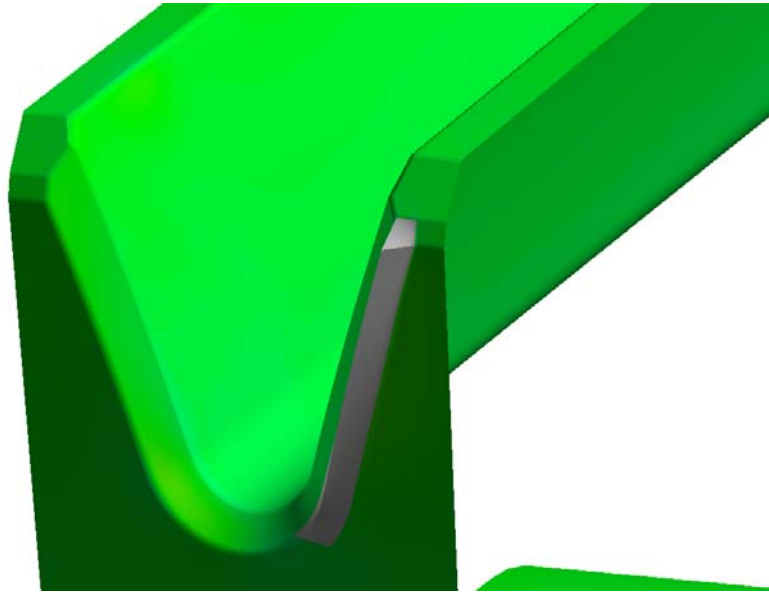
Figure 4.64. Bell 139-tooth helical gear with leading edge spoiler.

a 3-D view of the flow through the gear teeth. In both cases, the modifications either block or divert the flow away from the inlet region. Most of the flow through the teeth comes from the trailing edge side (streamlines colored in red) of the gear. The streamlines colored in blue represent flow from the leading edge. It should be noted that streamlines in Figure 4.66 that appear to go through the inviscid wall are an artifact of the post-processing software. Comparing these results with the those from the original unmodified case (Figure 4.62), it can be seen that the stagnation region on edge of the gear tooth has also shifted from the leading edge to the trailing edge and is significantly smaller.
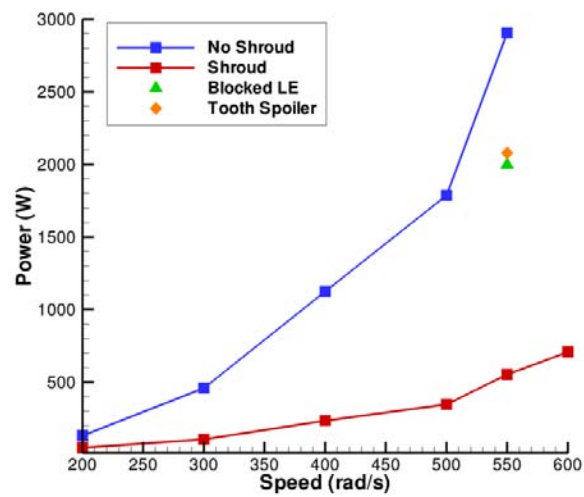
Figure 4.65. CFD predictions of windage power loss for modified Bell helical gears. at 550 rad/s.
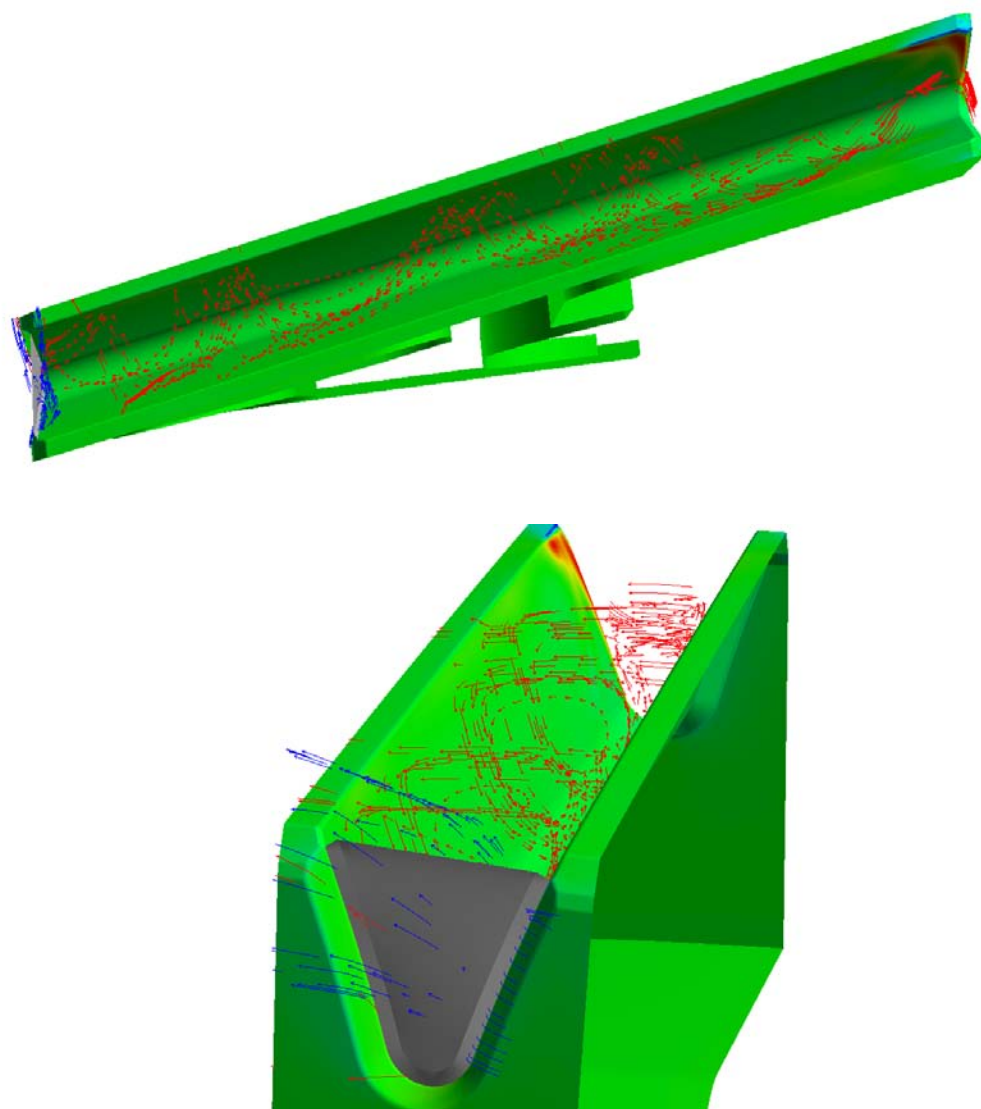
Figure 4.66. Relative frame streamlines of the Bell 139-tooth helical gear with blocked leading edge at 550 rad/s.
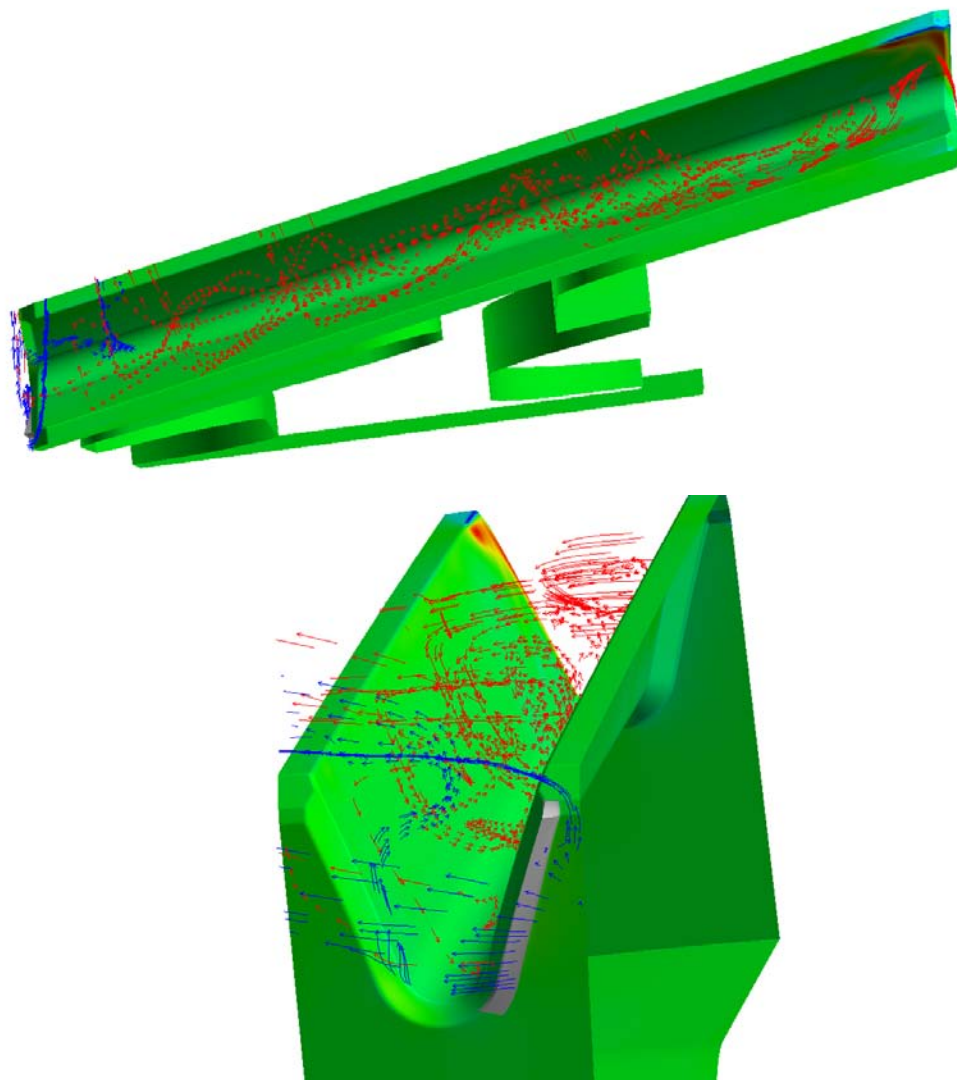
Figure 4.67. Relative frame streamlines of the Bell 139-tooth helical gear with leading edge spoiler at 550 rad/s.

Chapter 5

Conclusions

This dissertation has presented the development and application of a CFD method for gear windage aerodynamics. The goals of this research have been to develop and validate numerical and modeling approaches for these systems, to develop a physical understanding of the aerodynamics of gear windage loss, including the physics of loss mitigation strategies, and to propose and evaluate new approaches for minimizing loss. Absolute and relative frame CFD simulations, overset gridding, multiphase flow analysis, and sub-layer resolved turbulence modeling were brought to bear in achieving these goals. Several spur gear geometries were studied for which experimental data are available. Various shrouding configurations and free-spinning (no shroud) cases were studied. Comparisons were made with experimental data from the open literature, and data recently obtained in the NASA Glenn Research Center Gear Windage Test Facility. The results showed good agreement with experiment. Interrogation of the validative and exploratory CFD results have led, for the first time, to detailed understanding of the physical mechanisms of gear windage loss, and have led to newly proposed mitigation strategies whose effectiveness has been explored computationally.

The following conclusions have resulted from this research and have been presented:

1. Using the CFD method to interrogate the physics of these systems, it was shown, for the first time, that for all configurations studied, the dominant physical mechanism contributing to windage losses is the pressure field asso-

ciated with diversion and impingement of the high speed relative flow on the leading tooth surface.

2. Shrouding mitigates the magnitude of the pressure component of windage losses, but not its dominance in the loss budget.

3. The interrogation of the validative and exploratory CFD results have shown, for the first time, that shrouding reduces windage effects. Shrouds conserve the angular momentum of the flow near the teeth so that the tangential velocity of the flow that enters the gear teeth is much closer to that of the gear. This reduces the work required of the gear to accelerate the flow.

4. The CFD studies have suggested a set of possible geometric tooth modifications to reduce windage loss further. The trailing edge ramp/spoiler appears quite promising and the author hopes this is studied in the NASA Glenn facility.

5. The CFD results show good agreement with open literature data and with the NASA Glenn experiments. Experimental data from the NASA Glenn test facility and and CFD analyses show that axial and radial gear shrouding are effective in significantly reducing gear windage losses both independently and when employed together. The NASA Glenn data also shows very similar trends to the idealized shrouded gear configurations studied computationally.

6. The prediction of viscous losses and turbulence modeling was identified as a shortcoming since power loss was consistently underpredicted for the viscous-drag-only spinning disk cases.

   - Low Reynolds number turbulence modeling (with appropriately sub-layer resolved meshes) exhibited improved performance in predicting viscous losses.

   - Due to the dominance of the pressure losses, high Reynolds number two-equation modeling proved adequate for modeling the Diab spur gear suite.

- The budgets of viscous and pressure components of the windage torque suggest that viscous effects will become much more important for gears with pitch-line speeds approaching twice that investigated here.

- Viscous losses are reduced by shrouding as well, but are a small component of the total loss so this effect is not important.

- Small axial clearances were observed computationally to increase viscous losses compared to larger shroud clearances, suggesting that this effect could become important at higher speeds.

7. Overset meshing is and will continue to be a critical enabler in this effort. The capability has been established and demonstrated here and will become integral in further studies where the isolated gear assumption will not be relevant.

8. CFD analysis of the helical gears showed qualitative agreement with previous studies. The flow through the teeth was mostly axial from the leading edge to the trailing edge in the unshrouded configuration. When the gear was enclosed, the dominance of the leading edge flow was reduced. The CFD results also showed that shrouds are effective in significantly reducing gear windage losses for helical gears. CFD studies also suggested two promising geometric modifications that could be made to the leading edge of the gear teeth to provide further reductions in windage loss. The author hopes experimental data will become available in the future to further validate these results.

This dissertation has focused on the air-only effects of gear windage on isolated gears. However, gears do not operate in either an air-only environment or alone. The following items are areas of possible future work:

1. Apply multiphase CFD techniques to explore the physics of the air and oil atmosphere on gear windage and the effectiveness of shrouding.

2. Explore the effects of meshing gears on windage effects and determine the computational needs and requirements to provide design guidance.

3. Evolve design guidance to mitigate windage losses through further CFD studies.

4. Further validate the CFD methodology as more data becomes available from NASA Glenn.

Gear Windage Estimate Program

A.1 Program Description

The python script GWLestimate.py generates the windage power loss predictions ueing four different models: the Anderson and Loewenthal model[20], Dawson's 1984 model[4], Dawson's updated 1988 model[38], and the fluid flow model of Diab et al.[6]. The code is currently configured for the NASA Glenn 13-inch gear presented in Section 4.3.

A.2 GWLestimate.py

```python
#!/usr/bin/env python
# GWLestimate.py


import re, sys, math, os


#Gear Variables
pitchradius = 0.1651        # meters
facewidth = 0.0284988       # meters
facewidth2 = 1000*facewidth # mm
baseradius = 149.6314       # mm
basediameter = 2*baseradius #mm
basediameter2 = basediameter/1000 # meters
```

```python
module = 6.35      # mm
teeth = 52
#Operating Conditions
muI = 1.72e-5       # kg/(m*s)
mu = muI*1000      # centipoise
rho = 1.225     # kg/m^3
nu = muI/rho         # m^2/s
#mu = 0.015
speed = 50  # rad/s
maxspeed = 1200 # rad/s


file=open("glenn13.dat","w")


#Useful Constants
radpstorpm = (30/math.pi)  # radians per second to rev. per minute



def computeDawson(rpm,basediamter,facewidth,module):
    power = pow(rpm,2.9)*(0.16*pow(basediameter,3.9)+
     pow(basediameter,2.9)*pow(facewidth,0.75)*
     pow(module,1.15))*1e-20*1000
    #print rpm, power
    return power


def computeDawsonTwo(rpm,basediamter2, rho, nu):
    cprime = 4 # approx. for Glenn 13
    power = 1.12e-8*cprime*rho*pow(rpm, 2.85)*
     pow(basediameter2,4.7)*pow(nu,0.15)*1000
    #print rpm, power
    return power


def computeAandL(rpm, pitchradius, mu, facewidth):
    #Constants
```

```python
    C1 = 2.82e-7 #S.I.
    C2 = 0.019 #S.I.
    C3 = 0.028*mu + C2
    power = C1*(1+2.3*(facewidth/pitchradius))*pow(rpm,2.8)*
     pow(pitchradius,4.6)*pow(C3,.2)*1000
    #print speed, power
    return power


def computeDiabFF(speed, teeth, pitchradius, facewidth, rho, muI):
    # Constants
    n1 = 1.293
    m1 = 0.5
    n2 = 0.074
    m2 = 0.2
    V = speed * pitchradius
    L = 2*math.pi*pitchradius
    Re = rho*V*L/muI
    Restar = 300000.
    Rprime = (muI*Restar)/(rho*speed)
    Rstar = pow(Rprime,0.5)
    # Face
    Cf1 = (2*n1*math.pi/(5-2*m1))*(1/pow(Restar,m1))*
     pow((Rstar/pitchradius),5)
    Cf2 = (2*n2*math.pi/(5-2*m2))*( (1/(pow(Re,m2))) -
     (1/pow(Restar,m2))*pow((Rstar/pitchradius),5) )
    # Teeth
    sigma = math.pi/teeth
    Xa = 0  # profile shift coefficient, assume no shift for now
    Cl = (teeth/4.)*(facewidth/pitchradius)*
     pow((1.+(2.*(1+Xa)/teeth)),4)*
     (1.-math.cos(sigma))*pow((1.+math.cos(sigma)),3)
    # Total
    Ct = Cf1 + Cf2 + Cl
```

```
        power = 0.5 * Ct * rho * pow(speed,3) * pow(pitchradius, 5)
        return power

while speed < maxspeed+1:

    rpm = speed*radpstorpm

    power1 = computeAandL(rpm,pitchradius,mu,facewidth)

    power2 = computeDawson(rpm,basediameter,facewidth2,module)

    power3 = computeDawsonTwo(rpm,basediameter,rho,nu)

    power4 = computeDiabFF(speed,teeth,pitchradius,facewidth,rho,muI)

    file.write("%f \t %f \t %f \t %f \t %f\n"
        %(speed,power1, power2, power3, power4))

    speed = speed + 50


#END SCRIPT
```

Appendix B

Radial Viscous Power Loss Program

B.1 Program Description

The C++ program vprofiler.cpp generates the radial viscous power loss profiles from the solutions provided by OVER-REL. The program reads in a Tecplot formated ascii file called peeled-surfaces.dat. This file is generated by OVER-REL. The file has multiple zones where data is stored at the node points. After successfully reading in the data file, the program performs the following tasks:

1. Compute cell center values of the velocity components u, v, and w, the face area, and the skin friction coefficient C_f.

2. Compute the velocity components in cylindrical coordinate frame where the x-axis is the axis of rotation.

3. Compute the local shear stress and velocity magnitudes

4. Compute tangential shear stress.

5. Compute local tangential viscous force.

6. Compute local viscous torque.

7. Sum all local viscous torques for validation against previously computed OVER-REL results.

8. After validation, output to a text file of area averaged viscous loss versus radius.

B.2 Vprofiler.cpp

```
/*
 * vprofiler.cpp
 *
 *  Created on: Apr 20, 2010
 *      Author: Matthew Hill
 *
 *  HOW TO RUN
 *  ==========
 *
 *  This program is run from the command line in the following
 *  fashion:
 *  vprofiler filename speed zones
 *
 *  filename: name of the file to be read
 *  speed: angular velocity (rad/s) of body
 *  zones: number of zones that are to be read from file
 *
 *  The program outputs two files:
 *   vprofile.dat - radial dist. of visc losses along
 *                      one face of the gear
 *   vprofile_total.dat - radial dist. of visc loss over all faces.
 *
 */

#include <iostream>
 using std::cerr;
 using std::cout;
 using std::endl;
```

```cpp
 using std::ios;

#include <fstream>
 using std::ifstream; //input file stream
 using std::ofstream; //output file stream

#include <cstdlib>
 using std::exit;    //exit function prototype

#include <cmath>

int main(int argc, char *argv[]){
//argv[1] = filename and location;
//argv[2] = angular speed;
  if (argc != 4) {
  cerr << " Invalid input options" << endl;
  }

  cout << "PROGRAM START" << endl;

  // Open input, make sure it exists before running
  //ifstream inClientFile("peeled-surfaces.dat", ios::in);
  ifstream inClientFile(argv[1], ios::in);
  if ( !inClientFile){
    cerr << "File could not be opened" <<endl;
    exit(1);
  }
  inClientFile.ignore(80,'\n'); //ignore the first line

  // allocate variables and memory
  //int zones = 11; // if diab ogear
  int zones = atoi(argv[3]); // = 3; // if disk
  cout << "File has " << zones << " zones."<< endl;
```

```cpp
int I,J,points,ncells;
// REFERENCE VALUES
double Dref = .15;
double rho = 1.0;
double Vref = 81.4;
//
double sum_areas = 0.0;
double total_vpower = 0.0;
int stations = 40;
double* vpower_radial = new double[stations];
double* radial_station = new double[stations+1];
double r_min = .04;   //
double rmax;
if (zones == 3){ rmax = 0.15;}//diab disk radius in meters
else {rmax= 0.144;}  //diab gear 1 radius in meters
double delr = (rmax-r_min)/double(stations);
double rad = r_min;


double omega = atof(argv[2]);// radians per second,


for (int i = 0 ; i < stations; i++) {
radial_station[i] = rad;
rad += delr ;
vpower_radial[i] = 0.0; // initialize
}
radial_station[stations] = rmax;



ofstream outClientFile2("vprofile.dat", ios::out);
outClientFile2.precision(7);


for (int zone = 1; zone <= zones; zone++){
```

```cpp
// read header
cout << "Zone = " << zone << endl;

inClientFile.ignore(17,',');   //ignore: zone T = " gear ",
inClientFile.ignore(2,'=');    //ignore: ,I=
inClientFile >> I;
inClientFile.ignore(4,'=');    //ignore: ,J=
inClientFile >> J;
inClientFile.ignore(80,'\n'); //ignore rest of line
cout  << "I = " << I << endl;
cout  << "J = " << J << endl;
points = I*J;

// read data
double* x = new double[points];
double* y = new double[points];
double* z = new double[points];
double* cp= new double[points];
double* u = new double[points];
double* v = new double[points];
double* w = new double[points];
double* cf = new double[points];


for (int i = 0; i < points; i++){
    inClientFile >> x[i];
    inClientFile >> y[i];
    inClientFile >> z[i];
    inClientFile >> cp[i];
    inClientFile >> u[i];
    inClientFile >> v[i];
    inClientFile >> w[i];
    inClientFile >> cf[i];
```

```
 }
 //ignore rest of line and move on to next:
 inClientFile.ignore(80,'\n');

// compute #cells
ncells = (I-1)*(J-1);
cout << "ncells = " << ncells << endl;

//compute cell areas, centroids, centroid radius and theta
int cell_n, point_n;
double* area = new double[ncells];
double* radius = new double[ncells];
double* theta = new double[ncells];
double* xc = new double[ncells]; // x location of area centroid
double* yc = new double[ncells]; // y location of area centroid
double* zc = new double[ncells]; // z location of area centroid
double x1,x2,x3,x4;
double y1,y2,y3,y4;
double z1,z2,z3,z4;
double A1, A2, s1, s2, s3, s4, s5, s6;
double area_zone = 0.0; // start at zero

for (int j = 0; j < J-1; j++){
for (int i = 0; i < I-1; i++){
   cell_n = i + (j)*(I-1) ;
   point_n = i + j*I;
   // multiply by Dref to convert to dimensional units
   // from non-dimensional:
x1=(x[point_n])*Dref;
    y1=(y[point_n])*Dref;
    z1=(z[point_n])*Dref;

    x2=(x[point_n+1])*Dref;
```

```
            y2=(y[point_n+1])*Dref;
            z2=(z[point_n+1])*Dref;


            x3=(x[point_n+I])*Dref;
            y3=(y[point_n+I])*Dref;
            z3=(z[point_n+I])*Dref;


            x4=(x[point_n+I+1])*Dref;
            y4=(y[point_n+I+1])*Dref;
            z4=(z[point_n+I+1])*Dref;


            // area centroid location
            xc[cell_n] = 0.25*(x1+x2+x3+x4);
            yc[cell_n] = 0.25*(y1+y2+y3+y4);
            zc[cell_n] = 0.25*(z1+z2+z3+z4);


             // Area is computed by considering each face as two triangles
             // then taking pythagorian sum of the areas of the respective
             // projections on the three principal planes
        s1 = (x1*y2+x2*y3+x3*y1-x1*y3-x2*y1-x3*y2);
        s2 = (y1*z2+y2*z3+y3*z1-y1*z3-y2*z1-y3*z2);
        s3 = (z1*x2+z2*x3+z3*x1-z1*x3-z2*x1-z3*x2);


        s4 = (x2*y4+x4*y3+x3*y2-x2*y3-x4*y2-x3*y4);
        s5 = (y2*z4+y4*z3+y3*z2-y2*z3-y4*z2-y3*z4);
        s6 = (z2*x4+z4*x3+z3*x2-z2*x3-z4*x2-z3*x4);


        A1 = 0.5*sqrt((s1*s1) + (s2*s2) + (s3*s3));
        A2 = 0.5*sqrt((s4*s4) + (s5*s5) + (s6*s6));


        area[cell_n] = A1+A2;
        radius[cell_n] = sqrt(zc[cell_n]*zc[cell_n]+yc[cell_n]*yc[cell_n]);
        theta[cell_n] = atan2(zc[cell_n],yc[cell_n]);
```

```cpp
area_zone += area[cell_n];
}
}

cout << "Area of zone is = " << area_zone << endl;
sum_areas += area_zone;

// compute v_r, v_th, radius, theta
    double vr1, vr2, vr3,vr4;
    double vth1, vth2, vth3,vth4;
    double* vr = new double[ncells];
    double* vth = new double[ncells];
for (int j = 0; j < J-1; j++){
for (int i = 0; i < I-1; i++){
    cell_n = i + j*(I-1);
     point_n = i + j*I;


    //v_radial
vr1 = v[point_n]*cos( atan2(z[point_n],y[point_n]))
+ w[point_n]*sin(atan2( z[point_n],y[point_n] ));
vr2 = v[point_n+1]*cos( atan2( z[point_n+1],y[point_n+1] ))
+ w[point_n+1]*sin( atan2( z[point_n+1],y[point_n+1] ));
vr3 = v[point_n+I]*cos( atan2( z[point_n+I],y[point_n+I] ))
+ w[point_n+I]*sin( atan2( z[point_n+I],y[point_n+I] ));
vr4 = v[point_n+I+1]*cos( atan2( z[point_n+I+1],y[point_n+I+1] ))
+ w[point_n+I+1]*sin( atan2( z[point_n+I+1],y[point_n+I+1] ));
// multiply by ref. velocity
vr1 = Vref*vr1;
vr2 = Vref*vr2;
vr3 = Vref*vr3;
vr4 = Vref*vr4;


//v_theta
```

```
vth1 = -v[point_n]*sin( atan2( z[point_n],y[point_n] ))
+ w[point_n]*cos(atan2( z[point_n],y[point_n] ));
vth2 = -v[point_n+1]*sin( atan2( z[point_n+1],y[point_n+1] ))
+ w[point_n+1]*cos( atan2( z[point_n+1],y[point_n+1] ));
vth3 = -v[point_n+I]*sin( atan2( z[point_n+I],y[point_n+I] ))
+ w[point_n+I]*cos( atan2( z[point_n+I],y[point_n+I] ));
vth4 = -v[point_n+I+1]*sin( atan2( z[point_n+I+1],y[point_n+I+1]) )
+ w[point_n+I+1]*cos( atan2( z[point_n+I+1],y[point_n+I+1] ));
// multiply by ref. velocity
vth1 = Vref*vth1;
vth2 = Vref*vth2;
vth3 = Vref*vth3;
vth4 = Vref*vth4;


vr[cell_n]=0.25*(vr1+vr2+vr3+vr4);
vth[cell_n]=0.25*(vth1+vth2+vth3+vth4);
}
}


// compute Tau_mag, Vel_mag,  Tau_th
double* Tau_w = new double[ncells];
double* Tau_th = new double[ncells];
double* Cf = new double[ncells];
double cf1, cf2,cf3,cf4;
double Vmag;
for (int j = 0; j < J-1; j++){
for (int i = 0; i < I-1; i++){
cell_n = i+ j*(I-1);
point_n = i + j*I;

cf1 = cf[point_n];
cf2 = cf[point_n+1];
cf3 = cf[point_n+I];
```

```
cf4 = cf[point_n+I+1];
Cf[cell_n]=0.25*(cf1+cf2+cf3+cf4);


Vmag = sqrt(vr[cell_n]*vr[cell_n]+vth[cell_n]*vth[cell_n]);
Tau_w[cell_n] = 0.5*Vref*Vref*rho*Cf[cell_n];
Tau_th[cell_n] = vth[cell_n]*Tau_w[cell_n]/Vmag;
}
}


// viscous forces/torques/power at each cell face
double* F_th = new double[ncells];
double* Torque = new double[ncells];
double* Power = new double[ncells];


for (int i = 0; i < ncells; i++){
F_th[i] = Tau_th[i]*area[i];
Torque[i] = F_th[i]*radius[i];
Power[i] = Torque[i]*omega;
}


// sum of all forces/torques/power of each cell face
double vTorque = 0.0;
double vPower = 0.0;
for (int i = 0; i < ncells; i++){
vTorque += Torque[i];
vPower += Power[i];
}


total_vpower +=  vPower;


// Get the total radial distribution of visc. forces
for (int i = 0; i < ncells; i++){
 for (int j = 0 ; j < stations; j++){
```

```cpp
  if ( (radius[i] > radial_station[j])
    &&  ((radius[i] < radial_station[j+1])) ){
      vpower_radial[j] += Power[i];
}
}
}


cout << "Viscous torque from zone "<< zone << " is = "
<< vTorque << endl;
cout << "Viscous power from zone " << zone << " is = "
<< vPower << endl;


// get the radial distribution of forces on 1 side of the gear
double vradial, delr, rlower, rupper;
if (zones == 3 && zone == 1){ // diab disk, original grid config
for (int i = 0; i < I-1; i++){
vradial = 0.0;
for (int j = 0; j < J-1; j++){
cell_n = i+ j*(I-1);
point_n = i + j*I;
vradial += Power[cell_n];
}
y1=(y[point_n])*Dref;
z1=(z[point_n])*Dref;
y2=(y[point_n+1])*Dref;
z2=(z[point_n+1])*Dref;
rlower = sqrt(y1*y1+z1*z1);
rupper = sqrt(y2*y2+z2*z2);
delr= rupper-rlower ;
outClientFile2 <<  radius[cell_n]  << "    "
 << fabs(vradial)/delr << endl;
}
}
```

```cpp
//inviscid wall w/axial hole diab gear grid
else if (zones == 12  && zone == 10){
for (int i = 0; i < I-1; i++){
        vradial = 0.0;
        for (int j = 0; j < J-1; j++){
          cell_n = i+ j*(I-1) ;
          point_n = i + j*I;
          vradial += Power[cell_n];
        }
y1=(y[point_n])*Dref;
z1=(z[point_n])*Dref;
y2=(y[point_n+1])*Dref;
z2=(z[point_n+1])*Dref;
rlower = sqrt(y1*y1+z1*z1);
rupper = sqrt(y2*y2+z2*z2);
delr= rupper-rlower ;
outClientFile2 <<  radius[cell_n]  << "    "
 << fabs(vradial)/delr << endl;
}
}
//inviscid wall w/axial hole diab disk grid
else if (zones == 6  && (zone == 3 || zone == 6)){
for (int i = 0; i < I-1; i++){
vradial = 0.0;
for (int j = 0; j < J-1; j++){
cell_n = i+ j*(I-1) ;
point_n = i + j*I;
vradial += Power[cell_n];
          }
y1=(y[point_n])*Dref;
z1=(z[point_n])*Dref;
y2=(y[point_n+1])*Dref;
z2=(z[point_n+1])*Dref;
```

```
//this case is unique since i index start
// at outer radius, not inner
  rlower = sqrt(y1*y1+z1*z1);
rupper = sqrt(y2*y2+z2*z2);
delr= rlower - rupper; //-rlower ;
outClientFile2 <<  radius[cell_n]  << "    "
 << fabs(vradial)/delr << endl;
}
}
else if (zones == 11  && zone == 5){ //ogear diab grid
for (int i = 0; i < I-1; i++){
vradial = 0.0;
for (int j = 0; j < J-1; j++){
cell_n = i+ j*(I-1) ;
    point_n = i + j*I;
vradial += Power[cell_n];
}
y1=(y[point_n])*Dref;
z1=(z[point_n])*Dref;
y2=(y[point_n+1])*Dref;
z2=(z[point_n+1])*Dref;
rlower = sqrt(y1*y1+z1*z1);
rupper = sqrt(y2*y2+z2*z2);
delr= rupper-rlower ;
outClientFile2 <<  radius[cell_n]  << "    "
 << fabs(vradial)/delr << endl;
}
}
// diab gear w/ baffles
else if (zones == 13 && (zone == 10 || zone == 12)){
//zone number is really 14 in file but we
// are ignoring that face completely when the program gets called
  for (int i = 0; i < I-1; i++){
```

```
vradial = 0.0;
for (int j = 0; j < J-1; j++){
cell_n = i+ j*(I-1);
point_n = i + j*I;
vradial += Power[cell_n];
}
y1=(y[point_n])*Dref;
z1=(z[point_n])*Dref;
y2=(y[point_n+1])*Dref;
z2=(z[point_n+1])*Dref;
rlower = sqrt(y1*y1+z1*z1);
rupper = sqrt(y2*y2+z2*z2);
delr= rupper-rlower ;
outClientFile2 <<  radius[cell_n]  << "    " <<
 fabs(vradial)/delr << endl;
}
}

// De-allocate arrays
delete[] x;
delete[] y;
delete[] z;
delete[] cp;
delete[] u;
delete[] v;
delete[] w;
delete[] cf;
delete[] area;
delete[] radius;
delete[] theta;
delete[] xc;
delete[] yc;
delete[] zc;
```

```
delete[] vr;
delete[] vth;
delete[] Tau_w;;
delete[] Tau_th;
delete[] Cf;
delete[] F_th;
delete[] Torque;
delete[] Power;

} // end zone loop

inClientFile.close();

cout << "Total area of all grid zones = " << sum_areas << endl;
cout << "Total power of all grid zones = " << total_vpower << endl;
cout << "Total power of whole gear = " <<
 72.0*total_vpower << "W" <<endl;

// output vpower radial profile
ofstream outClientFile("vprofile_total.dat", ios::out);
outClientFile.precision(7);
for (int i = 0 ; i < stations ; i++){
outClientFile <<  radial_station[i] << "    "
 << fabs(vpower_radial[i]) << endl;
}
outClientFile.close();
outClientFile2.close();
delete[] vpower_radial;
delete[] radial_station;
cout << "PROGRAM END" << endl;
return 0;
}
```

Bibliography

[1] Bartz, W. J., *Lubrication of Gearing*, Mechanical Engineering Publications Limited, London, English ed., 1993.

[2] Paul M. Dean, J., "Geometry and Theory of Gears," *Gear Manufacture and Performance*, ASM, 1974.

[3] Boston Gear, Quincy, MA, *Gear Theory Manual*.

[4] Dawson, P. H., "Windage loss in larger high-speed gears," *Proc Instn Mech Engrs*, Vol. 198A, No. 1, 1984, pp. 51–59.

[5] Handschuh, R. F. and Kilmain, C. J., "Preliminary Investigation of the Thermal Behavior of High-Speed Helical Gear Trains," *International Conference on Gears*, International Federation for the Theory of Machines and Mechanisms, Munich, Germany, March 2002, NASA/TM-2002-211336 ARL-TR-2661.

[6] Diab, Y., Ville, F., Velex, P., and Changent, C., "Windage Losses in High Speed Gears - Preliminary Experimental and Theoretical Results," *Journal of Mechanical Design*, Vol. 126, Sept. 2004, pp. 903–908.

[7] Handschuh, R. F. and Hurrel, M. J., "Initial Experiments of High-Speed Drive System Windage Losses," *International Conference on Gears*, Munich,Germany, October 2010.

[8] Handschuh, R. F. and Kilmain, C. F., "Experimental Study of the Influence of Speed and Load on Thermal Behavior of High-Speed Helical Gear Trains," Techinal Memorandm 2005-213632, NASA, 2005.

[9] Coe, H. H., "Comparison of Predicted and Measured Temperatures of UH-60A Helicopter Transmission," Tech. rep., NASA, 1989, Enter text here.

[10] Winfree, D. D., "Reducing Gear Windage Losses from High Speed Gears," *AME Power Transmission and Gearing Conference*, ASME, Baltimore, MD, Sept. 2000.

[11] Colbourne, J., *The Geometry of Involute Gears*, Springer-Verlang, New York, 1987.

[12] von Karman, T., "Über laminare and turbulente Reibung," *Math. Mech.*, Vol. 1, 1921, pp. 244–249.

[13] Schlichting, H., *Boundary Layer Theory*, McGraw-Hill, New York, 6th ed., 1968.

[14] Daily, J. W. and Nece, R. E., "Chamber Dimension Effects on Induced Flow and Frictional Resistance of Enclosed Rotating Disks," *Journal of Basic Engineering*, March 1960, 59-Hyd-9.

[15] Maroti, L. A., Deak, G., and Kreith, F., "Flow Phenomena of Partially Enclosed Rotating Disks," *Journal of Basic Engineering*, September 1960, 59-A-49.

[16] Bayley, F. J. and Owen, J. M., "The Fluid Dynamics of a Shrouded Disk System with a radial Outflow of Coolant," *Journal of Engineering for Power*, July 1970, pp. 335–341, 70-GT-6.

[17] Daniels, W., Johnson, B., and Graber, D., "Aerodynamics and Torque Characteristics of Enclosed Co/Counter Rotating Disks," *Gas Turbine and Aeroengine Congress and Exposition*, Toronto, Canada, June 1989.

[18] Townsend, D., *Dudley's Gear Handbook: The design, manufacture, and application of gears*, McGraw-Hill, New York, 2nd ed., 1992.

[19] Anderson, N. E. and Loewenthal, S. H., "Spur-Gear-System Efficiency at Part and Full Load," Tech. rep., NASA, 10 Dec. 1979, TP 1622 AVRADCOM TR 79-46.

[20] Anderson, N. E. and Loewenthal, S. H., "Effect of Geometry and Operating Conditions of Spur Gear System Power Loss," *Journal of Mechanical Design*, Vol. 103, Jan. 1981, pp. 151–159.

[21] Heingartner, P. and Mba, D., "Determing Power Losses in the Helical Gear Mesh," *Gear Technology*, Sept. 2005.

[22] Handschuh, R. F. and Kilmain, C. F., "Operational Influence on Thermal Behavior of High-Speed Helical Gear Trains," Techinal Memorandm 2006-214344, NASA, 2006.

[23] Houjoh, H., Onshima, S., Matsumura, S., Yumia, Y., and Itoh, K., "Pressure Measurement of Ambient Air in the Root Space of Helical Gears for the Purpose of Understanding Fluid Flow to Improve Lubrication Efficiency," *Design Engineering Technical Conferences and Computers and Information in Engineering Conference*, ASME, Chicago, IL, Sept. 2003, pp. 957–964.

[24] Diab, Y., Ville, F., Houjoh, H., Sainsot, P., and Velex, P., "Experimental and numerical investigations on the air-pumping phenomenon in high-speed spur and helical gears," *Journal Mechanical Engineering Science*, Vol. 219, 2005, pp. 785–800, Proc. IMechE Part C:.

[25] Diab, Y., Ville, F., and Velex, P., "Investigations on power losses in high-speed gears," *Journal of Engineering Tribology*, Vol. 220, 2006, Proc. IMechE Part J.

[26] Johnson, G., Chandra, B., Foord, C., and Simmons, K., "Windage Power Losses From Spiral Bevel Gears With Varying Oil Flows and Shroud Configurations," *Journal of Turbomachinery*, Vol. 131, October 2009.

[27] Seetharaman, S. and Kahraman, A., "A Windage Power Loss Model for Spur Gear Pairs," *Tribilogy Transactions*, Vol. 53, 2010, pp. 473–484.

[28] Petry-Johnson, T., Kahraman, A., Anderson, N. E., and Chase, D. R., "An Experimental Investigation of Spur Gear Efficiency," *Journal of Mechanical Design*, Vol. 130, June 2008.

[29] Farrall, M., Simmons, K., Hibberd, S., and Young, C., "Computational Investigation of the Airflow Through a Shrouded Bevel Gear," *ASME Turbo Expo 2005*, June 2005.

[30] Al-Shibl, K., Simmons, K., and Eastwick, C. N., "Modelling windage power loss from an enclosed spur gear," *Journal of Power and Energy*, Vol. 221, 2007, pp. 331–341, Proc. IMechE Part A.

[31] Eastwick, C. N. and Johnson, G., "Gear Windage: A Review," *Journal of Mechanical Energy*, Vol. 130, March 2008.

[32] Lord, A. A., *An Experimental Investigation of Geometric and Oil Flow Effects on Gear Windage and Meshing Losses*, Ph.D. thesis, University of Wales, Swansea, 1998.

[33] Hill, M. J., Kunz, R. F., Noack, R. W., Long, L. N., Morris, P. J., and Handschuh, R. F., "Application and Validation of Unstructured Overset CFD Technology for Rotorcraft Gearbox Windage Aerodynamics Simulation," *64th Annual Forum of the American Helicopter Society*, April 2008.

[34] Marchesse, Y., Changenet, C., Ville, F., and Velex, P., "Investigations on CFD Simulation fro Predicting Windage Power Losses in Spur Gears," *3rd International Conference on Integrity, Reliability and Failure*, Porto, Portugal, July 2009.

[35] Imai, H., Goi, T., Arisawa, H., and Nishmimura, M., "Reduction in Gear Windage and Churning Loss by Optimum Shroud Desing with aid of CFD," *JSME International Conference on Motion and Power Transmission*, JSME, Matsushima Isles Resort, Japan, May 2009.

[36] Bowen, C., Braddock, C., and Walker, R., "Installation of a High-Reduction-Ratio Transmission in the UH-1 Helicopter," Tech. rep., U.S. Army Aviation Material Laboratories, 1969, USAAVLABS-TR-68-57.

[37] Brennen, C. E., *Fundamentals of Multiphase Flow*, Cambridge University Press, 2005.

[38] Dawson, P. H., "High Speed Gear Windage," *GEC Review*, Vol. 4(3), 1988, pp. 164–167.

[39] Kunz, R. F., Yu, W.-S., Antal, S. P., and Ettorre, S. M., "An Unstructured Two-Fluid Model Based on the Coupled Phasic Exchange Algorithm," *15th AIAA Computational Fluid Dynamics Conference*, Norfolk, VA, June 2001, AIAA 2001-2672.

[40] Clift, S. S. and Forsyth, P. A., "Linear and Non-Linear Methods for the Incompressible Navier-Stokes Equations," *International Journal for Numerical Methods in Fluids*, Vol. 18, 1994, pp. 229–256.

[41] Doormal, J. P. V. and Raithby, G. D., "Enhancements of the SIMPLE Method for Predicting Incompressible Flows," *Numerical Heat Transfer*, Vol. 7, 1984, pp. 147–163.

[42] Rhie, C. M. and Chow, W. L., "Numerical Study of the Turbulent Flow Past an Airfoil with Trailing Edge Separation," *AIAA Journal*, Vol. 21, 1983, pp. 1527.

[43] Thomas, P. D. and Lombard, C. K., "Geometric Conservation Law and its Application to Flow Computations on Moving Grids," *AIAA Journal*, Vol. 17, 1979, pp. 1030–1037.

[44] *PETSC*, http://acts.nersc.gov/petsc.

[45] *METIS*, http://glaros.dtc.umn.edu/gkhome/views/metis.

[46] Menter, F. R., "Two-Equation Eddy-Viscosity Turbulence Models for Engineering Applications," *AIAA Journal*, Vol. 32, 1994, pp. 269–289.

[47] Ferzinger, J. and Perić, M., *Computational Methods for Fluid Dynamics*, Springer, 3rd ed., 2002.

[48] Kunz, R. F., *NPHASE-PSU V3.1 Theory and User's Manual*, 1st ed., 2007.

[49] Chorin, A. J., "A Numerical Method for Solving Incompressible Viscous Flow Problems," *Journal of Computational Physics*, Vol. 2, No. 12, 1967.

[50] Roe, P. L., "Approximate Riemann solvers, parameter vectors and difference schemes," *Journal of Computational Physics*, Vol. 43, 1981, pp. 357–372.

[51] van Leer, B., "Towards the ultimate conservative differences scheme, A second order sequel to Godunov's methods," *Journal of Computational Physics*, Vol. 32, 1979, pp. 101–136.

[52] Coakley, T. J., "Turbulence Modeling Methods for the Compressible Navier-Stokes Equations," 1983, AIAA 83-1693.

[53] Versteeg, H. K. and Malalasekera, W., *An Introduction to Computational Fluid Dynamics: The Finite Volume Method*, Pearson Prentice Hall, 2nd ed., 2007.

[54] Benek, J. A., Steger, J., and Dougherty, F., "A Flexible Grid Embedding Technique with Applications to the Euler Equations," 1983, AIAA 83-1944.

[55] Noack, R. W., "DiRTlib: A Library to Add an Overst Capability to Your Flow Solver," *17th AIAA Computational Fluid Dynamics Conference*, AIAA, Toronto, Ontario, Canada, June 2006, AIAA 2005-5116.

[56] Noack, R. W., "SUGGAR: a General Capability for Moving Body Overset Grid Assembly," *17th AIAA Computational Fluid Dynamics Conference*, AIAA, Toronto, Ontario, Canada, June 2005, AIAA 2005-5117.

[57] Pointwise, *Gridgen User Manual*, version 15.10 ed., 2007.

Vita

Matthew J. Hill

Matthew John Hill was born in Upper Darby, PA on December 20, 1981. In 1989, he moved to Hong Kong and attended the Hong Kong International School until 1992. In that year, he moved backed to Pennsylvania and attended St. Pius X and then Devon Preparatory School, where he graduated in 2000. After graduation, he moved to New York City to pursue his Bachelor of Engineering in Mechanical Engineering at The Cooper Union for the Advancement of Science and Art. After graduating in 2004, he returned to Pennsylvania once again to continue his studies at The Pennsylvania State University. Working under Dr. Lyle Long, he earned his M.S. in Aerospace Engineering in 2006. It was at Penn State where he entered the world of in computational fluid dynamics and rotorcraft engineering working on coupled fluid-structure simulations of helicopter rotors. Afterwards, he continued on at Penn State as a Ph.D. student in Aerospace Engineering working for Dr. Rob Kunz studying gear windage. Following graduation, Matthew plans to work somewhere...

1. REPORT DATE (DD-MM-YYYY) 01-12-2012	2. REPORT TYPE Final Contractor Report	3. DATES COVERED (From - To)

4. TITLE AND SUBTITLE A Computational Investigation of Gear Windage	5a. CONTRACT NUMBER NNC10CA35C
	5b. GRANT NUMBER
	5c. PROGRAM ELEMENT NUMBER
6. AUTHOR(S) Hill, Matthew, J.; Kunz, Robert, F.	5d. PROJECT NUMBER
	5e. TASK NUMBER
	5f. WORK UNIT NUMBER WBS 877868.02.07.03.01.01.01

7. PERFORMING ORGANIZATION NAME(S) AND ADDRESS(ES) National Aeronautics and Space Administration John H. Glenn Research Center at Lewis Field Cleveland, Ohio 44135-3191	8. PERFORMING ORGANIZATION REPORT NUMBER E-18542

9. SPONSORING/MONITORING AGENCY NAME(S) AND ADDRESS(ES) National Aeronautics and Space Administration Washington, DC 20546-0001	10. SPONSORING/MONITOR'S ACRONYM(S) NASA
	11. SPONSORING/MONITORING REPORT NUMBER NASA/CR-2012-217807

12. DISTRIBUTION/AVAILABILITY STATEMENT
Unclassified-Unlimited
Subject Category: 37
Available electronically at http://www.sti.nasa.gov
This publication is available from the NASA Center for AeroSpace Information, 443-757-5802

14. ABSTRACT
A CFD method has been developed for application to gear windage aerodynamics. The goals of this research are to develop and validate numerical and modeling approaches for these systems, to develop physical understanding of the aerodynamics of gear windage loss, including the physics of loss mitigation strategies, and to propose and evaluate new approaches for minimizing loss. Absolute and relative frame CFD simulation, overset gridding, multiphase flow analysis, and sub-layer resolved turbulence modeling were brought to bear in achieving these goals. Several spur gear geometries were studied for which experimental data are available. Various shrouding configurations and free-spinning (no shroud) cases were studied. Comparisons are made with experimental data from the open literature, and data recently obtained in the NASA Glenn Research Center Gear Windage Test Facility. The results show good agreement with experiment. Interrogation of the validative and exploratory CFD results have led, for the first time, to a detailed understanding of the physical mechanisms of gear windage loss, and have led to newly proposed mitigation strategies whose effectiveness is computationally explored.

15. SUBJECT TERMS
Gears; Drive systems; Gear windage; Transmission; Computational fluid dynamics

16. SECURITY CLASSIFICATION OF:			17. LIMITATION OF ABSTRACT	18. NUMBER OF PAGES	19a. NAME OF RESPONSIBLE PERSON STI Help Desk (email:help@sti.nasa.gov)
a. REPORT U	b. ABSTRACT U	c. THIS PAGE U	UU	166	19b. TELEPHONE NUMBER (include area code) 443-757-5802